# BIOFILM-INDUCED CALCIUM CARBONATE PRECIPITATION:

# APPLICATION IN THE SUBSURFACE

by

Adrienne Janell Phillips

A dissertation submitted in partial fulfillment
of the requirements for the degree

of

Doctor of Philosophy

in

Engineering

MONTANA STATE UNIVERSITY
Bozeman, Montana

November 2013

# APPROVAL

of a dissertation submitted by

Adrienne Janell Phillips

This dissertation has been read by each member of the dissertation committee and has been found to be satisfactory regarding content, English usage, format, citation, bibliographic style, and consistency and is ready for submission to The Graduate School.

Dr. Robin Gerlach

Approved for the Department of Chemical and Biological Engineering

Dr. Jeffrey Heys

Approved for The Graduate School

Dr. Ronald W. Larsen

# STATEMENT OF PERMISSION TO USE

Adrienne Janell Phillips

November 2013

# DEDICATION

This dissertation is dedicated to Dr. Warren Jones, a mentor and friend who left behind many students and researchers, including me, inspired by his enthusiasm for the field of Environmental Engineering.

# ACKNOWLEDGEMENTS

This work was supported by the United States Department of Energy's DOE-NETL grant No. DE-FE0004478 and DE-FE0000397. Any opinions, findings, conclusions, or recommendations expressed herein are those of the author and do not necessarily reflect the DOE's views. Partial financial support was also provided by Southern Company and technical advice was provided by Shell International Exploration and Production B.V. I acknowledge DURIP, contract No. W911NF0510255 funding for the Environmental and Biofilm Mass Spectrometry Facility at MSU. Imaging facilities were provided by the Center for Biofilm Engineering and the Image and Chemical Analysis Laboratory at Montana State University.

I wish to acknowledge collaborators Dr. Anozie Ebigbo, Dr. Richard Esposito, Dr. Peter Walsh, Randy Hiebert, Joachim Eldring, Jim Kirksey, Dr. Andrew Mitchell, Dr. Ellen Lauchnor and Dr. Lee Spangler. Thanks also to engineering researchers Jordan Kennedy, Joshua Stringam, Dayla Morris, Neerja Zambare and Adam Rothman. Alaskan Copper (Seattle WA), fabricator and tester, are acknowledged for their contributions to the high pressure vessel. Peg Dirckx prepared graphics and James Connolly provided valuable feedback for the review manuscript. This research effort is truly collaborative and has been great fun.

I thank my committee members for their generous guidance and support, Dr. Robin Gerlach, Dr. Al Cunningham, Dr. Warren Jones, Dr. Abigail Richards, Dr. Frank Kerins and Dr. Jerry Stephens. Finally, I thank my family and friends.

## TABLE OF CONTENTS

TABLE OF CONTENTS-CONTINUED

TABLE OF CONTENTS-CONTINUED

TABLE OF CONTENTS-CONTINUED

TABLE OF CONTENTS-CONTINUED

# LIST OF TABLES

Table Page

# LIST OF FIGURES

Figure Page

LIST OF FIGURES – CONTINUED

# LIST OF FIGURES – CONTINUED

Figure Page

LIST OF FIGURES – CONTINUED

Figure Page

LIST OF FIGURES – CONTINUED

# ABSTRACT

Subsurface leakage mitigation strategies using ureolytic biofilm- or microbially-induced calcium carbonate precipitation (MICP) have been investigated for sealing high permeability or fractured regions. In the subsurface, this technology may help reduce unwanted preferential flow pathways thereby improving the storage security of geologically-stored carbon dioxide or sealing fractures caused by hydraulic fracturing. MICP has been researched for other applications, such as consolidating porous materials, improving construction materials and remediating environmental concerns.

Injection strategies to control saturation conditions and region-specific precipitation were developed in sand-filled columns. *Sporosarcina pasteurii* biofilms were established and calcium and urea solutions were injected to promote mineralization. These injection strategies resulted in (1) promoting homogeneous distribution of $CaCO_3$ along the flow path, (2) minimizing near-injection point plugging, and (3) promoting efficient precipitation by reviving ureolytic activity. Additionally, a Darcy-scale model was calibrated and used to predict experimental results.

The developed injection strategies were used to repeatedly seal a hydraulically fractured, 74 cm diameter Boyles Sandstone core under ambient pressures. To study meso-scale samples under relevant subsurface pressure conditions, a high pressure test vessel, rated to pressures of 96 bar, was developed. The hydraulically fractured sandstone core was loaded into the vessel and treated with MICP at 44 bar of confining pressure. After treatment, the permeability was reduced and the sandstone core withstood three times higher well bore pressures before re-fracturing compared to before MICP treatment.

Additionally, MICP was promoted in three 2.5 cm diameter Berea Sandstone cores under 76 bar of pressure. The cores' permeabilities were reduced and their minimum capillary displacement pressures (MCDP) were increased. Exposure of the biomineralized cores to 24 hours of supercritical $CO_2$ did not negatively impact the permeability or MCDP achieved after mineralization.

These studies suggest MICP may potentially seal and strengthen subsurface high permeability regions or fractures with the advantage that MICP technologies use low-viscosity fluids to penetrate small aperture pores that may not be reachable by traditional cement-based sealing technologies. These studies also point to the need for further research and development activities, particularly under subsurface relevant pressure conditions.

# CHAPTER ONE: INTRODUCTION

## Background

The research presented in this dissertation describes the potential of ureolytic biofilm- or microbially-induced calcium carbonate precipitation (MICP) as a technology toward mitigating subsurface leakage potential in the near-well bore environment [1-7]. This research has been sponsored by two U.S. Department of Energy (DOE) programs: DE-FE0004478, “Advanced $CO_2$ Leakage Mitigation using Engineered Biomineralization Sealing Technologies” and DE-FE0000397, “Investigating the Fundamental Scientific Issues Affecting the Long-term Geologic Storage of Carbon Dioxide”. One challenge for geologic carbon dioxide sequestration is developing ways to control unwanted upward migration of $CO_2$ which may occur through the confining layers (i.e. cap rock) or near well bores in the receiving reservoir [1]. This dissertation investigates the use of microbially-based technologies that can create biofilm and biomineralization deposits to plug preferential flow paths in $CO_2$ injection well fields. Such injection sites may contain a significant number of abandoned wells in addition to the wells actually used to inject $CO_2$.

Our research suggests that the MICP materials can all be delivered via solutions with aqueous viscosity providing the potential to plug small aperture leaks or the rock formation around the wellbore. These aqueous solutions used to promote MICP may provide an alternate approach to cement-based sealing technologies. The research is being conducted at the Center for Biofilm Engineering (CBE) at Montana State

University (MSU) (Montana, USA) in collaboration with MSU's Energy Research Institute (ERI), Southern Company (Alabama, USA), the University of Alabama at Birmingham (UAB) (Alabama, USA), The University of Stuttgart (Stuttgart, Germany), Aberystwyth University (Aberystwyth, United Kingdom), Schlumberger Carbon Services (Illinois, USA), and Shell Exploration and Production B.V. (Rijswijk, Netherlands).

## Dissertation Overview

In this dissertation, MICP is explored under both ambient and subsurface relevant conditions and at bench and meso-scale to reduce permeability and reduce flow through fractures. The dissertation begins with a literature review of MICP applications in Chapter 2. Chapter 3 describes the development of injection strategies to promote MICP and the development of a mathematical model designed to predict the results of calcium carbonate distribution in experimental sand-filled column studies. Chapter 4 demonstrates the use of the injection strategies developed in Chapter 3 to reduce the permeability of a fracture in a 74 cm diameter sandstone core under radial flow and ambient pressure conditions. Chapter 5 discusses the development of a high pressure vessel to house the sandstone core and an experiment to assess MICP facilitated fracture sealing under relevant subsurface conditions. Chapter 6 focuses on ongoing work regarding promoting MICP under high pressure conditions in 2.5 cm diameter, 5 cm long sandstone cores under axial flow conditions. Finally, Chapter 7 draws conclusions about the work and discusses future work required to continue advancing MICP technologies toward deep subsurface applications.

Chapter 2 is comprised of a review paper, “Engineered application of ureolytic biomineralization: a review” which has been published in the journal *Biofouling* [8]. Chapter 2 first presents an introduction to MICP and the fundamental mechanisms surrounding the process. MICP utilizes the urease enzyme (contributed by the microbes or biofilm) to hydrolyze urea in aqueous environments to increase the saturation conditions and promote precipitation of calcium carbonate. The MICP literature focuses on understanding how 1) the ureolytic activity of microorganisms, 2) the manipulation of reaction and transport rates of reagents, and 3) the saturation conditions, may all influence the precipitation of calcium carbonate. MICP has been researched extensively for a wide variety of engineering applications including improving construction materials such as cement [9-11], consolidating or cementing porous media [12-18], controlling hydraulics [2, 4-7, 19], and remediating environmental concerns [20-26].

Chapter 3 describes 61 cm sand-filled column experimental work to support the development of an MICP injection strategy to (1) promote homogeneous distribution of calcium carbonate along the flow path, (2) minimize near-injection-point plugging, and (3) promote efficient calcium precipitation by reviving ureolytic activity. The experimental work performed at MSU was used to calibrate a Darcy-scale model developed with collaborators at the University of Stuttgart. The model was calibrated with the two initial column experiments and was then used to predict the results of future experiments. The model reasonably predicted the results of the calcium distribution along the flow path of two more column experiments. Chapter 3 was published as

"Darcy-scale modeling of microbially induced carbonate mineral precipitation in sand columns" in the journal *Water Resources Research* [27].

Chapter 4 discusses the results of using the injection strategies developed in Chapter 3 to seal hydraulic fractures in a meso-scale Boyles sandstone core. Collaborators from Southern Company procured a 74 cm diameter core from Alabama, shipped it to Montana, where during characterization of the permeability, the core hydraulically fractured along a bedding plane. The MICP procedure was used to hydraulically seal the fracture. This work was published as "Potential $CO_2$ leakage reduction through biofilm-induced calcium carbonate precipitation" in the journal *Environmental Science and Technology* [6].

Chapter 5 details the development of a custom high pressure test vessel used to house meso-scale samples under pressures of up to 96 bar (1400 psi). The vessel was used to study the MICP treatment of the fractured Boyles sandstone core described in Chapter 4 under 44 bar (650 psi) of confining pressure. After MICP treatment, permeability was reduced in the Boyles Sandstone core. A description of the features of the vessel and the details of the high pressure MICP experiment are currently being prepared in the form of a manuscript titled "Meso-scale high pressure test vessel for the examination of biogeochemical processes" to be submitted to the *Journal of Petroleum Science and Engineering*.

Chapter 6 describes another high pressure test system which has been designed and constructed for testing one inch diameter samples 0.1 to 6 inches in length under pressures up to 131 bar (1900 psi) under axial flow conditions. Several MICP experiments have been performed in Berea sandstone cores, where MICP treatment has led to a reduction in permeability and an increase in minimum capillary displacement pressure (MCDP). Preliminary data suggest that the length of time the biofilm growth stage is performed may impact the time required to reduce permeability after initiating MICP treatment. Also, since previous work suggested that the calcium carbonate precipitated from MICP shows resistance under short time scales to acidic supercritical $CO_2$/brine solutions [5], two cores have been exposed to supercritical $CO_2$. Data collected by collaborators at the University of Alabama, Birmingham (UAB), suggest a 24 hour exposure to supercritical $CO_2$ does not negatively impact the reduction in permeability or the increase in MCDP. Additional replicates of the $CO_2$ exposure are required to draw significant conclusions about the impact of supercritical $CO_2$ on biominerals formed in Berea sandstone cores via MICP. This research is ongoing and will result in a collaborative publication with Dr. Peter Walsh at UAB.

Abstracts of papers published previously, which contributed to the advancement of the MICP technology, including the study of the biofilm-induced permeability reduction in sandstone cores [28] and the study of the resistance of biofilm to supercritical $CO_2$ [29] are included as Appendix A and B, respectively. Next, two other abstracts from publications which highlight the research performed at MSU with a focus on subsurface leakage mitigation using microbially- induced calcium carbonate barriers are included as Appendix C and D [2, 3]. Finally, an abstract of a background paper where the resistance of biominerals to supercritical $CO_2$ was tested is included as Appendix E [5]. An analysis of the kinetics of ureolysis under low and elevated pressure conditions are discussed and included in Appendix F. A comparison of high and low pressure ureolysis and precipitation in Berea sandstone cores is described in Appendix G. Finally, details about using X-Ray Computed Tomography (CT) to scan Berea sandstone cores are included in Appendix H.

The experiments discussed in the first 6 chapters of this dissertation suggest that MICP technologies may be applied in the subsurface to reduce permeability of fractures and porous media. The efforts described within, seek to advance the understanding of MICP toward field application by studying the biogeochemical processes under relevant subsurface pressures and closer to field relevant scale. To continue advancing this technology, a few essential questions should be answered. Previous work has demonstrated promising results of reduced permeability and fracture sealing, but long term exposure of the biominerals to supercritical $CO_2$ has not been evaluated sufficiently. This is a crucial research effort to examine the longevity of permeability reduction and impact to the biominerals after long term exposure to supercritical $CO_2$. Also, researching alternate carbon, urea and calcium sources which promote efficient precipitation but enhance the economic feasibility of the technology should be evaluated [4, 30]. Another important point of research is interpreting the pore and micro-scale processes associated with MICP (microbe/mineral interactions) which may help evolve injection strategies to further control distribution of the calcium carbonate. Finally, larger scale models developed as part of an on-going collaboration with the University of Stuttgart will allow the evaluation and design of improved injection strategies. Controlling and manipulating the ureolytic activity, reaction and transport, or saturation conditions surrounding MICP technologies will aid in effectively designing meso-scale lab experiments and field scale deployment strategies.

# CHAPTER TWO

# ENGINEERED APPLICATIONS OF UREOLYTIC BIOMINERALIZATION: A REVIEW

## Contribution of Authors and Co-Authors

Manuscript in Chapter 2

Author: Adrienne J. Phillips

Contributions: Envisioned graphics, table design and major topics of the review. Wrote and revised manuscript.

Co-Author: Robin Gerlach

Contributions: Envisioned graphics and table design and major topics of the review. Contributed to the writing, development and revision of the manuscript with comments and feedback.

Co-Author: Ellen Lauchnor

Contributions: Contributed to the development and revision of the manuscript with comments and feedback.

Co-Author: Andrew C. Mitchell

Contributions: Contributed to the revision of the manuscript with comments and feedback.

Co-Author: Alfred Cunningham

Contributions: Contributed to the graphics, table design and to the development and revision of the manuscript with comments and feedback.

Co-Author: Lee Spangler

Contributions: Contributed to the revision of the manuscript with comments and feedback.

## Manuscript Information Page

Phillips, A.J., Gerlach, R., Lauchnor, E., Mitchell, A.C., Cunningham, A., Spangler, L.
Biofouling: The Journal of Bioadhesion and Biofilm Research
Status of Manuscript:
____ Prepared for submission to a peer-reviewed journal
____ Officially submitted to a peer-review journal
____ Accepted by a peer-reviewed journal
_X__ Published in a peer-reviewed journal

Taylor and Francis
Vol. 29 (6) pgs. 715-733

## Abstract

Microbially-induced calcium carbonate ($CaCO_3$) precipitation (MICP) is a widely explored and promising technology for use in various engineering applications. In this review, $CaCO_3$ precipitation induced via urea hydrolysis (ureolysis) is examined for improving construction materials, cementing porous media, hydraulic control and remediating environmental concerns. The control of MICP is explored through the manipulation of three factors, (1) ureolytic activity (of microorganisms) (2) reaction and transport rates of substrates and (3) saturation conditions of carbonate minerals. Many combinations of these factors have been researched to spatially and temporally control precipitation. This review discusses how optimization of MICP is attempted for different engineering applications in an effort to highlight the key research and development questions necessary to move MICP technologies toward commercial scale applications.

## Introduction

Contrary to the commonly known detrimental effects of biofilms in industrial and medical environments, biofilms may be used for beneficial engineering applications. In particular, ureolytic biofilms or microbes which induce calcium carbonate ($CaCO_3$) precipitation (MICP) have been widely studied for beneficial use in construction materials, porous media cementation, hydraulic control and environmental remediation (Figure 2.1). A primary research focus has been controlling MICP by manipulating parameters that influence saturation state to achieve specific engineering goals. In many cases, engineered applications depend on controlling the rate and distribution of $CaCO_3$

precipitation *in situ*, which is governed by the spatial and temporal variation in saturation state.

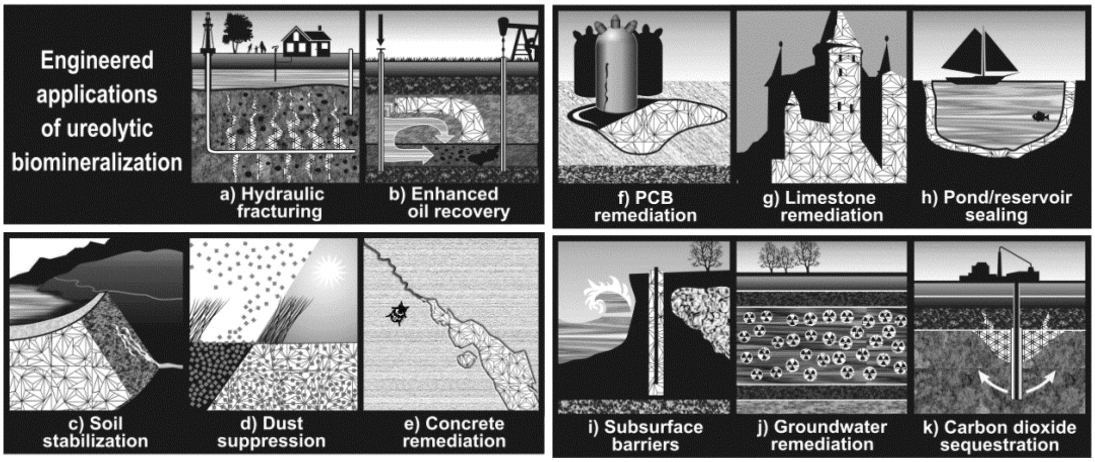

Figure 2.1. Proposed ureolysis-driven MICP engineering applications. White crystal hatch pattern represents $CaCO_3$. (a) sealing subsurface hydraulic fractures (for instance during well closure),(b) manipulating subsurface flow paths to improve oil recovery, (c) strengthening earthen dams or consolidating porous materials, (d) minimizing dust dispersal from surfaces, (e) sealing or remediating concrete fractures, (f) coating PCB-oil contaminated concrete resulting from leaking equipment, (g) treating or coating limestone or concrete to minimize acid erosion, (h) sealing ponds or reservoirs, (i) forming subsurface barriers to control salt water or contaminated groundwater intrusion, (j) remediating subsurface groundwater contaminated with radionuclides or toxic metals (represented by radioactivity symbols), (k) treating fractures (in cap rocks, well bore cements, or casing/cement/formation interfaces) to mitigate leakage from geologically sequestered carbon dioxide injection sites.

Several reviews addressing MICP for use in engineering, particularly, construction applications and porous media cementation have been prepared previously. De Muynck et al. (2010) elegantly reviewed the role of MICP in enhancing and rehabilitating construction materials [9]. Siddique and Chahal also reviewed MICP for use in construction materials, specifically focusing on concrete [11]. Separately, Ivanov and Chu (2008) and DeJong et al. (2010, 2011) comprehensively highlighted the role of the biogeochemical MICP processes in soil and porous media systems [15, 18, 31]. Finally, Al-

Thawdi reviewed MICP for strengthening of sand [32]. This review focuses on how the spatial and temporal control of MICP has been explored to treat construction materials, porous media and remediate environmental problems.

## Microbially-Induced $CaCO_3$ Precipitation

Microorganisms' involvement in mineral precipitation occurs via different mechanisms [33-35]. First, *biologically-controlled* mineralization describes cellular activities which specifically direct the formation of the mineral, for example, the cell mediated process of exoskeleton, bone or teeth formation or the formation of intracellular magnetite crystals by magnetotactic bacteria [35, 36]. Second, *biologically-influenced* mineralization is the process by which passive mineral precipitation is caused through the presence of cell surfaces or organic matter like extracellular polymeric substances (EPS) [35, 36]. Third, *biologically-induced* mineralization is the chemical alteration of an environment by biological activity that generally results in supersaturation and precipitation of minerals [9, 37]. Often combinations of the three different processes are active at the same time in a system. For instance, in the case of *microbially-induced* calcium carbonate precipitation or mineralization (MICP), where the cellular activity influences chemical conditions (saturation state) to promote mineralization, it is possible that *biologically-influenced* mineralization is also occurring since the cells themselves or their exudates may act as nucleation sites for $CaCO_3$ crystal formation [46].

MICP can occur as a byproduct of urea hydrolysis, photosynthesis, sulfate reduction, nitrate reduction or any other metabolic activity that leads to an increase in the saturation state of calcium carbonate [18, 35]. This review focuses on urea hydrolysis (ureolysis) to promote $CaCO_3$ precipitation. In ureolysis-driven MICP, the cellular activity or urease enzyme activity influences chemical conditions (saturation state) to promote mineralization through four factors (1) dissolved inorganic carbon (DIC) concentration, (2) pH, (3) calcium concentration, and (4) potential nucleation sites [38]. The first three factors determine the saturation state, because DIC and pH influence the carbonate ion concentration or activity ($CO_3^{2-}$). The fourth factor impacts the critical saturation state ($S_{crit}$), which is the saturation state at which nucleation (i.e. precipitation) actually occurs under the given conditions. Additionally, the species and concentration of microbe(s), their ureolytic activity, form of microbial growth (i.e. biofilm or planktonic), temperature, salinity, injection strategy (i.e. flow rate, treatment times) and reactant concentration (or activity) may impact the saturation conditions and the efficiency and extent of $CaCO_3$ precipitation[12, 39-41]. Carefully manipulating the (1) ureolytic activity of microorganisms, (2) reaction and transport rates of substrates and (3) the saturation state may greatly influence treatment efficacy.

Ureolytic Activity of Microorganisms. The urease enzyme can be found in a wide variety of microorganisms [42, 43] and contributes to the cell's ability to utilize urea as a nitrogen source [44, 45]. While urease production is quite common across a wide range of soil organisms and found in other natural environments, in the laboratory, many researchers have examined ureolytic MICP using the common soil organism *Sporosarcina pasteurii,* ATCC 11859, formally *Bacillus pasteurii* [46]. *S. pasteurii* is non-pathogenic, does not readily aggregate under most growth conditions and produces large quantities, of active intracellular urease [19, 37, 47]. *S. pasteurii* has been isolated from soil, water, sewage and urinal incrustations [9].

One disadvantage to studying laboratory strains is the microbial complexity of real world environments. In the context of soil stabilization, it was noted that injection of these organisms may result in non-homogeneous distribution of the microbes, or the organisms may face challenges of competition or predation from native organisms [17, 48, 49]. As such, to maintain ureolytic populations in subsurface applications, it may be advantageous to stimulate native attached (biofilm) ureolytic populations rather than augmenting the environment with laboratory strains not adapted to the treatment environment [22, 31, 44, 50]. Also when considering the augmentation of the subsurface with certain organisms, particularly *S. pasteurii,* described as a facultative anaerobe [19, 50] and more recently as an obligate aerobe [51], it is important to consider the electron acceptor's (for example, oxygen in the case of *S. pasteurii*) impact on microbial growth. Although ureolytic activity itself does not depend upon oxygen [40], microbial growth and urease production could be limited by electron acceptor availability. It has been demonstrated that *S. pasteurii* cannot anaerobically synthesize *de novo* urease; therefore the active urease may be limited to the existing enzyme injected with the aerobically grown inoculum [51]. To overcome challenges associated with growth-coupled urease production, stimulation of native populations, injection of electron-acceptor rich growth media or the injection of urease enzyme might be considered.

Additionally, mineral precipitation around cells can influence ureolytic activity by either causing cell inactivation through membrane disruption or by limiting nutrient transport to the cell [37, 39, 52]. Zamarreńo et al. (2009) suggest that precipitation and entombment might be a passive process, which the organisms cannot help but be involved in. Alternatively, they suggest that the precipitation actually protects cells for a short period of time from detrimental calcium concentrations [53]. In an engineering application it is important to consider that entombment may lead to reduced ureolysis and potentially limit overall precipitation. To overcome inactivation and promote additional $CaCO_3$ precipitation, resuscitation or reinjection of organisms as well as additional treatments may be required to maintain an active ureolytic population and maximize precipitation [27, 50].

Reaction and Transport. *Chemical Reactions.* During ureolysis-driven MICP, urease catalyzes the hydrolysis of one mole of urea to form one mole of ammonia and one mole of carbamic acid (Eq. 1), which spontaneously hydrolyses to carbonic acid and another mole of ammonia (Eq. 2). Under circum-neutral conditions the two moles of ammonia become protonated by deprotonating water to form two moles of ammonium ($NH_4^+$) and two moles of hydroxide ions (Eq. 3). The generated hydroxide ions shift the equilibrium of dissolved inorganic carbon species towards bicarbonate ($HCO_3^-$) and carbonate ($CO_3^{2-}$) (Eqs. 4 and 5) [4, 37, 54].

$$CO(NH_2)_2 + H_2O \xrightarrow{\text{Urease}} NH_2COOH + NH_3 \quad (1)$$

$$NH_2COOH + H_2O \xrightarrow{\text{Spontaneous}} NH_3 + H_2CO_3 \quad (2)$$

$$2NH_3 + 2H_2O \longleftrightarrow 2NH_4^+ + 2OH^- \quad (3)$$

$$H_2CO_3 \longleftrightarrow HCO_3^- + H^+ \quad (4)$$

$$HCO_3^- + H^+ + 2OH^- \longleftrightarrow CO_3^{2-} + 2H_2O \quad (5)$$

In the presence of sufficient calcium ion activity, saturation conditions become favorable for $CaCO_3$ precipitation (Eq. 6).

$$Ca^{2+} + CO_3^{2-} \longleftrightarrow CaCO_3\,(s) \tag{6}$$

*Kinetics of Reactions.* Although urease increases ureolysis rates $10^{14}$ times over uncatalysed rates [55], ureolysis is the rate-limiting step in MICP. Concentrations of bacteria, temperature, pH, saturation conditions and salinity have been shown to influence ureolysis kinetics [45, 50, 56]. In general, a higher concentration of cells producing urease has been shown to positively impact the rate of urea hydrolysis, as has elevated (20°C vs. 10°C) temperatures [45, 50, 55].

Several models to predict rates of ureolysis can be considered. In conditions of excess urea, a zero order model might be appropriate, where the rate of ureolysis ($r_{urea}$) is equal to the rate constant and not influenced by the urea concentration [urea] (Eq. 7):

$$r_{urea} = \frac{[urea]}{time} = -k_{urea} \tag{7}$$

Most commonly, first order rate models are presented (Eq. 8) [39, 45, 50, 55], where the ureolysis rate, $r_{urea}$, is dependent on the urea concentration:

$$r_{urea} = -k_{urea}[urea] \tag{8}$$

Ureolysis rates have also been modeled using Michaelis-Menten type expressions that include a term accounting for non-competitive inhibition by ammonium (Eq. 9) [27, 57]. Where $v_{max}$ is the maximum rate of ureolysis, $K_m$ is the half saturation coefficient, [P] is the concentration of ammonium, and $K_P$ is an inhibition constant for ammonium:

$$r_{urea} = \frac{v_{\max}\,[urea]}{(K_m + [urea])\left(1 + \frac{[P]}{K_P}\right)} \tag{9}$$

Rates of ureolysis are dependent on a wide range of factors and have been extensively studied in MICP systems, particularly in laboratory batch systems. Simple batch studies with planktonic cells produce valuable parameters, recognizing that the same parameters may not be fully transferable when considering values associated with biofilm, to use in modeling MICP. Models can help develop understanding of more complex environments not easily studied in the laboratory.

*Transport.* In fluid systems relevant to MICP, both advective and diffusive transport occurs and dominance of one or the other depends on the system. Advection refers to movement of a species with fluid flow. Diffusion refers to the movement of species independent from the bulk fluid movement and driven by concentration or electrostatic potential gradients. Fluid flow conditions (such as whether the flow is laminar or turbulent, axial or radial) and fluid properties (density and viscosity) influence the advective and diffusive properties of the species transport. In MICP application, transport conditions are complex, particularly in the case of radial flow where the fluid velocity changes over the spatial distribution of the flow path.

*Damköhler (Da) Number.* The dimensionless Damköhler (*Da*) number which describes the ratio of reaction rate to transport rate, may serve as an important design tool in MICP application. In biogeochemical processes such as MICP, the reactions (particularly ureolysis) are coupled to the transport of the reactive species. In general terms, *Da* relates the reaction rate of a species to the advective or diffusive mass transport rate of that species (Eq. 10)[58-60] .

$$Da = \frac{Reaction\ Rate}{Transport\ Rate} \tag{10}$$

More specifically, *Da* depends on the kinetics of the reaction and the transport through a specific reactor (or natural) system. For example, in a plug flow system where advective transport dominates, *Da* represents a ratio of the reaction rate to the advective mass transport rate of the species (fluid flow). When $Da < 1$, it does not indicate that reaction is not occurring; it does, however, imply that not all the supplied substrate is reacted and may be transported from the reaction zone. *Da* numbers >1 indicate the reaction is limited by the transport rate for a given length scale.

In a pulsed flow system or within stagnant pore spaces, where diffusive transport is likely to dominate, *Da* is the ratio of reaction rate to the effective diffusion rate of the reactive species. In diffusion dominated cases, a *Da* <1 indicates the reaction rate is limited by reaction kinetics rather than diffusion, however given enough time, the reaction may proceed to completion. Alternatively, a *Da* number >1 indicates the reaction rate drives the establishment of concentration gradients of reactive species.

*Da* incorporates many of the factors related to reaction and transport into a single unit-less number, for ease of comparison and design. The systematic analysis of *Da* may reveal a functional design tool (for example, predicting flow rates or pulsed treatment times) for MICP not previously explored.

<u>Saturation Conditions.</u> $CaCO_3$ precipitation is ultimately governed by the saturation state (S or Ω) of calcium carbonate where $[Ca^{2+}]$ and $[CO_3^{2-}]$ represent the activities of $Ca^{2+}$ and $CO_3^{2-}$ ions, which are approximately equal to concentration for low

ionic strength conditions, and $K_{so}$ is the temperature dependent equilibrium solubility constant (Eq. 11):

$$S\ or\ \Omega = \frac{\{Ca^{2+}\}\{CO_3^{2-}\}}{K_{So}} \tag{11}$$

At S=1, the solution is considered in equilibrium with the solid phase. If S is greater than one (S>1), the solution is considered supersaturated with respect to $CaCO_3$ and $CaCO_3$ precipitation is thermodynamically favored. If S is less than one (S<1) the solution is considered undersaturated and dissolution of solid phase $CaCO_3$, if present, is thermodynamically favorable (Figure 2.2) [61]. The saturation index (SI) is represented as the $\log_{10}$ of the saturation state (Eq. 12). When SI is positive then the solution is supersaturated and vice versa. Further detailed calculations can be found in several publications of potential interest to the reader [45, 50, 56].

$$SI = log_{10}(S) \tag{12}$$

While the S or SI predicts whether precipitation is thermodynamically favored, it does not necessarily predict the saturation state at which precipitation actually begins ($S_{crit}$). $S_{crit}$ or $SI_{crit}$ are empirical values which reflect how highly supersaturated a solution must become before precipitation is actually observed. This critical supersaturation is related to overcoming the nucleation activation free energy barrier (Ferris et al., 2003) and is likely impacted by a variety of system parameters influencing the actual activity of $Ca^{2+}$ and $CO_3^{2-}$ ions. Saturation values in the literature for batch systems have been reported in the range of S=12 to 436 [45, 50, 55, 56, 63]. $S_{crit}$ may depend on many factors including the kinetics of ureolysis, initial cell density, presence of nucleation points and presence of organics.

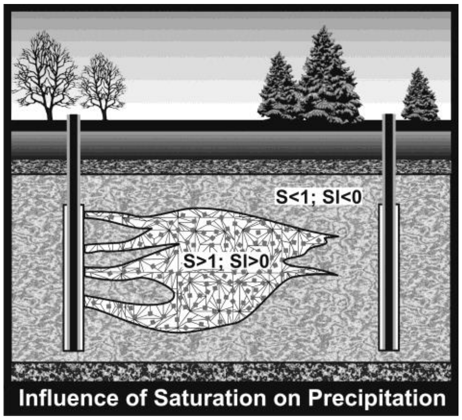

Figure 2.2. Influence of saturation on precipitation in a cross section of a groundwater aquifer (precipitates are represented by white crystal hatch pattern). Saturation states greater than one ($S>1$) and saturation indices greater than zero ($SI>0$) indicate precipitation is thermodynamically favored; saturation states less than one ($S<1$) and saturation indices less than zero ($SI<0$) indicate dissolution is favored if the mineral form is present. The saturation state can vary spatially and temporally due to reaction and transport rates which create concentration gradients [62].

*Nucleation.* As outlined above, it is quite possible that combinations of different biomineralization processes are active at the same time in a system. For instance, while ureolysis can increase the saturation state of the bulk environment (*biologically-induced* mineralization) the precipitation process itself might be initiated by the microbes serving as nucleation sites (*biologically-influenced* mineralization) (Figure 2.3a, b) [9, 37]. Once precipitation has commenced, ureolysis may maintain a high saturation index and cells as well as newly precipitated minerals likely act as additional templates or nucleation sites to facilitate crystal growth [37, 64]. While the influence of cell surfaces as nucleation sites has been widely discussed [65], Mitchell and Ferris (2006) observed an equal critical saturation state in solutions with and without bacterial cells separated by dialysis membranes that allowed for transport of solutes between the two solutions[66]. In addition, $CaCO_3$ nucleation has been noted in a variety of systems to be influenced by the presence of certain proteins, microbial biomolecules, EPS, other available passive substrates, heterogeneous nucleation on bottle walls or be solely occurring homogeneously in solution [33, 56, 63].

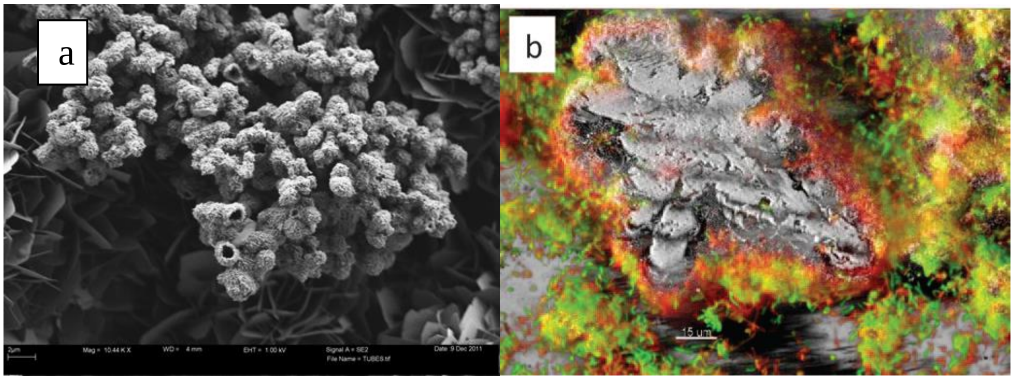

Figure 2.3. Images of cells associated with minerals. (a) Scanning electron microscopy image of tube-like (with similar diameters as bacterial cells) calcium-containing minerals possibly entombing *S. pasteurii* cells. Other researchers have noted similar findings via SEM analysis where rod shaped bacteria-like structures were observed inside and adjacent to $CaCO_3$ crystals or as rod shaped impressions in the $CaCO_3$ crystal [19, 20, 37, 39, 55, 56, 66, 67]). (b) Confocal laser scanning microscopy image of microbes (red and green) closely associated with $CaCO_3$ precipitates (grey) (Reprinted with permission, Cambridge University Press publication Microscopy Today) [7].

*Mineralogy*. Three primary polymorphs of $CaCO_3$ exist: calcite, vaterite, and aragonite. It is well known that surface-attached communities of microorganisms, or biofilms, secrete EPS rich in polysaccharides and other organic macromolecules. EPS and organic matter have been linked to the formation of vaterite which may be stabilized in the presence of certain organics [68, 69]. Vaterite has been found as a minor, meta-stable or transitional phase in the formation of calcite [70]. The maturation of $CaCO_3$ from vaterite to calcite may be described by the Ostwald Step Rule where metastable forms nucleate and then are replaced with more stable forms (a sequential formation in time also known as paragenesis) [71]. Mechanisms of initial nucleation, which may be influenced by the microbial growth conditions, the presence of certain organics, such as

EPS, or the saturation conditions of the fluid, as well as subsequent maturation are not completely understood [53, 68, 71, 72]. Crystal size may be a factor in the efficacy of an MICP technology. $CaCO_3$ crystals precipitated via ureolysis-driven MICP have been observed to be generally larger and less soluble than those precipitated under the same abiotic bulk solution conditions [5, 66].

To summarize, $CaCO_3$ precipitation via the ureolysis-driven MICP is initiated by creating conditions oversaturated with respect to $CaCO_3$, likely combined with the increased abundance of cell surfaces as nucleation points at the point of critical saturation and finally crystal growth on nuclei [45].

## Engineering Applications

### Construction Materials

Biodeposition. Biodeposition refers to the deposition of MICP to protect the surface of porous materials (such as limestone, concrete or bricks) from water intrusion. MICP treatment can decrease a material's ability to absorb water, restore the surface and reduce further potential weathering (Figure 1g) [9, 54]. For example, in reinforced concrete, pores might allow penetration of water and ions, particularly chloride or acids, leading to deleterious corrosive effects to the embedded reinforcing steel [54, 73, 74]. In a MICP treated surface, the $CaCO_3$ can clog pores and decrease water penetration through a protective calcite layer. Since De Muynck et al. (2010) provided a very comprehensive review of this topic, this review will discuss how the experimental conditions, particularly the promotion of ureolytic activity and application of substrates, influences treatment efficacy.

First, ureolytic *Bacillus sphaericus* isolates from calcareous sludge were found to be effective at $CaCO_3$ precipitation on limestone cubes [54]. The cubes were immersed in liquid bacterial cultures to promote biofilms and then immersed in urea and calcium chloride treatments to promote $CaCO_3$ formation. It was concluded, that isolates with a highly negative zeta (ζ)-potential, an indication of electrical surface potential of cells, would more successfully colonize positive ζ-potential limestone. It was also concluded that high initial urea degradation rate and high surface covering with $CaCO_3$ on the attached microbes (biofilm) produces the most homogeneous and coherent $CaCO_3$ coating to provide protection of limestone from water intrusion [54] .

De Muynck et al. (2008), performed similar biodeposition tests on concrete cubes treated with urea and calcium chloride or calcium acetate (an alternate to corrosive chloride) treatment solutions. Their study found no difference between calcium sources when examining *B. sphaericus* ureolysis-induced in terms of samples' weight gain due to precipitation or chloride penetration resistance. Additionally, they concluded the biofilm may act as a template or primer for initial deposition of $CaCO_3$ [67]. Second, De Muynck et al. examined the influence of urea and calcium concentrations on MICP coating of limestone. It was reported that increasing urea and calcium concentrations and repeated treatment improved limestone's resistance to water absorption due to $CaCO_3$ precipitation [75]. Still, it was concluded that the benefits of increased urea and calcium chloride concentration should be balanced with the detrimental impacts such as unwanted ammonium by-product formation or stone discoloration [75]. Finally, De Muynck et al. investigated the pore structure of French limestone base materials to determine the impact on the penetration depth and protective performance of *B. sphaericus* ureolysis-driven MICP deposits. More successful bacterial penetration of larger pores resulted in more deposition in stones with higher porosity [74].

Chunxiang et al. (2009) used *S. pasteurii*-facilitated MICP to coat cement with $CaCO_3$ biodeposits to study corrosion resistance. By altering the order of addition of calcium and urea the researchers increased the MICP deposits' effectiveness against water absorption and acid corrosion of the cement. They concluded that adding calcium before urea to a stationary phase bacterial culture produced a more compact $CaCO_3$ deposit because calcium influenced ureolysis activity and rates which may impact the adhesion and thickness of the $CaCO_3$ layer [76]. Whiffin (2004) suggested that high calcium nitrate ($Ca(NO_3)_2$) concentrations may inhibit urease activity [77], although mixed effects on activity were observed in a microbial consortium and among environmental isolates [42, 44]. Therefore, depending on the organisms' tolerance for calcium concentrations, a balance might need to be struck between high $Ca^{2+}$ concentrations which may inhibit ureolysis and low $Ca^{2+}$ concentration which may not allow for the formation of sufficiently protective deposits.

Biocement. Concrete is one of the most commonly used construction materials, but it is prone to weathering and cracking. Cracks form in concrete due to aging and/or freeze thaw cycles which lead to pathways for corrosive fluid intrusion [10, 78-80]. Healing of fractures in concrete with MICP (Figure 1e) would be advantageous since other sealants may degrade over time or are environmentally toxic, whereas $CaCO_3$ may be a more benign treatment [11]. Here, biocement refers to the use of MICP to produce binder materials to seal fractures or improve strength and durability of cementitious materials (such as adding microbes to cement mixtures). Since this topic has been extensively reviewed by others [9, 11], this section will focus on investigations related to the control of MICP treatment for both concrete fracture sealing and cementitious material improvement.

Bacteria in or applied to concrete may face challenges to their activity including small pore sizes as concrete cures, which may damage or inhibit the penetration of organisms, and the high pH, which may inhibit biological activity. Cement, or rather the water associated with cement, can have a pH of 11-13 even after it is completely cured [79, 81]. Alkaliphilic spores embedded in concrete were observed to retain culturability for less than four months presumably due to cell damage as the cement cured and pore size decreased [88]. Given small pore sizes and high pH conditions, research has focused on the use of alkaliphilic organism and/or methods to protect the organism to maintain viability and ureolytic activity during treatment.

To protect microbial urease activity from high pH in cement, *S. pasteurii* were immobilized in polyurethane (PU) foam in cement fractures and treated with urea/calcium solutions. Researchers found urease activity was maintained and hypothesized enzyme activity might be stabilized for longer periods of time when embedded in a matrix such as PU foam [90]. Instead of immobilizing cells, Bachmeier et al. (2002) investigated the use of urease immobilized in polyurethane foam, since this treatment methodology does not depend upon maintaining cell viability for ureolysis. Even though immobilized enzyme treatments may have shown decreased $CaCO_3$ precipitation rates (possibly due to diffusion limitation of either calcium or carbonate), significantly increased stability with elevated temperature was observed compared to the free enzyme [82]. Most recently, Bang et al. (2010) immobilized varying concentrations of *S. pasteurii* cells on Siran$^{TM}$ glass beads to fill into concrete cracks for crack remediation. Once again immobilization was speculated to have stabilized cell and urease activity from the adverse effects of the concrete's high pH [90].

Van Tittelboom et al. (2010) studied the efficacy of silica gel supplemented with *B. sphaericus* cells injected into concrete fractures and treated with calcium chloride, calcium acetate, or calcium nitrate and urea solutions. The calcium source did not change the reduction in water absorption (all sources worked to produce deposits in fractures) indicating the possibility of using alternative calcium sources. The necessity for some protection of cells from the high pH in concrete was suggested as bacteria injected without gel failed to precipitate $CaCO_3$, although it is also possible that cells injected in the fracture without silica gel may have not attached well and thus resulted in reduced treatment efficacy [83].

Another approach to concrete fracture remediation is self-healing, where healing agents are released or activated when fractures form [80, 84]. In one unique study, carrying agents including polyurethane or silica-gel, *B. sphaericus,* and urea/calcium nitrate treatments were loaded into separate glass capillaries and embedded in mortar, which upon cracking fractured the glass capillaries allowing the carrying agents, cells, and treatment solutions to mix. The bacteria retained ureolytic and $CaCO_3$ precipitating activity after immobilization in both polyurethane and silica, but a more homogeneous distribution of $CaCO_3$ crystals was observed in the silica gel versus polyurethane foam which was attributed to the ability of bacteria to distribute more homogeneously through the less viscous silica sol (before gelation) than polyurethane pre-polymer [93].

Ureolytic MICP can potentially improve cement's strength by incorporating cells into the cement mixture, although high concentrations of cells may reduce the compressive strength due to interference by biomass with the mortar integrity [85]. When certain cell concentrations of *Bacillus sp.* isolated from commercially available cement were mixed into a water, cement, sand mixture and cured in urea/$CaCl_2$ treatment the microbial cement was found to resist water uptake better and show improved compressive strength compared to the control cement [73]. Compressive strength of fly ash or silica fume amended concrete was also found improved by MICP induced by *B. megaterium* [86] and *S. pasteurii* [87].

In summary, construction materials may be improved by MICP. It has been shown, that increasing the number of treatment applications, changing the calcium source to avoid deleterious impacts from chloride, applying treatment to higher porosity materials, promoting biofilm growth before calcium treatment and varying the order in which the constituents are applied (calcium before urea) can yield protective $CaCO_3$ coatings via the MICP process. Also, some promise was found in using ureolytic MICP to improve the strength of concrete and remediate concrete fractures, but immobilization of cells or urease enzyme in gels or polyurethane was required to provide protection from high pH activity inhibition or damage to cells during cement curing. Immobilization in turn may lead to diffusion limitations and potentially reduced precipitation. These studies demonstrate the importance of protecting the urease activity by either promoting cells to attach to the surface or immobilizing them.

## Porous Media Cementation

Ureolysis-driven MICP to alter or improve mechanical properties of unconsolidated porous media has been extensively investigated. This method has been proposed to suppress dust (Figure 1d), reduce permeability in granular media, improve soils, or stabilize slopes (Figure 1c), and strengthen liquefiable soils [13, 17, 88, 89]. $CaCO_3$ crystals precipitated during MICP can bridge gaps between porous media grains to bind them together; precipitation can also reduce the pore throat size, porosity and permeability, and increases the stiffness and strength of the porous media matrix [18]. Much of the work to date has been performed to improve the efficiency of precipitation, maximize the extent of the treatments and balance chemical use to reduce costs for field application. In engineering applications such as sand consolidation or soil strengthening, it is preferable to precipitate $CaCO_3$ homogeneously over distance and use as little reactant volume as possible for economic reasons [12, 14]. While preferential plugging may be effective in some engineering applications, non-homogeneous bacterial distribution and non-homogeneous precipitation may have the disadvantage of near-injection-point plugging where substrates are abundant, limiting the spatial extent of the treatment [40, 90, 91]. Proposed strategies for controlling precipitation include promoting spatial distribution of ureolytic activity (cells), manipulating the transport and reaction rates of the reactive species and promoting favorable saturation conditions in specific regions.

Sand Consolidation. Whiffin et al. (2007) described a sand stabilization treatment method (BioGrout), which followed *S. pasteurii* inoculation with a calcium chloride solution to increase bacterial adhesion to the sand before MICP treatment. This treatment sequence achieved significant strength improvement and porosity reduction in sand packed columns. Although non-uniform precipitation was observed along the length of the column, Whiffin and colleagues reasoned that more homogeneous distribution could be achieved by shifting the balance of supply and conversion (i.e. *Da*) by increasing flow rates or lowering conversion rates to achieve higher reactant infiltration [13].

Following this initial Biogrout work, Harkes et al. (2010) altered ionic strength and flow rates, again influencing reaction kinetics and transport rates related to *Da*, to study the impact on ureolytic bacterial distribution in sand to prevent near-injection-point clogging. Bacterial attachment was found to be positively influenced by increased salinity or ionic strength of the transporting fluids, which could be due to a decrease in electrostatic repulsion forces between cells and porous media surfaces [92, 93]. However, the increase in ionic strength might also promote attachment of cells near the injection point and limit spatial extent of treatment. So, by altering the transport rate (increasing flow) of low ionic strength solutions Harkes et al. observed a more homogeneous distribution of bacteria, but cautioned against the loss of attachment and activity when low ionic strength solutions are used [12]. Transport of bacteria through a porous media matrix is a complex function of the size and surface properties of the cell, electrical interactions, the flow rate and chemistry of the transport fluid as well as the pore size distribution of the porous media [12, 93-96]. A balance between ionic strength and transport could help promote more homogeneous cell and ultimately ureolytic activity distribution.

Much of the work presented is performed on smaller scales in a laboratory-controlled environment, yet in 2010 van Paassen et al. embarked on a scaled-up demonstration of MICP in 100 $m^3$ of sand to determine ground improvement abilities and extent of precipitation. Similar to the injection strategies developed by Whiffin et al. (2007) and Harkes et al. (2010), the sand was inoculated with *S. pasteurii* cells, cementation solution followed to promote bacterial adhesion and then urea and calcium solutions were injected 10 times over 16 days. As much as 40 $m^3$ of the 100 $m^3$ sand reactor were cemented via MICP with a visible wedge shape between the injection and extraction wells (Figure 2.4) [14].

Figure 2.4. Image of cemented sand body from the large scale Biogrout experiment. Reprinted from Journal of Geotechnical and Geoenvironmental Engineering, Leon A. van Paassen, Ranajit Ghose, Thomas J. M. van der Linden, Wouter R. L. van der Star, and Mark C. M. van Loosdrecht, “Quantifying Biomediated Ground Improvement by Ureolysis: Large-Scale Biogrout Experiment”, 1721-1728., (2010), with permission from ASCE.

Liquefiable Soils. Other researchers have also recently examined scaled-up ureolysis-driven MICP. Burbank et al. (2011) studied field-scale ureolysis-driven MICP to strengthen liquefiable soils. Liquefiable soils are loose granular soil deposits generally found in saturated conditions, which may undergo a decrease in shear strength when subject to seismic waves and contribute to man-made structure failure during earthquakes [17]. Soils on the Snake River's shore (USA) were subjected to ureolytic biomineralization treatments, which yielded soils cemented with ~1% by weight $CaCO_3$ in the near surface and 1.8-2.4% calcite below 90 cm [17]. This was less precipitation than observed in laboratory enriched samples, which was attributed to the lower technical quality of the field study's calcium source. Their findings also suggested higher concentrations of $CaCO_3$ formed away from the injection point rather than closer to the injection point. Researchers attributed this to either 1) eluviation where fine-grained materials or $CaCO_3$ particles may have been transported downward with the infiltrating water or 2) increased ureolysis and possibly delayed subsequent precipitation occurring in the deeper soil profile.

Subsurface Barriers. In certain coastal areas, salt water intrusion into freshwater aquifers during groundwater extraction has become a major problem. The problem is often addressed by creating underground dams or increasing artificial recharge of fresh water to prevent migration of salt-laden water into freshwater aquifers. Subsurface MICP barriers may be an alternative to these methods (Figure 1i) [97]. Due to salt water intrusion into ground water, MICP must be able to occur in saline conditions to be applied in these environments. In 2011, Mortensen et al. assessed the influence of various environmental factors on ureolysis-driven MICP to determine suitable *in situ* environment. First, they observed that short term ureolytic activity did not appear to be inhibited by anaerobic conditions after cells were cultured aerobically, which agrees with findings by Parks (2009), Tobler et al. (2011), and Martin et al. (2012) [50-52]. Second, they found full and half-strength seawater enhanced $CaCO_3$ precipitation rates possibly due to increased alkalinity and cation availability [40]. Finally, the authors note that manipulating the reaction rates and transport rates by inhibiting precipitation rates with increased ammonium concentrations or by controlling flow rates is important in achieving homogeneous distribution of MICP. These results demonstrate the potential of ureolysis-driven MICP for developing subsurface barriers to prevent salt water intrusion.

Aquaculture: Impermeable Crusts. One promising engineering application of ureolysis-driven MICP is the preparation of crusts to control seepage from aquaculture ponds or reservoirs into underlying soils or sands (Figure 1h). Stabnikov et al. (2011) used the halotolerant, alkaliphilic *Bacillus sp. VS1* isolate to seal a sand-lined model pond. Successive percolation treatments with high concentrations of urea and calcium solutions resulted in a nearly impermeable crust on the surface of the sand, which markedly reduced the seepage rate, taking sand to the same permeability range as well compacted clay (Figure 2.5) [16].

Dust Suppression. Bang et al. (2011), showed the potential for using ureolysis-driven MICP to suppress dust (Figure 1d). Dust poses problems to human health and is traditionally suppressed through means of chemical application or watering down which may be difficult to maintain or may use environmentally problematic chemicals. Ureolysis-driven MICP is proposed as an alternative to consolidate dust particles. *S.*

*pasteurii* cells or urease and urea/calcium chloride treatment solutions were sprayed over sand samples, which were then subjected to wind erosion tests. Bang et al. (2011) found MICP dust control to be very effective, but its efficiency to be subject to the soil type and grain size distribution as well as environmental conditions such as humidity and temperature.

Figure 2.5. Photo of ~1mm thick crust of calcite on sand surface. Reprinted from Cement and Concrete Research, Viktor Stabnikov, Maryam Naeimi, Volodymyr Ivanov, Jian Chu, “Formation of water-impermeable crust on sand surface using biocement”, 1143-1149., (2011), with permission from Elsevier.

In summary, ureolysis-driven MICP has been explored for several engineered applications involving porous media, including consolidating sand or soils, creating subsurface barriers, sealing aquaculture ponds and suppressing dusts. These applications are often controlled by manipulating the transport and reaction rates to either promote homogeneous deposition or controlled deposition in selective areas. In porous media MICP application, a complex set of factors, including environmental conditions may greatly influence the treatment results.

## Hydraulic Control and Environmental Remediation

Radionuclide and Metal Remediation. *Radionuclide Remediation.* The US Department of Energy (DOE) faces environmental remediation challenges such as the long-term management of the Hanford site in Washington, USA, where groundwater is contaminated with radionuclides [20-22, 98, 99]. Traditional treatment methods like pump and treat have been found ineffective at the site to remediate or prevent migration of mobile radionuclide groundwater contaminants [21]. Therefore, years of research have evolved methods to stimulate ureolytic subsurface organisms to promote $CaCO_3$ precipitation which in turn promotes co-precipitation and solid phase capture of some of these contaminants, in particular strontium-90, a uranium fission by-product (Figure 1j). In subsurface environments saturated with respect to $CaCO_3$ minerals, the co-precipitation forms a long-term immobilization mechanism while the $^{90}Sr$ decays [22, 63, 98].

Control of strontium co-precipitation in the subsurface has been widely researched by studying the rates of ureolysis and precipitation. Warren et al. (2001) demonstrated that 95% of the total strontium added to batch ureolysis-driven (*S. pasteurii)* MICP samples could be incorporated in $CaCO_3$ precipitates. Further studies demonstrated that *S. pasteurii* in artificial groundwater media exhibited higher rates of ureolysis at slightly elevated temperatures, strontium co-precipitation increased with increasing $CaCO_3$ precipitation rates, and higher ureolysis rates could reduce the time to reach critical saturation ($S_{crit}$) which is important since $CaCO_3$ precipitation rates were observed greatest near $S_{crit}$ [20, 45, 55].

Since augmentation of subsurface environments may not be ideal or feasible, Fujita et al. (2008) investigated the potential to enrich native ureolytic organisms *in situ* in the Eastern Snake River Plain Aquifer (Idaho, USA) for the purpose of remediating groundwater by co-precipitating strontium. The authors suggest that multiple treatments with low concentrations of a carbon source (molasses) to stimulate the subsurface community followed by the injection of urea can promote ureolytic subsurface populations [21]. Another microbial enrichment test was performed with groundwater and sediment samples from wells at the Hanford site in Washington, USA [22]. Urea stimulated sediment samples showed 2-4 orders of magnitude higher specific ureolytic activity compared to groundwater samples, leading researchers to hypothesize that greater activity was associated with attached (or biofilm) communities compared to planktonic cells [22].

*Metal Remediation.* Toxic metal (e.g. copper, arsenic, chromium, etc.) contamination in soil or groundwater has been attributed to mining and smelting as well as other industrial activities. Toxic metal contamination is linked to human health problems and current remediation efforts can be costly and relatively ineffective. Traditional remediation efforts include phytoremediation, removing or covering the soils with clean soil, on-site chemical leaching of contaminants or bioremediation with toxic metal-tolerant bacterial species [24]. However, these treatment methods may not be long-term solutions. For example, in bioremediation many bacterial species can decrease the solubility and thus immobilize metals by changing their redox state, however future changes in oxidation-reduction potential could lead to remobilization; therefore, an alternate remediation method is $CaCO_3$-based co-precipitation.

It was previously shown that chromate was found associated with $CaCO_3$ in co-precipitated form [100] and then Achal et al. in 2012 isolated *Sporosarcina ginsengisoli* CR5, an arsenic-tolerant, urease-positive bacterium and researched the organisms MICP potential to remediate arsenic contaminated soils. Although organism growth was slowed in the presence of arsenic, significant arsenic was removed from aqueous solution during ureolytic MICP [24]. Another study focused on remediation of copper via the MICP process by the copper-tolerant, ureolytic organism *Kocuria flava* CR1. Copper bioremediation studies were performed with *K. flava* in urea and calcium containing batch with copper concentrations up to 1000 mg/L [23]. The authors reported a positive correlation between higher urease production and higher copper removal from aqueous solutions [23].

In elevated concentrations, metals may be toxic to organisms involved in remediation. As such, Kurmaç (2009) evaluated the impact of varying concentrations of lead, cadmium, chromium, zinc, copper and nickel to ureolysis-driven MICP treatment technology in synthetic wastewater amended with urea and calcium chloride. Authors found the impact of metal toxicity on microbial substrate degradation increased in the following order: Cd (II) > Cu(II) > Pb(II) > Cr(VI) > Ni(II) > Zn(II) [101]. In the application of MICP, metal toxicity may be a limiting factor in treatment efficacy, but isolation of metal-tolerant ureolytic organisms from contaminated environments may improve the treatment potential.

PCB Containment. Additional recalcitrant contaminants threatening environmental and human health are PCBs (polychlorinated biphenyls), which can contaminate concrete surfaces when PCB-containing oil leaks from equipment. Methods of removing PCB-contaminated oil include solvent washing, hydroblasting or sandblasting followed by encapsulation in epoxy coating. Epoxy coating may be ineffective due to resurfacing of the oil over time [102]. An alternative to epoxy coating is the use of ureolysis-driven MICP to produce a coating to seal PCB contaminated concrete (Figure 1f). By applying *S. pasteurii* cultures and urea/calcium treatment to the surface of PCB-coated cement cylinders, surficial PCB-containing oils were encapsulated. No leaching through the MICP coating was observed and permeability was reduced by 1-5 orders of magnitude [102].

Carbon Dioxide ($CO_2$) Sequestration. With atmospheric $CO_2$ concentrations on the rise, mitigation strategies are widely being explored. One proposed mechanism for reducing emissions is the capture and storage of $CO_2$ in deep geologic reservoirs, such as deep saline aquifers. The efficacy of this mitigation method depends on preventing potential $CO_2$ leakage either back to the surface or into overlying aquifers. Possible reasons for leakage include (1) the corrosive effect of supercritical $CO_2$ to well cement (carbonation), (2) leakages through microfractures in those well cements or (3) areas of increased cap rock permeability or decreased well bore integrity [103-106]. Traditional well repair methods include the use of cements (such as fine cement); however, these may be of higher viscosity than aqueous solutions used to promote MICP. Higher viscosity fluids may not adequately penetrate small pore spaces and potentially not seal microfractures where low viscosity supercritical $CO_2$ could find leakage pathways. As such, MICP may be an effective tool to seal fractures or high permeability leakage zones (formation trapping) in the context of $CO_2$ sequestration (Figure 1k), and may also be effective in helping to reliably abandon wells after fossil fuel extraction (Figure 1a).

Three proposed methods of *in situ* $CO_2$ leakage mitigation to which ureolysis-driven MICP can contribute are formation trapping, solubility trapping and mineral trapping [4, 107]. As previously mentioned, MICP may reduce permeability to mitigate leakage potential (formation trapping). Also, the storage of $CO_2$ might be enhanced by ureolysis-driven MICP by increasing the dissolved $CO_2$ (as carbonate or bicarbonate) in the subsurface formation water (solubility trapping). Finally, ureolysis-driven MICP might enhance the precipitation of dissolved $CO_2$ in carbonate minerals (mineral trapping) [4].

*Formation Trapping.* Engineered MICP has been proposed to protect well cements from supercritical $CO_2$, plug microfractures in the near well environment and reduce permeability in cap rock [4, 5]. In these applications, the spatial extent and temporal efficiency of precipitation must be controlled. Experiments under atmospheric conditions have led to evolved injection strategies to promote more uniform spatial distribution of $CaCO_3$. Pulse flow, with brief fluid injection followed by batch biomineralization periods, rather than continuous flow injections precipitated less $CaCO_3$ near the influent in sand column reactors. Additionally, reducing the saturation index near the injection point during periods of active biomineralization reduced near-injection-point plugging [1, 2, 7, 27]. Recently, these injection strategies have been used to seal hydraulic fractures in 70 cm diameter sandstone cores under ambient [6] and high pressure (Phillips et al. in preparation) conditions.

*Solubility and Mineral Trapping.* Spore and biofilm-forming *Bacillus* species are resistant to high pressures and supercritical $CO_2$ [28, 29]. Accordingly, Mitchell et al. (2010) studied S. *pasteurii*, for ureolysis-driven $CaCO_3$ precipitation with a range of initial $^{13}C$-$CO_2$ head pressures and urea concentration in artificial groundwater. Precipitated $CaCO_3$ was heavily enriched in $^{13}C$-$CO_2$ and the fraction of $^{13}C$-$CO_2$ increased with increasing headspace pressure and urea concentrations, suggesting that ureolysis enhanced the amount of carbonate in the $CaCO_3$ derived from headspace $CO_2$ (g) (mineral trapping). Dupraz et al. (2009) also studied *S. pasteurii* in artificial groundwater to determine the transformation of $CO_2$ into a solid carbonate phase (mineral trapping) under different temperature and salinity conditions (relevant to subsurface saline aquifer conditions) with different $CO_2$ partial pressures. While no temperature dependence of $CaCO_3$ precipitation rates was found in their studies, it was observed that increased salinities increased alkinalization and ureolysis rates, but created a delay in time before $CaCO_3$ precipitation began[107]. Finally, Mitchell et al. (2010) also demonstrated that as pH increases the DIC increases and headspace $CO_2$ (g) decreases (solubility trapping). It was concluded that ureolysis-driven MICP in the subsurface can potentially increase security of long-term $CO_2$ storage. On-going research suggests ureolysis-driven MICP also occurs at high pressures (>73 bar) and those derived minerals are stable when subjected to supercritical $CO_2$ exposure [5].

In summary, control of ureolysis-driven MICP for remediating subsurface environments of strontium contaminated groundwater, toxic metal contaminated soils and groundwater, PCB contaminated concrete or improving security of geologically sequestered $CO_2$ has been widely explored. Research has focused on methods to maintain ureolytic activity and understand the transport and reaction rates of urea and calcium, which influence $CaCO_3$ saturation conditions (Table 2.1). Ureolysis-driven MICP may effectively treat a wide variety of engineering challenges, but care should be taken to consider the maintenance of ureolytic activity (viability of organisms) under adverse contaminant exposure.

## Summary

Much of the literature surrounding ureolysis-driven MICP focuses on controlling the wide-range of parameters that influence precipitation. The range of variables and optimum values determined for specific MICP applications indicates there is not one "recipe" for controlling MICP in engineered applications. The success of MICP treatment depends on the ability to precipitate $CaCO_3$ at appropriate locations and times. Ureolysis-driven MICP is controlled by three main parameters, 1) the ureolytic activity (of microorganisms), 2) the reaction and transport rates of the substrates, and 3) the saturation conditions of carbonate minerals (Table 2.1).

Table 2.1. Summary of control parameters and ranges used to promote microbially-induced calcium carbonate precipitation (MICP).

| **Control Variable** | **Range** | | **General Assessment of Success** | **Relevant References** |
|---|---|---|---|---|
| ***Ureolytic Activity of Organisms*** | | | | |
| Inoculation Conc. | 0.03-2.88 $OD_{600}$<br>$10^5$-$10^9$ cfu/ml | | Greater bacterial concentrations= faster rates of ureolysis & produce larger and less soluble crystals | 12, 41, 50, 66 |
| Microbe | *S. pasteurii, B. lentus, B. megaterium, B. sphaericus, S. ginsengisoli, K. flava, B. pseudofirmus, B. cohnii, B. alkalinitrilicus,* Native organisms or enzyme | | Biofilm communities may have higher activity; stimulation of native ureolytic organisms desirable; strain should have strong urease production, not pathogenic or genetically modified if bioaugmentation is necessary | 39, 50 17, 23, 24, 82 21, 22, 54 42, 77, 80 |
| Carbon Source | BHI, NB, Yeast Extract (YE), Tryptic Soy Broth (TSB), Peptone, Acetate, Lactose Mother or Corn Starch Liquor, Molasses | | Alternate carbon sources may improve economic feasibility for field over lab grade reagents; injection of a carbon source prior to urea may stimulate subsurface attached communities | 4, 17, 30, 40, 50, 73 14, 21, 37 |
| ***Reaction and Transport*** | | | | |
| Flow Condition | Constant Flow | i.e.: 0.7 pore volumes per day; 0.35-12L/hr | Constant low flow rates may lead to non-homogeneous $CaCO_3$ distribution/injection point plugging; higher injection rates = more even distribution of bacteria, homogenous $CaCO_3$ distribution, minimize injection point cementation (ie Damköhler number <<1) | 2, 7, 12, 13, 40, 108 |
| | Pulse Flow | i.e: static intervals between treatments | Growth treatments may be used to overcome mortality due to $CaCO_3$ entombment & supply electron acceptors; pulsed flow may give more homogeneous $CaCO_3$ precipitation | 2, 6, 14, 16, 17, 26, 27, 40, 47, 75, 108, 109 |
| Viscosity | Low (i.e. close to water) to high (polyurethane) | | Low viscosity fluids can penetrate smaller fractures/treatment areas with less pumping pressure; bacterial distribution may be more homogenous in less viscous solutions | 2, 84 |
| Temperature | 10-60 °C | | Increased ureolysis rates observed at higher temperature; urease enzyme can withstand even higher temperatures than mesophilic ureolytically active cells, particularly if immobilized | 45, 50, 55, 56, 63, 82, 88 |

Table 2.1 Continued

| | | | |
|---|---|---|---|
| Salinity | 0.36-100 g/L | Increased salinity often increases alkalinity, ureolysis rates, and bacterial adsorption; increased salinity may increase time delay to $S_{crit}$; phosphates may decrease precipitation rates | 12, 16, 40, 45, 56, 97, 107 |
| ***Saturation Conditions*** | | | |
| pH | 4.5 – 13 | Peak enzyme activity = pH 8.0; optimal *S. pasteurii* growth =pH 8.5; extreme (low and high) pH environments may be detrimental to activity; once formed $CaCO_3$ resilient to acid attack when pH> 1.5 at certain time scales; pH increases after ureolysis are followed by pH decrease due to $CaCO_3$ precipitation | 37, 41, 50, 56, 76, 78, 81, 89, 107, 110 |
| Urea/ $Ca^{2+}$ Conc. | Urea: 6 mM- 1.5 M<br>Calcium: 25μM- 1.25 M | Equimolar urea/$Ca^{2+}$ ratio may be optimal since greater reactant concentration = higher kinetic rates (but only to a certain point) & to balance reagents for reaction but to not add extra unwanted chemicals to environment; calcium nitrate or acetate alternatives to calcium chloride | 2, 16, 17, 26, 40, 41, 45, 50, 67, 75, 76, 83, 99, 107 |
| Saturation state (Ω, S or $S_{crit}$) | 12-436 | Saturation state & critical saturation state influence spatial & temporal precipitation of $CaCO_3$ | 45, 50, 55, 56, 66 |

First, organisms or enzyme are either injected or stimulated to provide the catalyst for ureolysis and cells may act as nucleation sites for precipitation to occur. Several challenges surround maintaining ureolytic activity of microorganisms, such as adverse environmental conditions (e.g. high pH concrete or toxic metals), electron acceptor (e.g. oxygen) limitations, entombment in calcium carbonate, and nutrient diffusion limitations causing cell inactivation after entombment.

Second, the reaction rates and the transport rates of reactants are manipulated, for example, by changing the flow conditions (e.g. velocity) or reagent concentrations. Factors such as fluid salinity and temperature can influence rates of ureolysis and mineral precipitation. Flow rate and fluid viscosities can influence the transport conditions.

Exploring the dimensionless Damköhler number (*Da*), which is the ratio of reaction rate to transport rate, as a tool in MICP design under various conditions may provide valuable insight for controlling ureolysis and precipitation and ultimately the success of MICP engineered applications.

Finally, whether $CaCO_3$ has the thermodynamic propensity to precipitate is governed by the saturation conditions, and the location and timing of precipitation can be influenced by the presence of nucleation sites. Saturation state (S) or saturation index (SI) is determined by the activity of ($Ca^{2+}$ and $CO_3^{2-}$) and $S_{crit}$ or $SI_{crit}$ are empirical values which reflect how highly supersaturated a solution must become before precipitation is actually observed. $S_{crit}$ can be influenced by a variety of factors including but not limited to ureolysis kinetics and the availability of nucleation sites.

A wide range of factors can impact the saturation state to promote precipitation of $CaCO_3$ in engineered MICP technologies (Table 1). Since controlling saturation conditions and precipitation in time and space is a multi-factored reactive transport challenge, modeling has become an essential tool to optimize injection strategies. Current models, carefully interpreted and calibrated, explore promotion of favorable saturation state and predict treatment efficacy while decreasing the need for labor-intensive laboratory experiments [27, 62, 111-113].

Improving the economic and environmental feasibility of ureolysis-driven MICP treatment must be considered in the transition from laboratory to field-relevant scale engineered MICP technologies. There is an economic limitation to the use of laboratory grade nutrient sources in field applications and alternate nutrient sources such as inexpensive industrial wastewater, lactose mother liquor (LML, dairy industry) and corn steep liquor (CSL, starch industry) may offer a possibility of cheaper nutrient sources [4, 10, 30]. Additionally, large volumes of reactant and the production of bacterial cultures for injection (if necessary) may make certain engineered applications of MICP economically challenging compared to traditional treatments. Optimizing treatment strategies may reduce cost by minimizing unnecessary injection or excessive use of amendments. Unwanted by-products from ureolysis MICP, such as $NH_4^+$, have to be considered and controlled at least in certain prospective applications. $NH_4^+$ is undesirable, since groundwater aquifer health may be harmed, stone discolored, or subsurface communities changed by metabolic competition (e.g. outcompeting bioaugmented organisms) due to $NH_4^+$ salts or conversion products [9, 50]. While promising and effective treatment strategies have been demonstrated, additional research is necessary in order to improve economic feasibility, define optimal treatment strategies and reduce unwanted by-products.

## Outlook

With the wide variety of ureolysis-driven MICP applications being researched and developed around the world, there remain a number of technology development challenges and thus research opportunities. In order to improve the potential for successful MICP application, additional strategies have to be developed through further research including, but not limited to:

1. Investigating the potential of biofilm-based MICP approaches compared to suspended cell-based approaches, specifically differences in ureolysis and mineral

precipitation kinetics, mineralogy, and mineral reactivity and stability between attached and planktonic cultures.

2. Determining the optimal substrate balance (e.g. urea and calcium) for various MICP applications with the goal of optimizing $CaCO_3$ precipitation efficiency, which may increase economic feasibility and reduce production of unwanted byproducts.
3. Investigating nano- to micro-scale mineral nucleation processes and determining the effects on subsequent mineral growth, morphology and stability at larger scales.
4. Improving mathematical models describing MICP processes in porous media by developing quantitative descriptions of fundamental processes at the micro- and macro-scale (e.g. ureolysis and growth kinetics, precipitation kinetics, crystal growth and microbe-mineral interactions) as well as integrating these process descriptions into Darcy-scale models for large-scale application design.
5. Experimenting at larger scales, which, together with the developed models, will allow for the evaluation of the importance of transport processes in controlling MICP for engineered field application.
6. Developing *in situ* monitoring technologies (such as geophysical methods) that allow assessment of success in field application.
7. Evaluating long-term stability of MICP treatments compared to conventional (e.g. cement-based) technologies.

It is evident that the implementation of MICP-based technologies on the field scale requires the expertise of many disciplines, and multi-disciplinary research and development teams will be necessary. This review summarizes the research results across many proposed engineered applications in an effort to inspire researchers to address the key research and development questions necessary to move MICP technologies toward commercial scale applications.

In conclusion, ureolysis-driven MICP has been suggested for a wide variety of engineered treatments including modification of construction materials, cementing porous media, hydraulic control and remediating environmental contaminants (Figure 1). A majority of the literature focuses on promoting ureolytic activity, understanding the reaction and transport rate, and ultimately manipulating the saturation conditions to achieve the desired timing and location of $CaCO_3$ precipitation. Many potential applications of ureolysis-driven MICP exist, including those discussed in this review and other applications such as stabilizing building foundations or slopes; minimizing erosion, stabilizing grounds prior to tunneling; sealing tunnel seepage; strengthening earthen dams and dikes; strengthening dunes to protect shorelines or prevent desertification; as well as removing calcium from waste streams[18, 31, 114]. A diverse, multi-disciplinary research effort including field demonstrations, modeling and elucidation of the fundamental mechanisms of ureolysis-driven MICP has and will continue to aid in the effort of transitioning MICP-based technologies from the laboratory to the field.

# CHAPTER THREE

## DARCY SCALE MODELING OF MICROBIALLY INDUCED CARBONATE MINERAL PRECIPITATION IN SAND COLUMNS

### Contribution of Authors and Co-Authors

Manuscript in Chapter 3

Author: Anozie Ebigbo

Contributions: Developed and coded model, performed model calibration and sensitivity analysis. Co-wrote and revised manuscript.

Co-Author: Adrienne J. Phillips

Contributions: Designed and performed experimental work, analyzed data. Co-wrote and revised manuscript.

Co-Author: Robin Gerlach

Contributions: Contributed to experimental design, design of the model and to the revision of the manuscript with comments and feedback.

Co-Author: Rainer Helmig

Contributions: Contributed to the design of the model and revision of the manuscript with comments and feedback.

Co-Author: Alfred Cunningham

Contributions: Contributed to experimental design, design of the model and to the revision of the manuscript with comments and feedback.

Co-Author: Holger Class

Contributions: Contributed to the design of the model and revision of the manuscript with comments and feedback.

## Contribution of Authors and Co-Authors Continued

Co-Author: Lee Spangler

Contributions: Contributed to the revision of the manuscript with comments.

## Manuscript Information Page

Ebigbo, A., Phillips, A.J., Gerlach, Helmig, R., Cunningham, A., Class, H., Spangler, L.
Water Resources Research
Status of Manuscript:
____ Prepared for submission to a peer-reviewed journal
____ Officially submitted to a peer-review journal
____ Accepted by a peer-reviewed journal
_X__ Published in a peer-reviewed journal

American Geophysical Union
Vol. 48, W07519, doi :10.1029/2011WR011714, 2012

## Abstract

This investigation focuses on the use of microbially induced calcium carbonate precipitation (MICP) to set up subsurface hydraulic barriers to potentially increase storage security near wellbores of $CO_2$ storage sites. A numerical model is developed, capable of accounting for carbonate precipitation due to ureolytic bacterial activity as well as the flow of two fluid phases in the subsurface. The model is compared to experiments involving saturated flow through sand-packed columns to understand and optimize the processes involved as well as to validate the numerical model. It is then used to predict the effect of dense-phase $CO_2$ and $CO_2$-saturated water on carbonate precipitates in a porous medium.

## Introduction

Mineral precipitation influenced by microbial activity in the subsurface (particularly through the urea-hydrolysis pathway), commonly referred to as microbially induced calcium carbonate precipitation (MICP), can be exploited for a variety of engineered applications including the immobilization of groundwater contaminants [20-22, 45], ground reinforcement or altering properties of porous materials [12-14, 16, 47], and the creation of hydraulic barriers for purposes such as enhanced oil recovery or increasing storage security of $CO_2$ [1, 2, 19, 111]. Many organisms are capable of hydrolyzing urea, which can alter the saturation state of the formation water, and in the presence of calcium, may favor the precipitation of calcium carbonate [43, 45, 61] .

In previous studies, greater calcium carbonate precipitation was observed near injection sites which could potentially lead to restricted transport of nutrients and have adverse effects on well injectivity [13, 21]. Before a biomineralization technology can be considered field relevant, mineral deposition must be demonstrated to be controllable at a relevant scale while maintaining economic feasibility [12]. Controlling mineralization has been investigated by balancing the reaction with transport, for example, altering injection strategies or injection rates, manipulating the reactant concentrations, increasing the number of applications of treatments, or controlling the distribution of active microbes [9, 12, 13]. Additionally, it has been reported that the types and sizes of crystals formed are affected by the number and form (planktonic or attached) of cells, and that the environmental conditions in surrounding fluids can affect precipitation [39, 40, 50, 56, 66, 107, 110]. Multi-scale and extensive cross-disciplinary research on the feasibility of such a technology is key for its successful implementation [18, 31].

The challenges to creating effective and extensive hydraulic barriers for increasing $CO_2$ storage security are to make efficient use of resources and to promote mineralization in the regions of interest without plugging other regions. Analyzing all combinations of these precipitation-influencing factors in the laboratory would be laborious and time consuming. Several other researchers have utilized models to assist in the understanding or optimization of MICP treatment technologies [62, 112, 113, 115]. The model described in this paper was also developed to quickly analyze parameters and optimize experimental efforts with the aim of improving the understanding of the relevant processes involved. The bench-scale column results and Darcy-scale modeling efforts reported here address the challenge of demonstrating control of mineral deposition (i.e., $CaCO_3$) uniformly along the flow path in a porous medium.

Four separate column experiments were performed in order to: develop an injection strategy to produce homogenous $CaCO_3$ distribution along the length of the column, calibrate the model, and validate the model by comparing it to the physical data.

Finally, while not supported by experimental data, the model also examines some of the potential interactions of dense-phase $CO_2$ with $CaCO_3$. The model simulates two-fluid-phase (water and $CO_2$) experiments, providing a useful tool for the optimization of injection strategies, the design of high-pressure $CO_2$ experiments, and, ultimately, prospective field-scale application.

## Model Description

The system of interest consists of two fluid phases (water and $CO_2$), three immobile phases (rock/porous medium, calcite precipitates, and biofilm), and suspended/ dissolved components (see Figure 3.1).

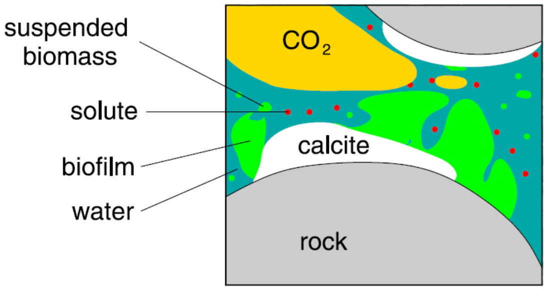

Figure 3.1 Schematic pore scale representation of system of interest.

It shall be noted that other calcium carbonate morphotypes are possible products of the ureolysis-induced calcium carbonate precipitation process described in this work.

However, calcite is the most frequently described calcium carbonate morphotype observed and was chosen as the representative morphotype in this model. In addition, biofilm as described here refers to attached microorganisms capable of producing extracellular polymeric substances (EPS) [7, 39].

Here the system is addressed on the so-called Darcy (macro) scale which is obtained if the processes on the pore (micro) scale can be averaged adequately [116-121]. In this article, the equations and variables of the model are defined on the macro-scale. Thus, only volume-averaged information is available within a *representative elementary volume*.

Definition of System and Main Assumptions. The components the model accounts for include water (w), carbon dioxide ($CO_2$), suspended biomass (b), attached biomass/biofilm (f), substrate (s), electron acceptor/oxygen (e), calcite (c), urea (u), ammonia/ammonium (a), calcium ($Ca^{2+}$), chloride ($Cl^-$), and sodium ($Na^+$).

Two fluid phases may be present in the pores of the porous medium (water [w] and $CO_2$ [n]), which are the wetting and the nonwetting phases, respectively. Before the injection of $CO_2$, only water is present. Thus, the set of primary variables can change depending on the number of phases present [122].

The water phase consists of the components water, dissolved $CO_2$, suspended biomass, substrate, oxygen, urea, ammonia/ammonium, calcium, chloride, and sodium. The $CO_2$ phase consists of $CO_2$, water, and oxygen. All other components are assumed not to dissolve/partition into this phase. Calcite and biofilm are immobile.

Even though brines consist of several salts, it is assumed here that their combined effect on density, viscosity, and $CO_2$ solubility can be represented by an equivalent sodium chloride concentration [123].

There is no differentiation between molecularly dissolved $CO_2$ and carbonic acid. The sum of both is referred to as $H_2CO_3$ [124, 125].

In the explanations and diagrams that follow, it is assumed that the host rock (or other porous medium) does not contain significant amounts of carbonate minerals. However, if this is not the case, the amount of calcite initially present in the model can be set to a nonzero value.

Chemical Reactions. In the presence of the enzyme urease, urea is hydrolyzed to give ammonia and carbonic acid. The bacterial strain *Sporosarcina pasteurii* is capable of producing large amounts of urease [126]. The subsequent protonation of ammonia to ammonium causes an increase in pH, shifting the equilibrium of the calcite precipitation/dissolution reaction toward precipitation by increasing the availability of the carbonate ion ($CO_3^{2-}$).

| | |
|---|---|
| $CO(NH_2)_2 + H_2O \xrightarrow{\text{Urease}} NH_2COOH + NH_3$ | ureolysis |
| $2NH_3 + 2H_2O \longrightarrow 2NH_4^+ + 2OH^-$ | protonation of ammonia |
| $H_2CO_3 + OH- \longleftrightarrow HCO_3^- + H_2O$ | dissociation of carbonic acid |
| $HCO_3^- + 2OH^- \longleftrightarrow CO_3^{2-} + H_2O$ | dissociation of bicarbonate ion |
| $Ca^{2+} + CO_3^{2-} \longleftrightarrow CaCO_3\ (s)$ | calcite precipitation/dissolution |

The dissociation reactions are fast compared to ureolysis, precipitation, and dissolution. Hence, these are assumed to occur instantaneously and are accounted for with equilibrium coefficients. Slower reactions are described by using rate expressions.

*Rate of Ureolysis.* As described by Fidaleo and Lavecchia [2003], the rate of urea hydrolysis is given by,

$$r_{urea} = v_{max} Z_{ub} \frac{m_u}{(K_u+m_u)\left(1+\frac{m_{NH_4^+}}{K_{NH_4^+}}\right)} \qquad (1)$$

where $m_u$ is the molality of urea, $K_u$ is the Monod half-saturation constant, and $K_{NH4}^+$ is an inhibition parameter due to high $NH_4^+$ concentrations. The maximum rate of ureolysis $v_{max}$ is calculated as follows:

$$v_{max} = \frac{k}{1+\frac{m_{H^+}}{K_{EU,1}}+\frac{K_{EU,2}}{m_{H^+}}} \qquad (2)$$

Dissociation constants for the enzyme-urea complex are denoted by $K_{EU,1}$, and k is a rate constant. Note that these rate expressions from Fidaleo and Lavecchia [2003] were determined for jack bean urease. It is assumed here that the same expressions can be used for microbially produced urease. The concentration of intra- and extracellular urease in the porous medium $Z_{ub}$ is difficult to determine [127]. Urease is released when bacterial cells rupture and may sorb to polymers of the biofilm and to the porous medium [126, 128, 129]. For the purposes of this model, it is assumed that most of the urease is associated with the biofilm (either intracellularly or sorbed to biofilm polymers). Hence, the amount of urease is assumed to be related nonlinearly to the amount of attached biomass (i.e., biofilm),

$$z_{ub} = k_{ub}\left(\varrho_f \phi_f\right)^{n_{ub}} \qquad (3)$$

Suspended biomass is not included since its contribution is considered small compared to that of the biofilm [130, 131]. Here $\rho_f$ is the biofilm density (dry mass per unit volume), $\varphi_f$ is the volume fraction of the porous medium occupied by the biofilm, $k_{ub}$ is a proportionality coefficient and $n_{ub}$ accounts for the nonlinear dependence of $Z_{ub}$ on $\rho_f\,\varphi_f$.

*Rate of Calcite Precipitation/Dissolution.* The net rate of precipitation or dissolution of calcite is governed by the calcite saturation state Ω which provides a measure of the distance of the system from equilibrium, i.e., Ω =1,

$$\Omega = \frac{\gamma_{Ca^{2+}} m_{Ca^{2+}} \gamma_{CO_3^{2-}} m_{CO_3^{2-}}}{K_{sp}} \tag{4}$$

The activity coefficients $\gamma Ca^{2+}$ and $\gamma CO_3^{2-}$ are calculated using Pitzer equations as described by Wolf et al. [1989], Millero et al. [1984], and Clegg and Whitfield [1995] [132-134]. To this end, the influence of the interactions of all the ions considered are included in the calculations. However, the concentrations of some of the ions are determined using apparent dissociation coefficients as described in section below. Figure 3.2 shows how the activities of calcium and carbonate ions vary with chloride concentration in NaCl and $CaCl_2$ solutions. $K_{sp}$ is the solubility product of calcite.

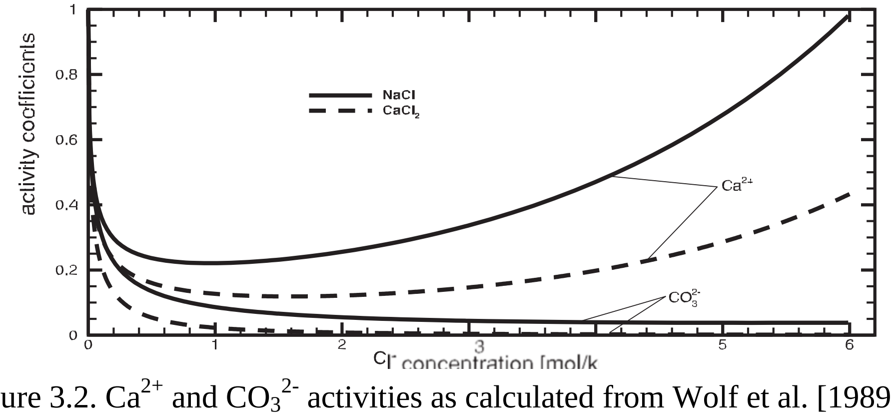

Figure 3.2. $Ca^{2+}$ and $CO_3^{2-}$ activities as calculated from Wolf et al. [1989], Millero et al. [1984], and Clegg and Whitfield [1995] using Pitzer equations as a function of Cl- concentration in NaCl and $CaCl_2$ solutions.

The rate at which equilibration occurs is assumed to depend on the distance from equilibrium. When Ω> 1, net precipitation occurs, and net dissolution occurs when Ω < 1. There are several empirical approaches for determining these rates. There are also some approaches which obtain the rates from the up-scaling of pore-scale processes [117, 120]. Here common empirical rate functions for precipitation and dissolution are chosen [135],

$$r_{prec} = k_{prec} A_{sw} (\Omega - 1)^{n_p} \qquad \text{for } \Omega \geq 1 \qquad (5)$$

The empirical parameters $k_{prec}$ and $n_p$ are available in the literature [e.g., Zhong and Mucci, 1989] [135] . The specific interfacial surface between solid (i.e., both porous matrix and calcite) and water phases $A_{sw}$ is estimated from the porosity φ with an empirical relation [e.g., Clement et al., 1996] as follows:

$$A_{sw} = A_{sw,0} \left(1 - \frac{\varphi_c}{\varphi_0}\right)^{\frac{2}{3}} \qquad (6)$$

The subscript ‘‘0’’ denotes initial values.

Similarly, the dissolution rate is calculated as given by [124, 136],

$$r_{diss} = \left(k_{diss,1} m_{H^+} + k_{diss,2}\right) A_{cw} (1 - \Omega)^{n_d} \qquad (7)$$

Again, $k_{diss,1}$, $k_{diss,2}$, and $n_d$ are empirical parameters. $A_{cw}$ is the specific interfacial surface between calcite and water phases. Assuming the porous rock matrix originally in place does not dissolve, $A_{cw}$ may differ significantly from $A_{sw}$ as shown in Figures 3 and 4. For small values of φc (which is the volume fraction of porous medium occupied by calcite), $A_{cw}$ is proportional to $\varphi_c$, i.e.,

$$A_{cw} = a_c \varphi_c \qquad (8)$$

where $a_c$ represents the specific surface area of the calcite grains (surface area per volume of calcite). However, when significant amounts of calcite are present in the porous medium, i.e., for large $\varphi_c$, this relationship is not valid. Instead, $A_{cw}$ and $A_{sw}$ become equivalent. Thus, $A_{cw}$ is chosen in such a way that the limiting of the two options, i.e., the smaller of the two is chosen (see also Figures 3.3 and 3.4):

$$A_{cw} = min(A_{sw} a_c \varphi_c) \qquad (9)$$

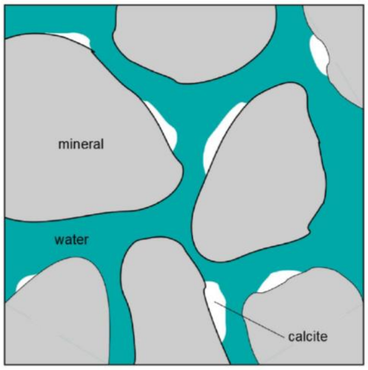

Figure 3.3. Solid-water interfacial areas: At low values of $\varphi_c$, the interfacial surface between calcite and water phases, $A_{cw}$, and that between solid (i.e., both porous matrix and calcite) and water phases, $A_{sw}$, differ significantly, $A_{cw} < A_{sw}$.

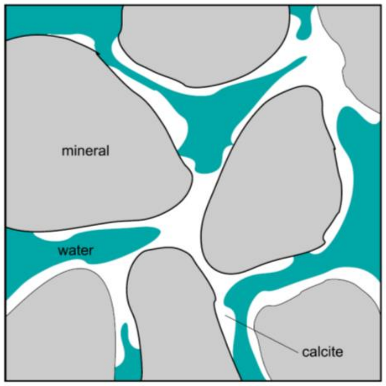

Figure 3.4. Solid-water interfacial areas: At high values of $\varphi_c$, the interfacial surface between calcite and water phases, $A_{cw}$, and that between solid (i.e., both porous matrix and calcite) and water phases, $A_{sw}$, are equivalent, $A_{cw} \approx A_{sw}$.

*Dissociation Coefficients* The dissociation of $NH_3$ and $H_2CO_3$ in water are accounted for with apparent (i.e., stoichiometric) dissociation coefficients. Calculating activity coefficients as is done for the computation of Ω would unnecessarily increase the complexity and computational cost of the model. As such, correlations from literature are chosen, with which one can determine the apparent dissociation coefficients as functions of ionic strength I,

$$K_a^*(I) = \frac{m_{NH_3} m_{H^+}}{m_{NH_4^+}} \quad \text{dissociation of ammonia} \qquad (10)$$

$$K_1^*(I) = \frac{m_{HCO_3^-} m_{H^+}}{m_{H_2CO_3}} \quad \text{dissociation of carbonic acid} \qquad (11)$$

$$K_2^*(I) = \frac{m_{CO_3^{2-}} m_{H^+}}{m_{HCO_3^-}} \quad \text{dissociation of bicarbonate ion} \qquad (12)$$

$$K_w^*(I) = m_{H^+} m_{OH^-} \quad \text{dissociation of water} \qquad (13)$$

For $H_2CO_3$, dissociation coefficients are calculated using correlations given by Millero et al. [2007], and those by Bell et al. [2008] are used for the dissociation of $NH_3$ [137, 138]. The dissociation coefficient of water is also required and approximated as a function of ionic strength [139].

Mass Balance Equations. Mutual dissolution of the water and $CO_2$ phases are accounted for with the mass fractions $X_w^{CO_2}$ and $X_n^w$ which represent the amount of $CO_2$ in the water phase and of water in the $CO_2$ phase, respectively. Equations which balance the mass of each component in the phases α can be written as in equation (14),

$$\sum_\alpha \left\{ \frac{\partial}{\partial t}(\phi \varrho_\alpha X_\alpha^i S_\alpha) + \nabla \times (\varrho_\alpha X_\alpha^i \mathbf{v}_\alpha) - \nabla \times (\varrho_\alpha \mathbf{D}_\alpha \nabla X_\alpha^i) \right\} = q^i;$$

$$i \in \{\mathrm{w}, \mathrm{CO_2}\},\ \alpha \in \{\mathrm{w}, \mathrm{n}\}. \qquad (14)$$

Here ρ is density, S is the fluid-phase saturation within the rock pores, v is the Darcy flux (fluid-phase velocity), **D** is the hydrodynamic dispersion tensor, and q represents sources/sinks.

The components which are assumed to exist exclusively as dissolved/suspended components of the water phase can be expressed with concentrations C and the following mass balance equations hold,

$$\frac{\partial}{\partial t}(\phi S_{\mathrm{w}} C_{\mathrm{w}}^{j}) + \nabla \times (C_{\mathrm{w}}^{j} \mathbf{v}_{\mathrm{w}}) - \nabla \times (\mathbf{D}_{\mathrm{w}} \nabla C_{\mathrm{w}}^{j}) = q^{j};$$
$$j \in \{\mathrm{b}, \mathrm{s}, \mathrm{u}, \mathrm{a}, \mathrm{Ca}^{2+}, \mathrm{Cl}^{-}, \mathrm{Na}^{+}\}. \qquad (15)$$

Oxygen can be present in both water and $CO_2$. Thus, the mass balance equation for oxygen is,

$$\sum_{\alpha} \left\{ \frac{\partial}{\partial t}(\phi S_{\alpha} C_{\alpha}^{\mathrm{e}}) + \nabla \times (C_{\alpha}^{\mathrm{e}} \mathbf{v}_{\alpha}) - \nabla \times (\mathbf{D}_{\alpha} \nabla C_{\alpha}^{\mathrm{e}}) \right\} = q^{e};$$
$$\alpha \in \{\mathrm{w}, \mathrm{n}\}. \qquad (16)$$

Additionally, the equations for the immobile phases, attached biomass, and calcite are,

$$\varrho_k \frac{\partial \phi_k}{\partial t} = q^k ; \qquad k \in \{\mathrm{f}, \mathrm{c}\} . \qquad (17)$$

<u>Sources and Sinks.</u> The sources and sinks given in equations (14)–(17) accounting for reactions (urea hydrolysis, precipitation, dissolution) and bacterial activity are described in detail in the following [cf. Ebigbo et al., 2010]:

Suspended and attached biomass: $q^b = r_g^b - r_b^b - r_a + r_d$ (18)

and $q^f = r_g^f - r_b^{bf} + r_a - r_d$ (19)

where $r_g^b$ and $r_g^f$ and are growth rates for suspended and attached biomass, respectively; and $r_b^b$ and $r_b^f$ the corresponding decay rates; and $r_a$ and $r_d$ and are the rates of attachment to and detachment from the biofilm, respectively[140],

$$r_{\mathrm{g}}^{\mathrm{b}} = \mu \phi S_{\mathrm{w}} C_{\mathrm{w}}^{\mathrm{b}}, \tag{20}$$

$$r_{\mathrm{g}}^{\mathrm{f}} = \mu \phi_{\mathrm{f}} \varrho_{\mathrm{f}}. \tag{21}$$

The growth coefficient is calculated with double-Monod kinetics[141],

$$\mu = k_{\mu} \frac{C_{\mathrm{w}}^{\mathrm{s}}}{K_{\mathrm{s}} + C_{\mathrm{w}}^{\mathrm{s}}} \cdot \frac{C_{\mathrm{w}}^{\mathrm{e}}}{K_{\mathrm{e}} + C_{\mathrm{w}}^{\mathrm{e}}}. \tag{22}$$

Here $k_\mu$ is the maximum substrate utilization rate, and $K_s$ and $K_e$ are half-saturation coefficients. Decay rates are calculated as first-order relationships with respect to live-cell concentrations,

$$r_{\mathrm{b}}^{\mathrm{b}} = b_{\mathrm{b}} \phi S_{\mathrm{w}} C_{\mathrm{w}}^{\mathrm{b}}, \tag{23}$$

$$r_{\mathrm{b}}^{\mathrm{f}} = b_{\mathrm{f}} \phi_{\mathrm{f}} \varrho_{\mathrm{f}}, \tag{24}$$

where $b_b$ and $b_f$ are decay coefficients. They comprise constant endogenous decay $b_0$ and process-dependent decay $b^\kappa$ ($\kappa$ ε b, f). For the suspended biomass, $b^b$ is assumed to be primarily dependent on pH. Since *Sporosarcina pasteurii* is an alkaliphile, only low pH conditions due to high $CO_2$ concentrations in water are taken to be harmful to the bacterial cells. In addition, it is assumed that the biofilm bacteria are protected from the adverse effects of $CO_2$. This assumption is supported by the findings of Mitchell et al. [2008] in which they propose mechanisms which contribute to the protective nature of the biofilm including mass transfer resistance offered by the biofilm structure and immobilization of $CO_2$ molecules due to their interaction with the extracellular polymers of the biofilm. Thus, the following decay relationship is chosen[142]:

$$b^{\mathrm{b}} = b_0 \left( 1 + \frac{m_{\mathrm{H^+}}^2}{K_{\mathrm{pH}}} \right) , \qquad (25)$$

where $K_{pH}$ is an empirical constant.

Precipitation of calcite occurs mainly in and on the biofilm [7, 143]. This can lead to inactivation of bacterial cells embedded in the biofilm, either by disruption when a calcite nucleus develops within a cell or due to a coating of the cells by the calcite (which effectively leads to inactivation) [9, 13, 52, 56]. Thus, $b^f$ is a function of the calcite precipitation rate:

$$b^{\mathrm{f}} = b_0 + \frac{r_{\mathrm{prec}} M_{\mathrm{CaCO_3}}}{\varrho_{\mathrm{c}}(\phi_0 - \phi_{\mathrm{c}})} . \qquad (26)$$

Equation (26) assumes that the rate of inactivation due to precipitation is inversely proportional to the free space available for precipitation, $\varphi_0$- $\varphi_c$.

As in the work of Ebigbo et al. [2010], attachment and detachment rates are calculated as follows:

$$r_{\mathrm{a}} = k_{\mathrm{a}} \phi S_{\mathrm{w}} C_{\mathrm{w}}^{\mathrm{b}} , \qquad (27)$$

$$r_{\mathrm{d}} = k_{\mathrm{d}} \phi_{\mathrm{f}} \varrho_{\mathrm{f}} . \qquad (28)$$

The attachment [cf. Taylor and Jaffé, 1990] and detachment [cf. Rittmann, 1982; Speitel and DiGiano, 1987][144, 145] coefficients are given by,

$$k_{\mathrm{a}} = c_{\mathrm{a},1} \phi_{\mathrm{f}} + c_{\mathrm{a},2} , \qquad (29)$$

$$k_{\mathrm{d}} = c_{\mathrm{d},1} (\phi S_{\mathrm{w}} |\nabla p_{\mathrm{w}} - \varrho_{\mathrm{w}} \mathbf{g}|)^{0.58} + c_{\mathrm{d},2} \mu . \qquad (30)$$

The parameters, $c_{a,1}$, $c_{a,2}$ and $c_{d,1}$, are all constants [111, 140], p is fluid-phase pressure, and **g** is the gravity vector. Speitel and DiGiano [1987] fit the value of $c_{d,2}=0.665$, whereas Ebigbo et al. [2010] obtained a better fit in their model with $c_{d,2}=6\varphi_f$ [111, 145]. In this model, better results were obtained with an expression similar to the latter approach. However, since it is required that $0 \leq c_{d,2} \leq 1$ and that the influence of reduced pore space due to precipitation needs to be included,

$$c_{\mathrm{d},2} = \frac{\phi_{\mathrm{f}}}{\phi_0 - \phi_{\mathrm{c}}},$$ was used to calculate $c_{d,2}$. (31)

Substrate: $q^{\mathrm{s}} = -(r_{\mathrm{g}}^{\mathrm{b}} + r_{\mathrm{g}}^{\mathrm{f}})/Y$ where Y is the yield coefficient. (32)

Electron acceptor (oxygen): $q^{\mathrm{e}} = -F \times (r_{\mathrm{g}}^{\mathrm{b}} + r_{\mathrm{g}}^{\mathrm{f}})/Y.$ (33)

The coefficient F quantifies the amount of oxygen consumed per unit mass of substrate [146].

Urea: $q^{\mathrm{u}} = -r_{\mathrm{urea}} M_{\mathrm{urea}}.$ (34)

Ammonia: $q^{\mathrm{a}} = 2 r_{\mathrm{urea}} M_{\mathrm{NH_3}}.$ (35)

Calcite: $q^{\mathrm{c}} = (r_{\mathrm{prec}} - r_{\mathrm{diss}}) M_{\mathrm{CaCO_3}}.$ (36)

Calcium: $q^{\mathrm{Ca^{2+}}} = (r_{\mathrm{diss}} - r_{\mathrm{prec}}) M_{\mathrm{Ca^{2+}}}.$ (37)

$CO_2$: $q^{\mathrm{CO_2}} = (r_{\mathrm{diss}} - r_{\mathrm{prec}} + r_{\mathrm{urea}}) M_{\mathrm{CO_2}}.$ (38)

Water, sodium, and chloride: $q^{\mathrm{w}} = q^{\mathrm{Na^+}} = q^{\mathrm{Cl^-}} = 0.$ (39)

Charge Balance. With the charge balance equation, it is possible to calculate pH,

$$\sum_i z_i m_i = 0,$$

where $z_i$ is the charge of the ion i. (40)

Numerical Model. Some supplementary equations are required to complete the description of the model. The mass balance equations form a system of 10 partial (equations (14)–(16)) and two ordinary (equation (17)) differential equations. These are implemented, as outlined by Ebigbo et al. [2010], in MUFTE-UG using a vertex-centered finite-volume scheme and a fully implicit time discretization.

Depending on the conditions at hand, the sources and sinks, which arise from the chemical and biological reactions, can impose a very strong coupling on the set of equations. In addition, constitutive relationships such as the permeability-porosity function augment this coupling and increase the nonlinear character of the system. Hence, an efficient numerical solution is challenging.

Time-step sizes are automatically adapted to the rate of convergence that depends on the rate at which the processes occur. The process which has the highest influence on time-step size in this model is the rate of calcite precipitation. High-saturation states can lead to very fast precipitation events which, of course, reduce the time step size. In the simulations conducted in this study, the time step sizes ranged from several seconds to several hours.

More information on MUFTE-UG is available in the work of Assteerawatt et al. [2005] and Helmig et al. [1998][147, 148].

## Experiments: Saturated Flow Through Sand-Packed Columns

Laboratory experiments involving saturated flow through sand-packed columns were carried out to optimize the precipitation process and validate part of the numerical model. As previously described [2], vertically positioned columns (61 cm in length, 2.54 cm in diameter) were packed with 40 mesh (0.5 mm effective filtration size) quartz sand (Unimin Corporation, Emmet, ID) under water to minimize air inclusions. Columns were disinfected and rinsed by injecting two pore volumes followed by 30 min stagnation periods of each of the four following solutions:

- 1% bleach (Clorox, Oakland, Calif.) v/v and 3.5% Tween 80 (Acros, N. J.) w/v solution ;
- 10% w/v NaCl (Fisher, Fair Lawn, N. J.) solution ;
- 1.26% w/v sodium thiosulfate (Fisher, Fair Lawn, N. J.) solution ; and
- 10% w/v ammonium chloride (Fisher, Fair Lawn, N. J.) solution.

Cultures of *Sporosarcina pasteurii* were grown overnight from a frozen stock culture and washed via centrifugation and resuspened in fresh sterile medium prior to injection into the column in up-flow configuration. A cell attachment period (no flow) of ~6 h was followed by 18 h of pumping growth medium to develop biofilm. After biofilm establishment and an overnight delay, two pore volumes of calcium-rich (1.25 M calcium) growth medium were injected to initiate biomineralization. The columns were then allowed to remain static for 24 h (biomineralization stage). For columns 2–4, calcium-rich medium from the first 7.6 cm of the columns was displaced immediately after injection with calcium-free medium to minimize injectivity reduction near the injection point. Between biomineralizing stages, the columns were flushed with two pore volumes of calcium and urea-free medium to restore a low saturation state. Periodically, throughout the experiments, the biofilm was resuscitated by injecting at least two pore volumes of fresh growth medium without calcium. Flow rates were controlled by a Masterflex (model 755370) pump and controller (Cole Parmer, Vernon Hills, Ill.). The filling and flushing strategy for all four columns is described in Table 1. The experiments were terminated when the systems' pressure limits were reached. However, column 4 was terminated when as much calcium had been injected as for columns 2 and 3.

Table 3.1. Column injection summary

| Column | Biomass concentration of Inoculum (cfu/ml) | $Ca^{2+}$ Rich Medium Pulses | Mass of Total $Ca^{2+}$ Injected (g) | Resuscitation Events | Avg. Flow Rate (mL $s^{-1}$) | Rinse Influent Region |
|---|---|---|---|---|---|---|
| 1 | $4.0x10^9$ | 35 | 303.4 | 15 | 10.7 | No |
| 2 | $1.1x10^8$ | 20 | 130.3 | 10 | 8.0 | Yes |
| 3 | $6.2x10^9$ | 11 | 83.3 | 4 | 8.9 | Yes |
| 4 | $1.3x10^7$ | 22 | 135.2 | 9 | 9.1 | Yes |

Growth medium was prepared by mixing 3 g of Difco Nutrient Broth (BD, Sparks, Md.), 20 g of urea (Fisher, Fair Lawn, N. J.), 10 g of ammonium chloride (Fisher, Fair Lawn, N. J.), and 185 g of calcium chloride dihydrate (not included in calcium-free growth medium) (Acros, N. J.) and stirring continuously until dissolved in 1 L of nanopure water. As necessary, the pH of the medium was adjusted to between 6.0 and 6.3 (the final pH of calcium-rich medium was 5.4–5.6).

Monitoring and Sampling Methods. Column effluent was collected and monitored for ammonium and residual calcium concentration after each biomineralization stage. A portion of the effluent sample was filtered using a 0.2 μm SFCA Corning syringe filter

(Corning Incorporated, N. Y.) and analyzed with a modified Nessler assay for ammonium production. The unfiltered remainder of the effluent sample was used to monitor pH.

During the experiments, the activity in the column was monitored as follows:

1. Ammonium concentration was determined with a modified Nessler assay; effluent samples were diluted in deionized water and compared to standards made from $(NH_4)_2SO_4$. Each sample and standard (250mL) was added in triplicate to a 96-well microplate (Fisher, Fair Lawn N. J.) to which 3 mL of mineral stabilizer and polyvinyl alcohol, and 10 mL of Nessler reagent (potassium tetraiodomercurate(II)) (Hach, Loveland, Colo.) were added. Ammonium concentration was quantified in the resulting solution after 13 min reaction time via spectrophotometry at 425 nm (Bio-Tek, Synergy HT).
2. The pH of effluent samples was assessed with a Fisher Scientific pH meter (model 50) equipped with a Corning glass electrode, which was calibrated daily with pH 7 and 10 buffers.

At the termination of the experiment, each column was destructively sampled by cutting it into eight 7.6 cm sections and digesting triplicate portions of each section's sand contents with 10% trace-metal grade nitric acid (Fisher, Fair Lawn, N. J.). Calcium analysis was performed on an Agilent 7500 ICPMS after a 1:5000 or 1:10,000 dilution in 5% trace-metal grade nitric acid (Fisher, Fair Lawn, N. J.) and compared with certified standards (Agilent Technologies, Environmental Calibration Standard 5183–4688) to estimate the total $CaCO_3$ mineral per mass of sand.

Additionally, images and elemental maps were acquired using the Zeiss Supra 55VP scanning electron microscope located in the Imaging and Chemical Analysis Laboratory at Montana State University. $CaCO_3$ precipitates on sand samples were air-dried and sputter coated with iridium. High resolution images were taken at 1.0 kV at a working distance of 4.0 mm. Elemental analysis with energy dispersive X-ray spectroscopy (EDS) was per formed at 20 kV and a working distance of 15 mm.

Results and Discussion. *Residual-Effluent Analysis.* $CaCO_3$ precipitation may inactivate microorganisms or create nutrient diffusion limitations [13, 52, 75, 107], leading to reduced ureolysis and subsequently less biomineralization. It has also been hypothesized that larger carbonate crystals, less likely to re-dissolve, are produced when greater bacterial concentrations are present during ureolysis [63]. As such, the biofilm was periodically resuscitated by injecting at least two pore volumes of fresh growth medium without calcium to stimulate the recovery of bacterial populations after precipitation events [56]. Both residual-effluent populations and $NH_4^+$ concentrations (an indication of ureolysis) are greater directly after the biofilm resuscitation events, while these parameters were observed to decrease during active biomineralization periods (Figure 3.5).

Directly after resuscitation events, effluent pH was restored to above 9 and the $NH_4^+$ concentrations rose to above 12 g $L^{-1}$, while during active biomineralizing periods, the pH averaged 6.9 and $NH_4^+$ concentrations dropped as low as 5.1 g $L^{-1}$.

*Distribution of $CaCO_3$ Deposition.* Unlike columns 2–4, column 1 did not employ a calcium-medium displacement strategy for the injection region. As described previously and observed by other researchers [2, 13, 30, 112], higher $CaCO_3$ concentrations per mass of sand were observed in column 1 in the first section near the injection point. Concerns regarding locally reduced injectivity near the injection point of the column [1, 13, 21] led to a modified injection strategy (used for columns 2–4) which involved rinsing $Ca^{2+}$ rich medium from the influent area before significant ureolysis, and thus $CaCO_3$ precipitation could occur. Favorable results of homogeneous $CaCO_3$ distribution were achieved for columns 2–4 as shown in Figures 3.6–3.8. The average $CaCO_3$ contents from each column study are summarized in Table 3.2.

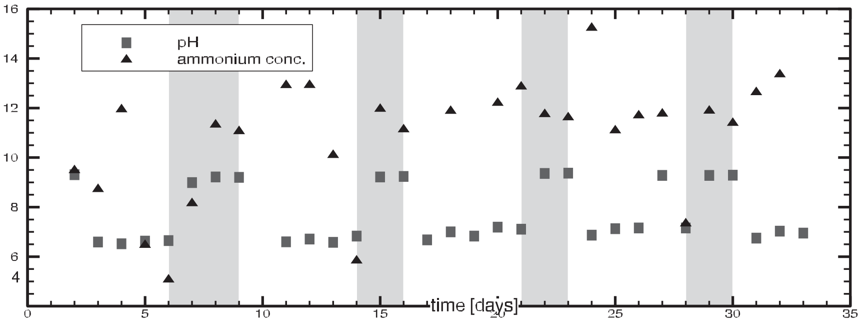

Figure 3.5. Effluent $NH_4^+$ concentration and pH data from column 4. Gray areas indicate resuscitation periods. Although not presented here, similar results were observed for the other columns. Note that the injected medium contained 3.4 g $L^{-1}$ of $NH_4^+$.

Table 3.2. Average concentration per column section (§) per experiment (mg $CaCO_3$/per gram of sand)

| Exp # | §1 | §2 | §3 | §4 | §5 | §6 | §7 | §8 |
|---|---|---|---|---|---|---|---|---|
| 1 | 479 ± 29 | 256 ± 61 | 274 ± 30 | 227± 29 | 250 ± 74 | 254 ± 71 | 211 ± 22 | 202 ± 73 |
| 2 | 222 ± 30 | 193 ± 13 | 196 ± 10 | 188 ± 8 | 174 ± 6 | 178 ± 10 | 169 ± 15 | 173 ± 24 |
| 3 | 150 ± 10 | 136 ± 6 | 130 ± 4 | 154 ± 29 | 132 ± 12 | 133 ± 11 | 134 ± 6 | 201 ± 34 |
| 4 | 112 ± 18 | 165 ± 40 | 141 ± 40 | 118 ± 21 | 117 ± 24 | 121 ± 12 | 117 ± 8 | 109 ± 8 |

To obtain $\varphi_c$, the ICPMS results were converted assuming $\rho_c$= 2710 g $L^{-1}$ and $\varphi_0$ = 0.4, in order to make direct comparisons to the model output results.

## Model Validation

The numerical model was calibrated using the experimental data for $\varphi_c$ of the first two experiments (i.e., columns 1 and 2) in Table 2. The columns are idealized as 80 cm one dimensional reactors, purposefully longer than the length of the experimental column (61 cm) to reduce the effect of the boundary conditions at the effluent on the simulations.

The initial conditions were:

1. $p_w$ = 1.01325 bar at the top of the column (effluent) and a hydrostatic pressure profile in the rest of the column;
2. $X_w^{CO_2}$ = 5.8 x $10^{-7}$ g/g (i.e., 5.8 x $10^{-4}$ g $L^{-1}$);
3. $C_w^s$= 3 g $L^{-1}$;
4. $C_w^e$ = 0.008 g $L^{-1}$;
5. $NH_4Cl$ concentration (from which $C_w^a$ and $C_w^{Cl}$ can be calculated): 10 g $L^{-1}$;
6. $C_w^{Na}$ is adjusted such that the pH of the solution matches the experimental value, i.e., 6.2. All other components are not present initially.

Flux boundary conditions were used at the inlet for all components. The water-inflow velocity was chosen to match those of the experiments (see Table 3.1). The fluxes of the dissolved/suspended components depended on the composition of the injected solution. Calcium-free solutions were identical to the solution initially present in the column. Additionally, the flux of $NaCl_2$ during the injection of the calcium-rich solution was chosen such that it corresponded to a $NaCl_2$ concentration of 139.7 g $L^{-1}$ (which corresponds to 185 g $L^{-1}$ of $CaCl_2 \cdot 2H_2O$), and that of $Na^+$ such that the pH equals 5.4 (no significant dissolution of calcite is expected due to the high calcium concentrations).

Column inoculation was simulated by setting a biomass flux for 15 min at the inlet corresponding to the bacterial concentrations listed in Table 3.1. It is assumed here that the dry cell weight is 2.5 x $10^{-13}$ g/cfu [149].

After the biofilm was established (t ≈ 2 d), the strategy was generally to inject two pore volumes each of the calcium-free and calcium-rich solutions, a small amount (equivalent to the pore volume of the first 7.6 cm of the porous medium column) of calcium-free solution (not for column 1) to minimize precipitation at the inlet, and then shutting off the injection (no flow) for ~24 h. This cycle was repeated for the duration of each experiment. In addition, periodic resuscitation (injection of at least two pore volumes of calcium-free growth medium) was simulated as appropriate. The various injections and rest periods carried out in the different experiments are reproduced by the model. It should be noted that, in the experiments, the columns are not geomechanically confined. Volume changes, which may be caused by calcite precipitation, are not accounted for by the model. At the effluent, all boundary conditions are Dirichlet and set to zero, except the pressure which is atmospheric.

The parameters used for the simulations are shown are shown in Table 3.3. Six parameters were fitted, including $\rho_f$ , $k_\mu$, $c_{a,1}$ , $c_{a,2}$ , $k_{ub}$ , and $n_{ub}$. This was done manually by varying these parameters within plausible ranges of validity (see footnotes in Table 3.3) to match the calcite distribution along the columns in the experiments.

Table 3.3 Parameters used for simulation of the experiment

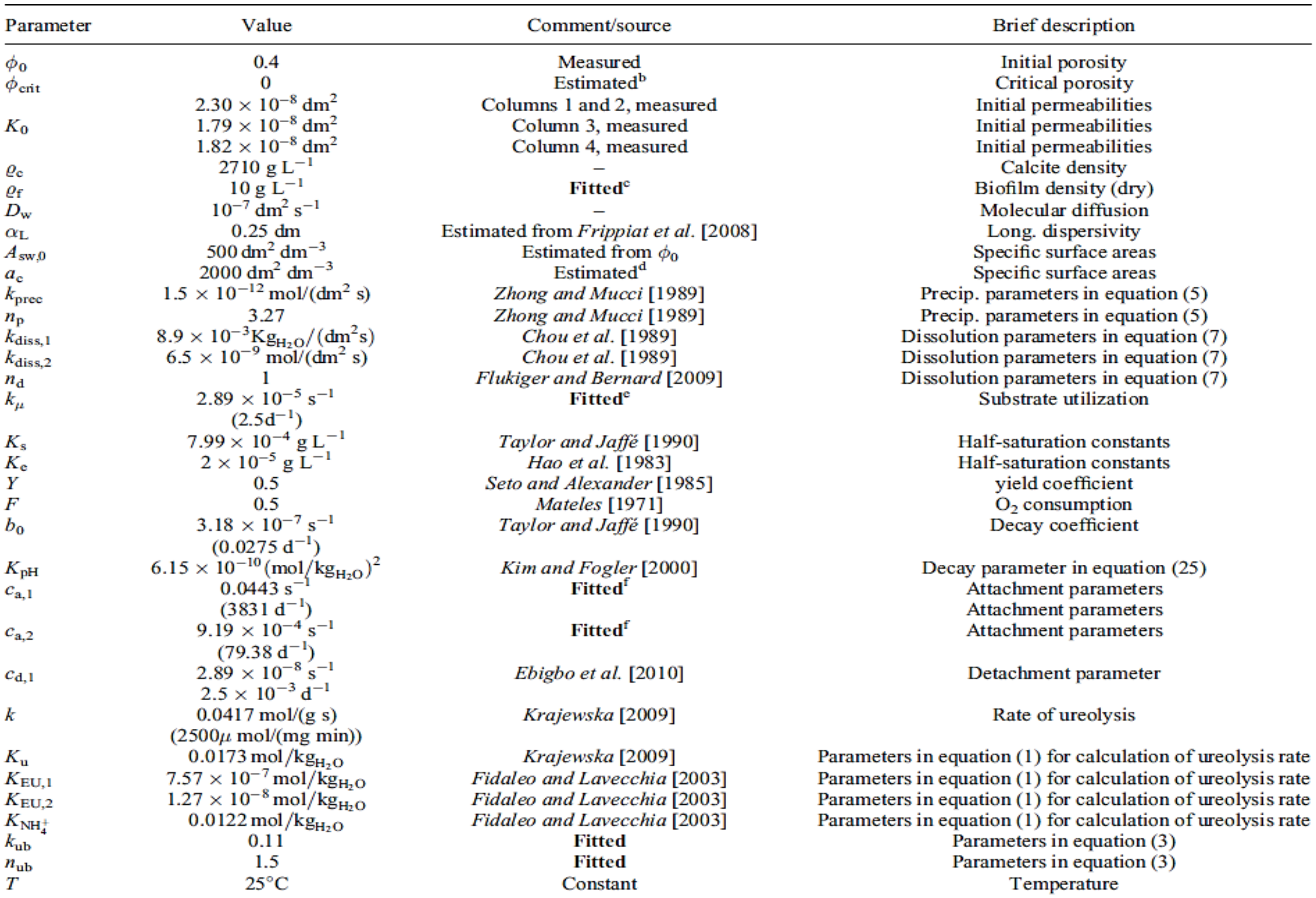

| Parameter | Value | Comment/source | Brief description |
|---|---|---|---|
| $\phi_0$ | 0.4 | Measured | Initial porosity |
| $\phi_{crit}$ | 0 | Estimated[b] | Critical porosity |
| $K_0$ | $2.30 \times 10^{-8}$ dm$^2$ | Columns 1 and 2, measured | Initial permeabilities |
|  | $1.79 \times 10^{-8}$ dm$^2$ | Column 3, measured | Initial permeabilities |
|  | $1.82 \times 10^{-8}$ dm$^2$ | Column 4, measured | Initial permeabilities |
| $\varrho_c$ | 2710 g L$^{-1}$ | – | Calcite density |
| $\varrho_f$ | 10 g L$^{-1}$ | **Fitted**[c] | Biofilm density (dry) |
| $D_w$ | $10^{-7}$ dm$^2$ s$^{-1}$ | – | Molecular diffusion |
| $\alpha_L$ | 0.25 dm | Estimated from *Frippiat et al.* [2008] | Long. dispersivity |
| $A_{sw,0}$ | 500 dm$^2$ dm$^{-3}$ | Estimated from $\phi_0$ | Specific surface areas |
| $a_c$ | 2000 dm$^2$ dm$^{-3}$ | Estimated[d] | Specific surface areas |
| $k_{prec}$ | $1.5 \times 10^{-12}$ mol/(dm$^2$ s) | *Zhong and Mucci* [1989] | Precip. parameters in equation (5) |
| $n_p$ | 3.27 | *Zhong and Mucci* [1989] | Precip. parameters in equation (5) |
| $k_{diss,1}$ | $8.9 \times 10^{-3}$ Kg$_{H_2O}$/(dm$^2$s) | *Chou et al.* [1989] | Dissolution parameters in equation (7) |
| $k_{diss,2}$ | $6.5 \times 10^{-9}$ mol/(dm$^2$ s) | *Chou et al.* [1989] | Dissolution parameters in equation (7) |
| $n_d$ | 1 | *Flukiger and Bernard* [2009] | Dissolution parameters in equation (7) |
| $k_\mu$ | $2.89 \times 10^{-5}$ s$^{-1}$<br>(2.5d$^{-1}$) | **Fitted**[e] | Substrate utilization |
| $K_s$ | $7.99 \times 10^{-4}$ g L$^{-1}$ | *Taylor and Jaffě* [1990] | Half-saturation constants |
| $K_e$ | $2 \times 10^{-5}$ g L$^{-1}$ | *Hao et al.* [1983] | Half-saturation constants |
| $Y$ | 0.5 | *Seto and Alexander* [1985] | yield coefficient |
| $F$ | 0.5 | *Mateles* [1971] | $O_2$ consumption |
| $b_0$ | $3.18 \times 10^{-7}$ s$^{-1}$<br>(0.0275 d$^{-1}$) | *Taylor and Jaffě* [1990] | Decay coefficient |
| $K_{pH}$ | $6.15 \times 10^{-10}$ (mol/kg$_{H_2O}$)$^2$ | *Kim and Fogler* [2000] | Decay parameter in equation (25) |
| $c_{a,1}$ | 0.0443 s$^{-1}$<br>(3831 d$^{-1}$) | **Fitted**[f] | Attachment parameters<br>Attachment parameters |
| $c_{a,2}$ | $9.19 \times 10^{-4}$ s$^{-1}$<br>(79.38 d$^{-1}$) | **Fitted**[f] | Attachment parameters |
| $c_{d,1}$ | $2.89 \times 10^{-8}$ s$^{-1}$<br>$2.5 \times 10^{-3}$ d$^{-1}$ | *Ebigbo et al.* [2010] | Detachment parameter |
| $k$ | 0.0417 mol/(g s)<br>(2500$\mu$ mol/(mg min)) | *Krajewska* [2009] | Rate of ureolysis |
| $K_u$ | 0.0173 mol/kg$_{H_2O}$ | *Krajewska* [2009] | Parameters in equation (1) for calculation of ureolysis rate |
| $K_{EU,1}$ | $7.57 \times 10^{-7}$ mol/kg$_{H_2O}$ | *Fidaleo and Lavecchia* [2003] | Parameters in equation (1) for calculation of ureolysis rate |
| $K_{EU,2}$ | $1.27 \times 10^{-8}$ mol/kg$_{H_2O}$ | *Fidaleo and Lavecchia* [2003] | Parameters in equation (1) for calculation of ureolysis rate |
| $K_{NH_4^+}$ | 0.0122 mol/kg$_{H_2O}$ | *Fidaleo and Lavecchia* [2003] | Parameters in equation (1) for calculation of ureolysis rate |
| $k_{ub}$ | 0.11 | **Fitted** | Parameters in equation (3) |
| $n_{ub}$ | 1.5 | **Fitted** | Parameters in equation (3) |
| $T$ | 25°C | Constant | Temperature |

[a] Fitting is done using columns 1 and 2. Fitted parameters are highlighted in bold. Table references include: [57, 111, 124, 125, 135, 140, 150-155]. [b] The relatively large values of $\varphi_c$ (0.3) at the influent of column 1 suggest that $\varphi_{crit}$ is lower than the range of porosities achieved in these experiments. [c] Literature values for $\rho_f$ include (in g L$^{-1}$) 14–91 [156], 2.5 and 3 [140], 29.3 and 38.4 [157], and 34–76 [158]. [d] Estimated as $a_c \approx \frac{3}{r}$ (assuming the ‘‘effective’’ radius of a calcite crystal r =150 μm). The results of these simulations were not sensitive to $a_c$. [e] Literature values for $k_\mu$ vary with bacterial strain and environmental conditions, e.g., 2.6 - 6.5 d$^{-1}$ ([151]) and 7.7d$^{-1}$ ([140]). [f] These values are lower but not very different from those of Taylor and Jaffe [1990] where $c_{a,1}$ = 6810 d$^{-1}$ and $c_{a,2}$ = 635 d$^{-1}$.

Figure 3.6 shows the results of the simulation for the columns used for model calibration. The calibrated model predicted $\varphi_c$ for columns 3 and 4 (Figure 3.8) with little error: the root-mean-square errors were 0.0046 and 0.0032, respectively. However, in column 3 (Figure 3.7), the results differ slightly from the experimental data toward the effluent. These differences, particularly toward the effluent, could be the result of an artifact in the experiments of calcium carbonate precipitating in the nonporous-medium-containing effluent section and settling onto and possibly into the effluent section. Additionally, increased bacterial (and thus ureolytic) activity could be due to diffusion of oxygen through the silicon tubing in the effluent leading to increased microbial concentrations, and thus precipitation.

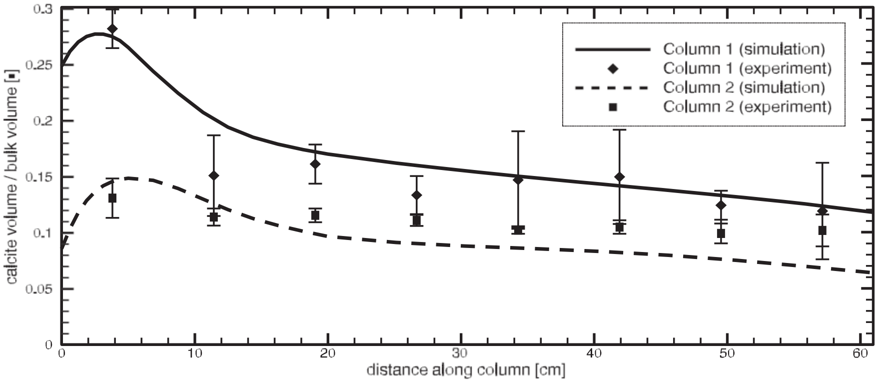

Figure 3.6. Calcite volume per bulk volume $\varphi_C$. Columns 1 (at t=58 d) and 2 (at t=35 d) were used for the calibration of the model as shown in Table 3.3. Six model parameters were fitted here. The symbols show experimental data with standard deviations, and lines are simulation results. In the simulations, calcite precipitation is lower directly at the inlet as a result of the high ionic strength caused by the injection of $Ca^{2+}$ which reduces the activity of $CO_3^{2-}$ as shown in Figure 3.2.

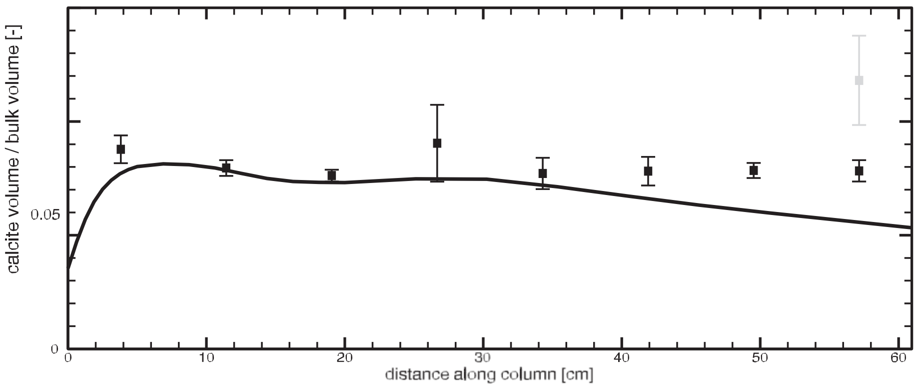

Figure 3.7. Calcite volume per bulk volume $\varphi_c$ for column 3 at t=17 d. Results of predictive modeling of the column 3 experiment using the calibrated set of parameters from columns 1 and 2. Symbols show experimental data, and lines are simulation results. Model predictions are in good agreement with experimental results except toward the outlet of the column. It is worth noting that in the first evaluation of this experiment, the amount of calcite estimated in the last column section was significantly higher (gray symbol). This was attributed to an inclusion of calcite precipitates from the effluent tubing in the calculation of $\varphi_c$. The amount of calcite in this section was subsequently reevaluated separately, and the resulting value is shown in black.

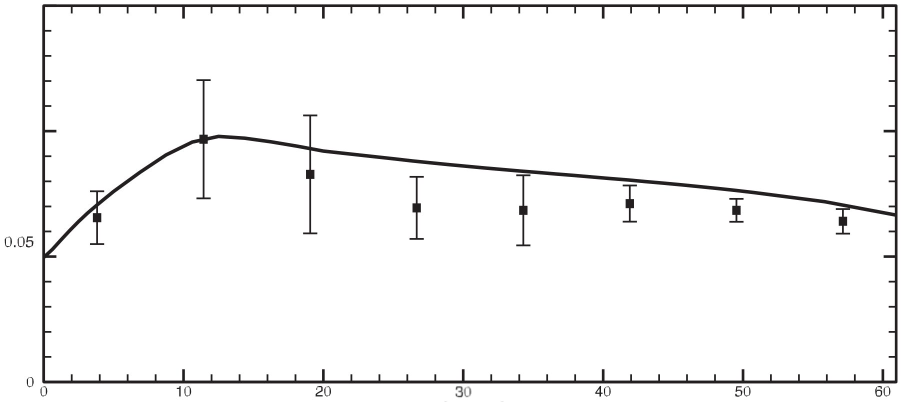

Figure 3.8. Calcite volume per bulk volume $\varphi_c$ for column 4 at t=34 d. Results of predictive modeling of column 4 experiment using the calibrated set of parameters from columns 1 and 2. Symbols show experimental data, and lines are simulation results. Model predictions are in good agreement with the experiment.

In addition to the calcite distribution along the column, the modeling results are compared to the pH of the effluent samples taken during the experiments. The samples were taken after mineralization phases, 7 min after flow was restarted. While the pH data was not used in the model calibration, good correlation between the model and experimental results were achieved (Figure 3.9). However, the experiments generally show a stronger variation of pH than the model. This may indicate an overestimation of the buffering capacity of the carbonate mineral by the model, i.e., an overestimation of the rates of precipitation and dissolution. Data for precipitation and dissolution rates were taken from studies without the interference of microorganisms capable of forming biofilms. It is possible that the presence of the biofilm reduces these rates. This may also be a source of error for the model prediction of the amount of $Ca^{2+}$ precipitates, particularly toward the effluent of the columns.

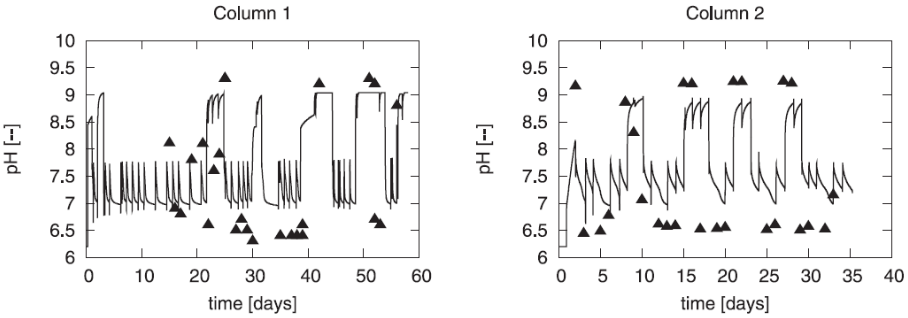

Figure 3.9. Comparison of effluent pH over time resulting from the experimental procedure for two experiments. Continuous lines are model predictions, while the symbols are the measurements.

The effect of the injection strategy used for columns 2–4 on the saturation state Ω of calcite and hence on calcite precipitation within the column is illustrated in Figure 3.10.

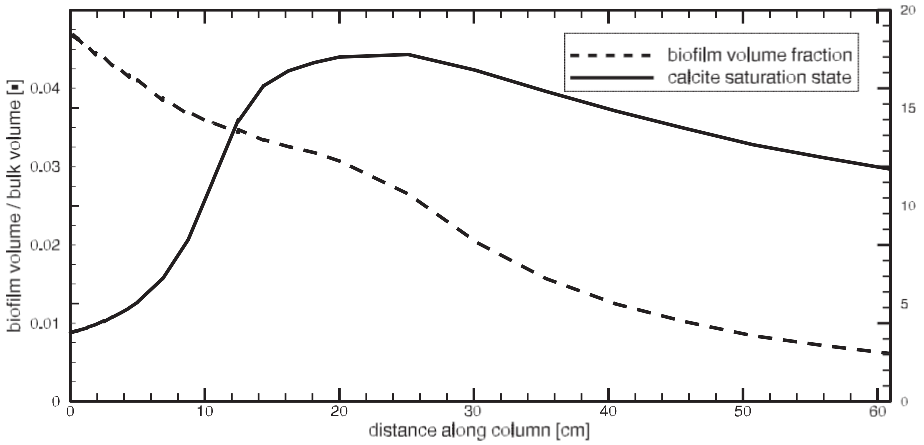

Figure 3.10. Results of simulation for column 4 showing the calcite saturation state Ω and biofilm volume fraction along the column length (at t = 33 d) during the final biomineralization phase.

It can be seen that the injection of a small amount of calcium-free medium into the column just before the biomineralization phase leads to a reduction of Ω next to the injection point. The figure also shows that the biomass does not distribute uniformly within the column, but accumulates mostly at the inlet due to the availability of oxygen at the inlet.

## Sensitivity Study

In order to gain some insight into the importance of the uncertain parameters fitted in section 4, a sensitivity study was conducted. All six parameters ($\rho_f$ , $k_\mu$, $c_{a,1}$, $c_{a,2}$,

$k_{ub}$, and $n_{ub}$) were varied within a given range to determine their effects on the error as compared to the experimental measurements. It must be noted, however, that the parameters are varied individually. A detailed investigation of parameter correlations is beyond the scope of this study, although it might give further valuable insight. Nonetheless, the main sources of uncertainty for the model with respect to parameterization can be shown with this study.

For each parameter, a lower and an upper limit were defined. For the substrate utilization rate $k_\mu$ and the biofilm density $\rho_f$, these can be determined from literature (see the footnotes in Table 3.3). However, for the other parameters, the lower and upper limits are more difficult to determine. As such, they were approximated by the variation of the fitted values given in Table 3.3 by approximately an order of magnitude in both directions (see Table 3.4). Intermediate parameter values, defined as either half or double the fitted value, are referred to as low and high values, respectively (Table 3.4). Intermediate-value simulations were carried out only for the parameters to which the system is most sensitive, as shown in Table 4.

Table 3.4 Variation of Parameters for Sensitivity Study

| | $\varrho_f[\mathrm{g\ L^{-1}}]$ | $k_\mu[1\ \mathrm{d}^{-1}]$ | $c_{a,1}[1\ \mathrm{d}^{-1}]$ | $c_{a,2}[1\ \mathrm{d}^{-1}]$ | $k_{ub}$ | $n_{ub}$ |
|---|---|---|---|---|---|---|
| Upper limit | 50 | 4 | 40,000 | 800 | 1 | 2.5 |
| Lower limit | 5 | 1 | 400 | 8 | 0.01 | 0.5 |
| High value | – | – | 7662 | 158.76 | 0.22 | 2 |
| Low value | – | – | – | – | 0.055 | 1 |
| Original value | 10 | 2.5 | 3831 | 79.38 | 0.11 | 1.5 |

The results of the sensitivity study as shown in Figure 3.11 clearly demonstrate that for this setup, the model is most sensitive to the proportionality factor $k_{ub}$. A quantification of this parameter experimentally would significantly reduce the model uncertainty.

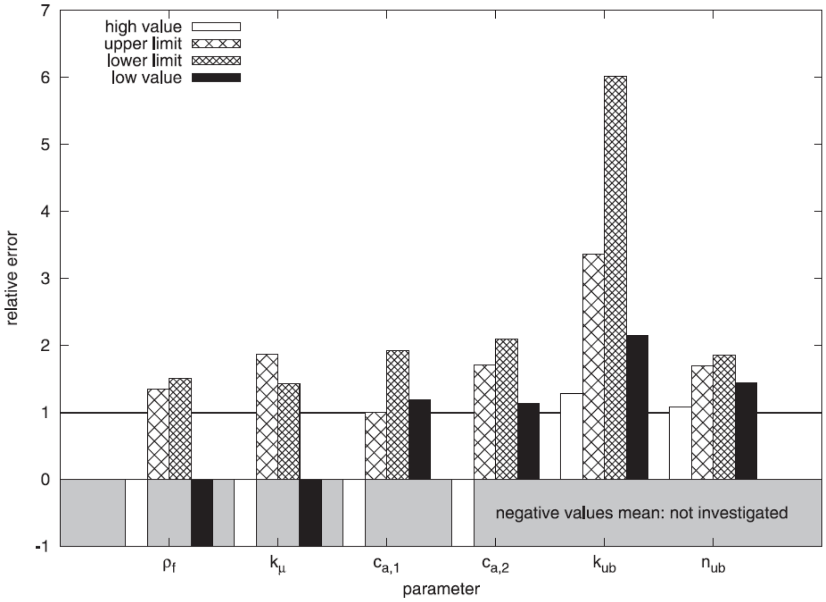

Figure 3.11. The effect of six parameters on the error made by the numerical model as compared to the experimental data on calcite distribution. The histogram shows error (i.e., total sum of the squared errors for both columns) relative to the error with the calibrated parameters.

## Simulations with Two Fluid Phases

The effect of dense-phase $CO_2$ on the mineral barrier is the focus of current research by the authors. The numerical model is a useful tool with which several processes can be investigated and new experiments can be designed. As an example, in this section, possible effects of free-phase $CO_2$ on carbonate precipitates are investigated with the help of the numerical model.

A simple simulation is shown here in which $CO_2$ is injected into a column in which a given amount of calcite ($\varphi_c = 0.1$) and biofilm ($\varphi_f = 0.05$) are initially present and uniformly distributed. The other initial and boundary conditions are identical to those of the experiments with saturated flow except pressure which is assumed to be 80 bar.

Two injection scenarios were tested. In both cases, the total injection rate and other parameters were the same as in the column 4 experiment (i.e., 0.155 mL $s^{-1}$), and a constant mass fraction of water in $CO_2$ of 1.5 x $10^{-4}$ g $g^{-1}$ is assumed (corresponding to the saturation pressure of water in the $CO_2$ phase at 25°C and 80 bar): injection of pure $CO_2$ and injection of 90% (by volume) $CO_2$ (i.e., 0.1395 mL $s^{-1}$) and 10% water (i.e., 0.0155 mL $s^{-1}$).

These result in two fluid phases within the column. A simulation time of 3 d is chosen. Two-phase-flow parameters used here include residual water and $CO_2$ saturations $S_{wr}$ =0.1 and $S_{nr}$ =0.05, pore size-distribution index $\lambda$= 2, entry pressure $p_d$ =0.1 bar. The molecular diffusion coefficient for the $CO_2$ phase is approximated with $D_{CO2} = 10^{-3}$ $dm^2$ $s^{-1}$.

As can be seen in Figure 3.12, the simulations show that:

1. The injection of pure, dense-phase $CO_2$ leads to limited calcite dissolution within the column because the dissolution of $CaCO_3$ buffers the pH of the medium, minimizing further dissolution.
2. The injection of both $CO_2$ and water leads to relatively fast dissolution. The injected water flushes out resident water reducing the buffering capacity of the calcite.

As such, limited success of this technology may be seen with $CO_2$ injection strategies involving large volumes of simultaneously injected water.

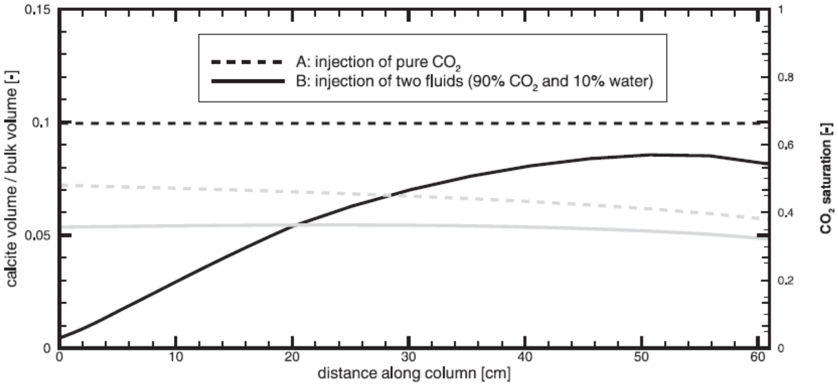

Figure 3.12. Results of simulations (at t =3 d) showing the effect of pure $CO_2$ and a $CO_2$-water mixture on calcite within the sand column. The black lines show the calcite distribution, while the gray lines show the saturation of $CO_2$.

## Conclusions

1. Relatively uniform microbially mediated precipitation could be achieved in three of the four experiments involving water-saturated flow through 61 cm, sand-packed columns when near-injection-point calcium-medium displacement strategies were used.
2. Calcium deposition efficiency may be optimized by balancing biomineralizing periods with bacterial resuscitation events. Long biomineralization periods could lead to inactivation of bacterial cells (due to cell encapsulation), reduced ureolysis, and, ultimately, reduced calcium deposition efficiency.
3. A numerical model has been developed, capable of describing microbially induced carbonate precipitation and dissolution in porous media in the presence of water and $CO_2$ flow.

4. Part of the numerical model, i.e., for water-saturated flow through sterilized sand, was validated with experimental data for one-dimensional column experiments.

It should be noted that a transfer of the model to field scenarios might not be straightforward while focusing on model scale-up is currently ongoing [6].

## Outlook

1. The model can and will be used to optimize injection strategies to achieve a large radius of influence in larger-scale, three-dimensional experiments.
2. High-pressure, dense-phase-$CO_2$ experiments will be designed using the model as a predictive tool.
3. In the future, the two-phase-flow model will be validated with the results of high-pressure laboratory experiments.
4. The model would also be suitable, with slight modifications, for other applications involving microbially induced $CaCO_3$ precipitation including (but not limited to) strontium co-precipitation as well as soil and dike stabilization.

## Chapter Specific Supporting Information

### Notation (Subscripts)

| | |
|---|---|
| $\alpha_L$, $\alpha_T$ | Longitudinal and transverse dispersivities [dm] |
| $\varphi$ | Porosity |
| $\varphi_0$ | Initial porosity |
| $\varphi_c$ | Volume fraction of calcite $[l_{calcite}=l_{bulk}]$ |
| $\varphi_{crit}$ | Critical porosity at which $K = 0$ |
| $\varphi_f$ | Volume fraction of biofilm $[l_{biofilm}=l_{bulk}]$ |
| $\gamma$ | Activity coefficient |
| $\mu$ | Biomass growth coefficient $[1\ s^{-1}]$ or $[1\ d^{-1}]$ |

| | |
|---|---|
| $\mu_\alpha$ | Dynamic fluid-phase viscosity [Pa·s] or [g/(dm·s)] |
| $\lambda$ | Pore size-distribution index |
| $\mu_{max}$ | Maximum specific rate of urea hydrolysis [mol$_{urea}$=g$_{urease}$·s] |
| $\Omega$ | Calcite saturation state |
| $\rho$ | Density [kg m$^{-3}$] or [g L$^{-1}$] |
| $\tau$ | Tortuosity |
| $a_c$ | Specific surface area of calcite grains [dm$_2$ L$^{-1}$] |
| $b$ | Decay coefficient [L s$^{-1}$] or [L d$^{-1}$] |
| $b_0$ | Endogenous decay coefficient [L s$^{-1}$] or [L d$^{-1}$] |
| $c_{a,i}$ | Parameters for the calculation of $k_a$ |
| $c_{d,i}$ | Parameters for the calculation of $k_d$ |
| $g$ | Gravitation vector [ms $^{-1}$] |
| $k$ | Specific rate of urea hydrolysis [mol$_{urea}$=g$_{urease}$·s] |
| $k\mu$ | Maximum substrate utilization rate [L s$^{-1}$] or [L d$^{-1}$] |
| $k_a$ | Attachment coefficient [L s$^{-1}$] or [L d$^{-1}$] |
| $k_d$ | Detachment coefficient [L s$^{-1}$] or [L d$^{-1}$] |
| $k_{diss;1}$ | Parameter for calculation of $r_{diss}$ [kg$_{H2O}$ = dm$^2$ · s] |
| $k_{diss;2}$ | Parameter for calculation of $r_{diss}$ [mol= dm$^2$ · s] |
| $k_{prec}$ | Parameter for calculation of $r_{prec}$ mol=dm$^2$ s] |
| $k_r$ | Relative permeability |
| $k_{ub}$ | Parameter for the calculation of $Z_{ub}$ |
| $m$ | Molality [mol=kg$_{H2O}$] |
| $n_d$ | Parameter for calculation of $r_{diss}$ |
| $n_p$ | Parameter for calculation of $r_{prec}$ |
| $n_{ub}$ | Parameter for the calculation of $Z_{ub}$ |
| $p$ | Phase pressure [Pa] or [bar] |
| $p_{cap}$ | Capillary pressure [Pa] or [bar] |
| $p_d$ | Entry pressure [Pa] or [bar] |
| $q$ | Source/sink [g=L·s] |
| $r_a$ | Biomass attachment rate [g/(L· s)] |
| $r_b$ | Biomass decay rate [g/(L·s)] |
| $r_d$ | Biomass detachment rate [g/(L·s)] |
| $r_{diss}$ | Net rate of calcite dissolution [mol/(L·s)] |
| $r_g$ | Biomass growth rate [g/(L s)] |
| $r_{prec}$ | Net rate of calcite precipitation [mol/(L·s)] |
| $r_{urea}$ | Rate of urea hydrolysis [mol$_{urea}$/(L· s)] |
| $v$ | Darcy flux/velocity [dm s$^{-1}$] |
| $z$ | Ionic charge |
| $A_{cw}$ | Specific surface area between water and calcite [dm$^2$ L$^{-1}$] |
| $A_{sw}$ | Specific surface area between water and solids (i.e., both porous matrix and calcite) [dm$^2$ L$^{-1}$] |
| $A_{sw,0}$ | Initial value of $A_{sw}$ [dm$^2$ L$^{-1}$] |
| $C$ | Concentration [g L$^{-1}$] |
| $D$ | Hydrodynamic dispersion [dm$^2$ s$^{-1}$] |
| $D$ | Molecular diffusion coefficient [dm$^2$ s$^{-1}$] |
| $F$ | Oxygen consumption per unit mass of substrate |

| | |
|---|---|
| $K$ | Permeability [$dm^2$] |
| $K^*_1$ | Apparent dissociation coefficient of $H_2CO_3$ |
| $K^*_2$ | Apparent dissociation coefficient of $HCO_3^-$ |
| $K^*_a$ | Apparent dissociation coefficient of $NH_4^+$ |
| $K_{EU,i}$ | Dissociation constants for enzyme-urea complex [$mol=kg_{H2O}$] |
| $K_{NH4+}$ | Parameter for inhibition due to $NH_4^+$ [$mol=kg_{H2O}$] |
| $K_{pH}$ | Constant for calculation of pH-dependent decay [$mol=kg_{H2O}$] |
| $K_s$, $K_e$ | Monod half-saturation constant [$g\ L^{-1}$] |
| $K_u$ | Ureolysis half-saturation constant [$mol=kg_{H2O}$] |
| $K_{sp}$ | Calcite solubility product [$mol=kg_{H2O}$] |
| $K_w$ | Apparent dissociation coefficient of water [$mol=kg_{H2O}$] |
| $M$ | Molecular mass [$g\ mol^{-1}$] |
| $S$ | Saturation |
| $S_r$ | Residual saturation |
| $T$ | Temperature [C] |
| $X$ | Mass fraction |
| $Y$ | Yield coefficient |
| $Z_{ub}$ | Concentration of urease in porous medium [$g\ L^{-1}$] |

Subscripts

| | |
|---|---|
| c | Calcite |
| f | Attached biomass/biofilm |
| n | Nonwetting phase |
| w | Wetting phase |

Superscripts

| | |
|---|---|
| a | Ammonia/ammonium |
| b | Suspended biomass |
| c | Calcite |
| $Ca^{2+}$ | Calcium |
| $Cl^-$ | Chloride |
| $CO_2$ | Carbon dioxide |
| e | Electron acceptor/oxygen |
| f | Biofilm |
| $Na^+$ | Sodium |
| s | Growth substrate |
| u | Urea |
| w | Water |

## Image and EDX Analysis of Minerals

Figure 3.13 depicts the surface of sand from a treated column where calcium carbonate crystals were observed in the size range of 10 to 100 µm. Spot EDX analysis of the crystals confirmed the presence of elemental calcium (data not shown). In addition, EDX elemental mapping revealed calcium in regions where obvious crystals had formed and silica in the region of the base materials (see Figure 3.13). This result leads to additional support that the formed minerals were calcium carbonate.

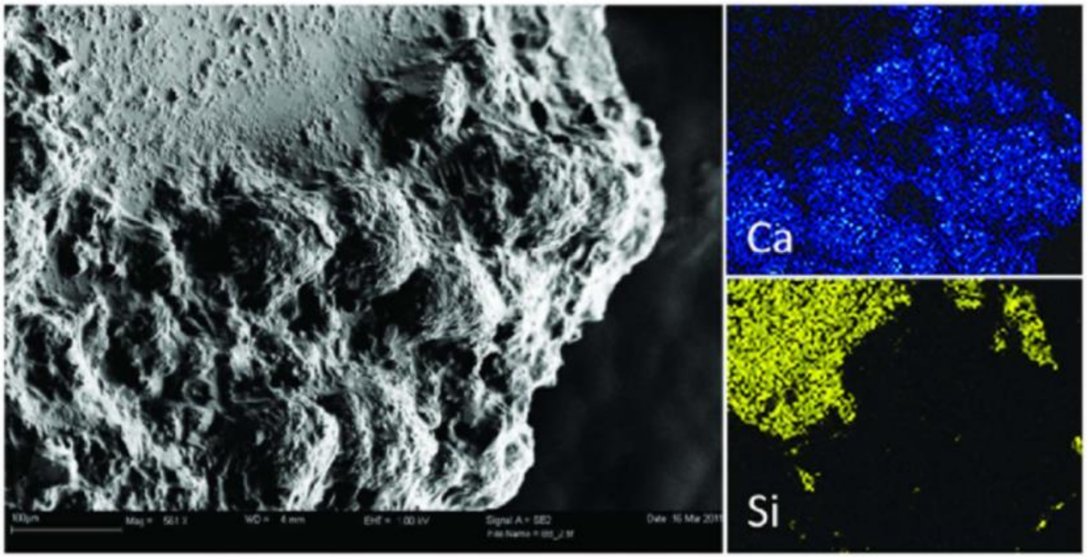

Figure 3.13. Scanning electron micrograph of $CaCO_3$-crystal structure on sand particle along with EDX elemental maps for calcium and silicon (scale bar: 100 µm).

# CHAPTER FOUR

# POTENTIAL $CO_2$ LEAKAGE REDUCTION THROUGH BIOFILM-INDUCED CALCIUM CARBONATE PRECIPITATION

## Contribution of Authors and Co-Authors

Manuscript in Chapter 4

Author: Adrienne J. Phillips

Contributions: Designed and performed experimental work, analyzed data. Wrote and revised manuscript.

Co-Author: Ellen Lauchnor

Contributions: Contributed to experimental design and to the revision of the manuscript with comments and feedback.

Co-Author: Joachim Eldring

Contributions: Contributed to experimental design and to the revision of the manuscript with comments and feedback.

Co-Author: Richard Esposito

Contributions: Contributed to the experimental design, procured core, performed thin section analysis and contributed to revision of the manuscript with comments and feedback.

Co-Author: Andrew Mitchell
Contributions: Contributed to the revision of the manuscript with comments and feedback.

Co-Author: Robin Gerlach

Contributions: Contributed to experimental design and to the revision of the manuscript with comments and feedback.

Co-Author: Alfred Cunningham

## Contribution of Authors and Co-Authors Continued

Contributions: Contributed to experimental design and to the revision of the manuscript with comments and feedback.

Co-Author: Lee Spangler
Contributions: Contributed to the revision of the manuscript with comments.

# Manuscript Information Page

Phillips, A.J., Lauchnor, E., Eldring, J., Esposito, R., Mitchell, A.C., Gerlach, R., Cunningham, A., Spangler, L.
Environmental Science and Technology
Status of Manuscript:
____ Prepared for submission to a peer-reviewed journal
____ Officially submitted to a peer-review journal
____ Accepted by a peer-reviewed journal
_X__ Published in a peer-reviewed journal

American Chemical Society
47 (1), pp. 142–149, January 2013

## Abstract

Mitigation strategies for sealing high permeability regions in cap rocks, such as fractures or improperly abandoned wells, are important considerations in the long term security of geologically stored carbon dioxide ($CO_2$). Sealing technologies using low-viscosity fluids are advantageous in this context since they potentially reduce the necessary injection pressures and increase the radius of influence around injection wells. Using aqueous solutions and suspensions that can effectively promote microbially induced mineral precipitation is one such technology. Here, we describe a strategy to homogenously distribute biofilm-induced calcium carbonate ($CaCO_3$) precipitates in a 61 cm long sand-filled column and to seal a hydraulically fractured, 74 cm diameter Boyles Sandstone core. *Sporosarcina pasteurii* biofilms were established and an injection strategy developed to optimize $CaCO_3$ precipitation induced via microbial urea hydrolysis. Over the duration of the experiments, permeability decreased between 2 and 4 orders of magnitude in sand column and fractured core experiments, respectively. Additionally, after fracture sealing, the sandstone core withstood three times higher well bore pressure than during the initial fracturing event, which occurred prior to biofilm-induced $CaCO_3$ mineralization. These studies suggest biofilm-induced $CaCO_3$ precipitation technologies may potentially seal and strengthen fractures to mitigate $CO_2$ leakage potential.

## Introduction

Subsurface fractures may provide leakage pathways for geologically sequestered $CO_2$. Whether fractures are initiated intentionally by hydraulic fracturing to alter subsurface flow conditions (i.e., improving fossil fuel extraction), unintentionally during drilling or pumping fluids into reservoirs, or exist because of natural formation conditions, fractures can play a significant role in the determination of geologic reservoir permeability and fluid flow pathways [159, 160]. As such, high permeability fractures in cap rock or even microfractures associated with well cements may contribute significantly to reservoir leakage potential [104, 105].

Ideally, potential $CO_2$ storage sites are not connected to drinking or agricultural water aquifers and generally, functional aquifers are also separated from target storage reservoirs by low permeability cap rocks. Nevertheless, concerns exist regarding the impact of potential $CO_2$ migration into overlying aquifers and the atmosphere [161, 162]. Leakage could result in carbon credit forfeiture under a carbon trading system, wasted resources or energy associated with the injection of $CO_2$, pose a hazard to overlying functional water aquifers or endanger public health [105, 161, 162]. Thus, primary leakage prevention or mitigation is essential to managing risks associated with subsurface $CO_2$ storage.

Reducing the permeability of leakage pathways with biofilm has been previously investigated with promising results [28]. The advantage to the use of microorganisms is their penetrability into small apertures[163], which may not be possible with higher viscosity sealing cements, making small fractures a target for biofilm sealing. The disadvantage to biofilm sealing technologies is the maintenance of established barriers; microbial biofilms will degrade over time without nutrient supply. However, a novel strategy using ureolysis-driven biofilm-induced $CaCO_3$ precipitation to mitigate fluid or gas leakage from subsurface reservoirs has been investigated [4]. With biofilm-induced $CaCO_3$ precipitation, a stable mineral can remain even after biofilm has dispersed or nutrient addition has ceased.

Many microorganisms are capable of hydrolyzing urea enzymatically, which can influence the saturation state (S) of surrounding fluids in the presence of calcium to favor precipitation (when $S > 1$) of $CaCO_3$ (eqs 1 and 2) [39, 42, 43].

$$CO(NH_2)_2 + 2H_2O \longrightarrow 2NH_4^{+} + CO_3^{2-} \qquad (1)$$

$$Ca^{2+} + CO_3^{2-} \longleftrightarrow CaCO_3\ (s) \qquad (2)$$

Microbial or biofilm-induced $CaCO_3$ precipitation (MICP) via the urea hydrolysis pathway has been well explored for use in many technologies including: sealing cement fractures, forming protective surface layers, or strengthening cement [9]; controlling flow in permeable zones or channels [19, 89]; and consolidating porous media, among other applications [32]. These MICP technologies are widely researched across multiple disciplines, multiple scales (from micro to macro), and the understanding of treatment control and extent is rapidly advancing [18]. For example, it was previously observed that MICP can produce nonhomogeneous distribution of $CaCO_3$ which may lead to injection point plugging, limiting the spatial extent of the treatment [13, 30]. Researchers speculated more homogeneous distribution could be achieved by balancing the transport of reactants with the reaction rates or improving distribution of cells [13]. These hypotheses were acknowledged and utilized to investigate an injection strategy leading to more homogeneous $CaCO_3$ distribution in the research reported here.

The overall objective of this work was to investigate whether biofilm-induced $CaCO_3$ mineralization could be scaled from a 61 cm laboratory sand-filled column to sealing a fractured 74 cm diameter sandstone core. Specific objectives were to (a) develop a new injection strategy in a sand-filled column to minimize injection point precipitation and promote homogeneous spatial distribution of $CaCO_3$ while reducing permeability and (b) demonstrate that MICP technology is suited to sealing fractures, which could contribute to the leakage of geologically stored $CO_2$. To this end, the injection strategy developed in the column study was used to twice seal and significantly strengthen a hydraulic fracture under radial flow and ambient pressure conditions in a Boyles Sandstone core. The primary novel aspect of this work is that $CaCO_3$ distribution is controlled by manipulating the $CaCO_3$ saturation conditions in time and space. This time and space dependent control of the $CaCO_3$ saturation index can be applied to real world systems to promote homogeneous distribution of $CaCO_3$ along the direction of flow and minimize near-injection-point plugging.

## Experimental Methods

### Bacterial Cultivation

Cultures of *Sporosarcina pasteurii*, a ureolytically active organism, were grown overnight from frozen stock cultures to stationary phase, washed via centrifugation, and resuspended in fresh sterile medium to an $OD_{600}$ of 0.4 prior to column or fracture inoculation.

## Column Experiment

Results from column experiments 1–4 were previously reported in Cunningham et al. (2011) and Ebigbo et al. (2012). Similar to those experiments, column 5 was prepared by packing a 61 cm long, 2.54 cm diameter column with sand, followed by disinfection and rinsing (Supporting Information). Growth (ionic strength 0.2M) and calcium-growth (ionic strength 1.2M) media were prepared as previously described (Supporting Information) and a calcium- and urea-free (displacement) medium (ionic strength 0.2M) was prepared with 3 g/L Difco Nutrient Broth, 10 g/L ammonium chloride (Fisher, NJ, USA), and 100 mL/L glycerol (EMD Chemicals, NJ, USA) to minimize media density differences. Media densities were confirmed by comparing the masses of known volumes and media viscosities were measured using a TA Instruments AR-G2 rotational rheometer. Column 5 was inoculated and a post inoculation cell-attachment period (no flow) of approximately 6 h was followed by 18 h of biofilm promotion by continuously injecting growth medium as previously described [2, 27]. Then, the column was flushed with calcium- and urea-free medium between biomineralizing stages to establish a low saturation state and minimize instantaneous precipitation when calcium-growth medium was injected. Finally, two pore volumes of calcium-growth medium (0.33 M equimolar calcium/urea) were injected to initiate 4–8 h static biomineralization stages (Table 4.1).

The first 7.6 cm (3 in.) of the column were replaced with displacement medium immediately after injection of the calcium-growth medium to minimize injection point $CaCO_3$ precipitation. During the column 5 experiment, biofilm was resuscitated by injecting fresh growth medium without $Ca^{2+}$ every afternoon for overnight growth as opposed to the periodic, unscheduled resuscitation events reported in columns 1–4 [2, 27] .

Table 4.1 Calcium deposition efficiency and permeability reduction in five column experiments [2,27]

| Column No. | Displace calcium in influent region? | Calcium concentration in Medium (M) | Calcium Deposition Efficiency | Reduction in permeability | Column plugged? |
|---|---|---|---|---|---|
| 1 | No | 1.25 | 13% | 66% | Yes |
| 2 | Yes | 1.25 | 24% | 99% | Yes |
| 3 | Yes | 1.25 | 29% | 89% | Yes |
| 4 | Yes | 1.25 | 15% | 72% | No |
| 5 | Yes | 0.33 | 71% | 61% | No |

Injection flow rates were controlled by a Masterflex (Model 7553–70) pump and controller (Cole Parmer, IL, U.S.A.) and differential pressures were monitored with water-filled piezometers to assess changes to column permeability. At the termination of the experiment, the column was destructively sampled to determine mass of calcium associated per gram of sand along the column's axis of flow [2, 27].

### Column and Core Fracture
### Residual Effluent Analysis

Column and fracture biomineralization stage effluents were collected and monitored for ammonium ($NH_4^+$), an indication of ureolysis, and residual $Ca^{2+}$ concentration. A filtered portion of the effluent sample was analyzed with a modified Nessler assay for $NH_4^+$ production [2, 27] and ion chromatography (Metrohm, USA) to monitor dissolved $Ca^{2+}$ concentration (Supporting Information). The unfiltered remainder of the effluent sample was used to monitor pH and the number of culturable cells using a drop plate enumeration method [164].

Core Drilling and Characterization

A 74.3 cm diameter, 37.5 cm tall Boyles Sandstone (member of the Lower Pottsville Formation, a potential sequestration formation identified by Southern Company, AL, USA) core was obtained from Etowah County, Alabama (Russo Corp, AL, USA) (Figure 4.1). While some unidentified artifacts associated with surface weathering may be present with the core drilled at ground surface, the Boyles Sandstone was chosen due to its presence at relevant sequestration depths in the Pottsville formation. After drilling, a slab saw was used to cut the core to height and a 5.1 cm (2 in.) hole was drilled through the core's center.

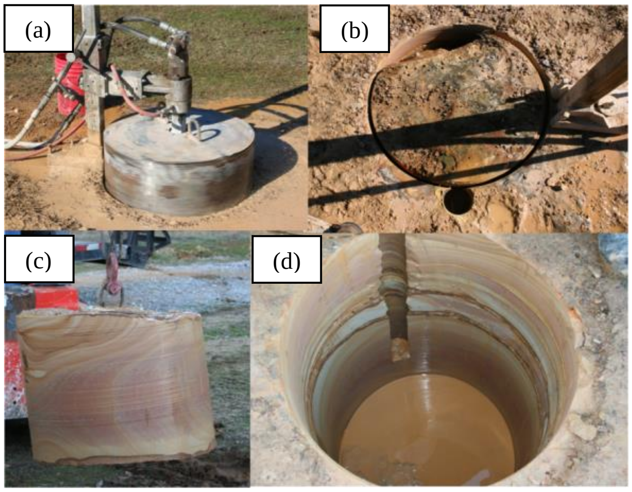

Figure 4.1. (a−d) Photos showing the progression of drilling and extraction of the Boyles Sandstone core. (a) The core was drilled using a 76.2 cm diameter core drill under water cooling to the depth of ∼100 cm; (b) a secondary 10.2 cm core was drilled adjacent to the large bore to break the core from the underlying formation with a pneumatic pump; (c) a metal plate was attached to holes drilled into the top of the core; and (d) the core was lifted free of the formation.

Samples of the cored sandstone material were sent to the University of Alabama at Birmingham, Department of Mechanical Engineering, for permeability and minimum capillary displacement pressure measurements (Supporting Information). A portion of the core material was also analyzed for porosity and pore structure characterization via mercury porosimetry (Micromeritics AutoPore IV 9500 Series, GA, USA) at University of Montana, Montana Tech's Center for Advanced Mineral and Metallurgical Processing in Butte, Montana, USA (Chapter Specific Supporting Information). Thin section analysis for mineralogy and porosity was performed at the Geological Survey of Alabama, USA (Figure S4.1, Supporting Information).

### Core Injection System Design

A Teledyne Isco pump and controller (Teledyne, NE, USA) were used to inject fluids either under constant flow or pressure control (Figure 4.2a) through flexible stainless steel tubing and stainless fittings 0.635 cm ID (1/4 in.) (Swagelok, USA). An expandable double packer assembly was constructed from a threaded rod, spacers, washers, nuts, and rubber elements (Supporting Information). The core was placed in a lined shipping crate on blocks to allow for effluent fluid collection and the packer assembly was installed to isolate a zone between 7.6 and 15.2 cm from the bottom of the core.

### Core Initial Hydraulic Fracturing Event

The core's hydraulic behavior was initially characterized by injecting water under radial flow conditions and recording flow and pressure via the Teledyne Isco pump Labview interface (National Instruments, TX, USA). Water was injected at constant pressure (8 bar) for approximately 1.75 h before the rock hydraulically fractured along a horizontal bedding plane perpendicular to the well bore (Figure 4.2b). The fracture occurred approximately 15.9 cm from the bottom of the core, measured approximately 1 mm in thickness, and extended approximately 33 cm in length on the outside circumference of the core.

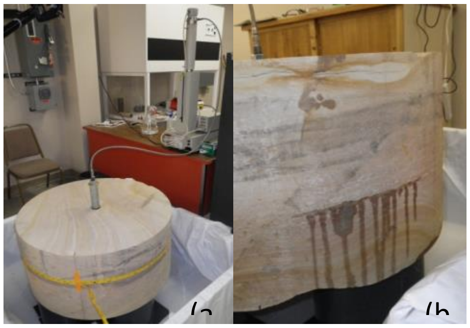

Figure 4.2. Images of injection system and flow path from the fracture. (a) Fluids were injected in radial flow configuration to the Boyles Sandstone core via double packer system with a Teledyne Isco pump. (b) Original channel-like flow path was observed from the hydraulic fracture.

## Core Fracture Sealing Experiments

For each sealing experiment, the pump, influent tubing and packer were disinfected; growth medium was injected to condition the core; and 35 mL of a *S. pasteurii* cell suspension (cell concentrations: $2.3 \times 10^7$ cfu/mL experiment #1, $3.8 \times 10^7$ cfu/mL experiment 2) was filled into the packer for fracture inoculation. Growth medium was pumped at 20 mL/min to push the cells into the fracture, and fracture effluents were collected to confirm microbial penetration (effluent concentration measured: $2.6 \times 10^5$ cfu/mL sealing experiment 1, $3.2 \times 10^6$ cfu/mL sealing experiment 2). Cell-attachment periods (no flow) of 4–5 h were followed by 18 h of continuous growth medium flow to promote biofilm development. At least two fracture pore volumes of urea- and calcium-free medium were then injected to restore low $CaCO_3$ saturation states to minimize immediate precipitation.  Next, greater than two pore volumes of 0.33 M (equimolar $Ca^{2+}$ and urea) calcium-growth medium (ionic strength 1.2M) amended with 0.04 g/L fluorescein (Acros, NJ, USA) were injected to initiate biomineralization.  Lastly, fluids in the fracture's first 5.4 cm were replaced with displacement medium to minimize injection point mineralization.

At the beginning of sealing experiment 1, after injection of the calcium-growth medium, 24 h static biomineralization stages were performed.  However, this strategy led to evaporative drying of the core overnight which was hypothesized to contribute to reduced ureolytic activity because of desiccation of the biofilm.  Hence, on day 14, growth medium was injected at 0.69 mL/min overnight to reduce drying and resuscitate ureolytic biofilm activity.  During sealing experiment 2, similar injection strategies were utilized except growth medium was injected overnight immediately to minimize evaporative drying.  During sealing experiment 2, two calcium-growth media pulses were performed daily (with 4 h biomineralization stages) in an effort to speed up sealing.

In the core sealing experiments, the pump was initially operated in constant flow mode at 20 mL/min.  However, as the fracture sealed, pressures exceeded the pump's shut off pressure set-point of 7 bar in sealing experiment 1 and 8 bar in sealing experiment 2.  These set-points were designed to minimize the risk of refracturing during sealing experiments.  Thus, for the experiments' remainder, the pump was operated in constant pressure mode in which the pump internally adjusts flow to maintain pressure rather than constant flow mode.  Influent pressure (p) and flow rate (Q) were recorded using the Isco pump's Labview interface.

Prior to injection of calcium-growth medium in sealing experiment 1, the fracture zone region on the outside circumference of the core was scraped with a disinfected stainless steel rod and particles collected as a control for XRD analysis. At the termination of the experiment, the inside of the well bore and the outside of the core in the fracture zone were also scraped and particles were analyzed by XRD to determine mineral phases present (Supporting Information Figure S4.2).

The packer was twice removed to observe well bore and packer conditions and confirm the packer was not clogged with $CaCO_3$. Well bore images were collected with a digital endoscope equipped with a reflector tube (Oasis Scientific, SC, USA) (Supporting Information Figure S4.3). The packer was cleaned, disinfected and reinserted to the original location isolating the fracture zone.

### Sealed Fracture Strength Testing

Core sealing experiment #1 was terminated by testing the strength of the sealed fracture by injecting water amended with fluorescein using stepwise increasing pressures (8 bar up to 30 bar). Two parameters were measured: injection pressure (p) and flow (Q) using the Isco pump's Labview interface. Images were collected under black light to visualize breakthrough of the injected fluid (Supporting Information Figure S4.5).

## Results

### Injection Strategy to Produce Homogenous $CaCO_3$ Distribution

Column $CaCO_3$ Distribution. Aside from the near-injection-point region of the previously reported sand-filled columns, a relatively homogeneous distribution of $CaCO_3$ was achieved along the axis of flow (Figure 4.3) [2, 27]. The first iteration of column experiments (column 1) did not employ near-injection-point calcium displacement and the $CaCO_3$ concentration per gram of sand was significantly higher near the injection point than in subsequent column experiments[2, 27]. Beyond the first 7 cm, relatively homogeneous distribution along the flow path was achieved, particularly in column 5 (Figure 4.3). Column 5's injection strategy included the use of equimolar ratios of urea and $Ca^{2+}$ in the media, near-injection-point rinsing during biomineralization stages, and regularly scheduled resuscitation events. This evolved strategy served to produce a low influent region $CaCO_3$ concentration to minimize near-injection point plugging and homogeneous distribution of $CaCO_3$ over the rest of the column. While the contribution of bacteria to the reduction in pore space was not quantified, at the end of the Column 5 experiment calcite was calculated to occupy an average of 15.4% of the 47% porosity of the sand pack.

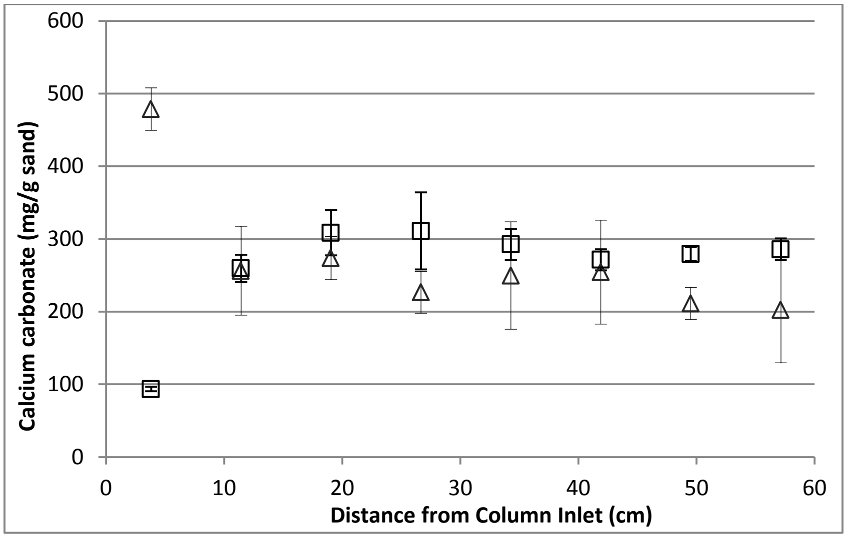

Figure 4.3. $CaCO_3$ concentration (mg) per gram of sand with error bars representing the standard deviation of measured calcium by ICP-MS in vertically positioned column experiments (Δ Column #1; □ Column #5). Reduced $CaCO_3$ in the near-injection-point (93 ± 3 mg/g sand) was measured in column #5 (near-injection-point displacement strategy employed) as compared to column #1 (478 ± 29 mg $CaCO_3$/g sand). Adapted from Ebigbo (2012) and Cunningham (2011).

Core Fracture $CaCO_3$ Distribution. Radial distribution of precipitates in the core fracture experiments could not be quantitatively determined without destructive core sampling (undesirable since further experiments are planned). Despite this limitation, visual observation of the well bore revealed apparent $CaCO_3$ precipitation, as compared to regions without treatment (Supporting Information Figure S3a and b). Additionally, calcite was detected via XRD from the scraping of the fracture region on the core's exterior (Supporting Information Figure S4.2b) and from scrapings of the well bore post experiment (data not shown). While it could not be quantitatively demonstrated that $CaCO_3$ formed homogeneously along the length of the fracture, qualitative evidence (visual observation and the positive calcite detection with XRD) suggests that $CaCO_3$

precipitated at least inside the well bore and outside the fracture (i.e. at the beginning and end of the flow path).

## Residual-Effluent Analysis

Column Ureolysis. As previously reported, column experiments 1–4 did not employ regular biofilm resuscitation events but rather resuscitation was initiated when effluent $NH_4^+$ concentrations were observed to decrease to as low as 5.1 g/L[2, 27]. In the column 5 experiment, resuscitation events were performed nightly which contributed to maintaining an active ureolytic population and high effluent $NH_4^+$ concentrations. Effluent $NH_4^+$ concentrations averaged 13.3 ± 3.3 g/L.

Core Fracture Ureolysis. On the basis of low average effluent $NH_4^+$ concentrations (4.6 ± 2.4 g/L) in core sealing experiment 1's first 13 days of treatment, it was hypothesized that evaporative drying between biomineralizing injections was negatively impacting the *S. pasteurii* biofilm, reducing the ureolytic activity, and thereby reducing $Ca^{2+}$ precipitating activity [82]. As such, on the 14th day of sealing experiment #1, the injection strategy was modified to include an overnight growth pulse to minimize desiccation and revive biofilm ureolytic activity. After day 14, it was consistently observed that the average $NH_4^+$ concentration (12.8 ± 1.2 g/L) and effluent culturable cell numbers were greater after initiating overnight biofilm resuscitation events (Figure S4 Supporting Information).

Column Calcium. The columns' $Ca^{2+}$ deposition efficiency was calculated as the sum of the mass of $Ca^{2+}$ measured in each column section determined from inductively coupled plasma mass spectrometry (ICP-MS) divided by the total known mass of $Ca^{2+}$ injected. Columns 1–4 utilized biomineralizing media with 1.25 M calcium and 0.33 M urea where $Ca^{2+}$ deposition efficiency was limited by the production of $CO_3^{2-}$ from ureolysis and complete $Ca^{2+}$ precipitation could not be achieved [2, 27]. The injection strategy employed for column 5 involved using equimolar concentrations of urea and $Ca^{2+}$ (0.33M) in the biomineralizing solutions and regularly resuscitating the biofilm with growth medium. This, as predicted, yielded greater overall $Ca^{2+}$ precipitation efficiency (Table 4.1).

Core Fracture Calcium. For the core fracture sealing experiments, evolved injection strategies using media with equimolar concentrations of $Ca^{2+}$ and urea (0.33 M) and regularly scheduled resuscitation events were utilized (beyond day 14 in experiment 1). Calcium deposition efficiency was calculated by comparing the differences between known injected $Ca^{2+}$ mass and the residual-effluent $Ca^{2+}$. In sealing experiment 1 as much as 93% and in sealing experiment 2 as much as 86% of the injected $Ca^{2+}$ was estimated to have been deposited.

### Permeability

Column Permeability. Column flow rate and differential pressure were recorded to calculate hydraulic conductivity (eq. 3) which was converted to permeability using measured fluid density and viscosity (eq. 4) [165]. K is hydraulic conductivity, Q is measured flow rate, Δp is differential pressure, A is cross-sectional column area (5.1 $cm^2$), L is column length (61 cm), k is permeability, μ is dynamic viscosity ($1.29 \times 10^{-3}$, $1.01 \times 10^{-3}$, $1.05 \times 10^{-3}$ kg/m-s displacement medium, growth medium, calcium growth medium, respectively), ρ is density (1013 $kg/m^3$), and g is the acceleration of gravity (9.81 $m/s^2$).

$$Q = -KA\frac{\Delta p}{L} \qquad (3)$$

$$k = \frac{K\mu}{\rho g} \qquad (4)$$

The permeability of the columns was reduced by 61–99% (Table 4.1) as compared to 0% in previously studied control columns either not inoculated with microbes or inoculated with a non-ureolytic strain of *Bacillus subtilis* [2, 166]. Variations in these values were attributed to not all columns being plugged or not reaching system pressure limits when destructive sampling occurred. Please note: the prescribed goal of these experiments was development of methods to produce homogeneous distribution of $CaCO_3$ along the flow length of the columns, not to plug the columns or determine the maximum reduction in permeability achievable.

Core Fracture Permeability. Fracture hydraulic conductivity was calculated using an equation for radial Darcy flow in confined aquifers[165]. To calculate conductivity of the fracture when flow was preferential through the fracture, the equation was modified to scale from full radial flow to fracture only radial flow by multiplying the 2π term with the fracture length to core circumference ratio (eq. 5), where $b_1$ is approximate fracture aperture, $b_2$ is effective width of screened area in the packer, $r_o$ is the radial extent of the fracture at the outside of the core, and $r_w$ is the radius of the well. After day 23 (sealing experiment 1) and day 5 (sealing experiment 2), conductivity was calculated with the equation restored to its original form as fluids stopped flowing through the fracture preferentially and radial flow was observed (eq. 6).

$$K = Q\frac{\ln\left(\frac{r_0}{r_w}\right)}{\left(\frac{fracture\ length}{core\ circumference}\right)2\pi\,\Delta p\, b_1} \qquad (5)$$

$$K = Q\frac{\ln\left(\frac{r_0}{r_w}\right)}{2\pi\,\Delta p\, b_2} \qquad (6)$$

We assume (1) constant fracture aperture, (2) wellbore flow into the matrix is negligible compared with the fracture flow (until full radial flow is restored), (3) the ratio of the fracture's inner circumference to inner well bore circumference is the same as the outer fracture circumference to total core circumference, (4) fracture flow is horizontal and any vertical fracture flow is negligible, and (5) fracture roughness is neglected [167]. The calculated conductivity was converted to permeability using measured fluid viscosity and density parameters via eq. 4 (Figure 4.4).

After sealing experiment 1, the sealed fracture strength was assessed with a second hydraulic fracture event. Pressures applied to the well bore were increased stepwise (8–30 bar) over the course of 1.6 h until fluids were observed flowing from the fracture. The flow rate of water increased from 1.5 to 160 mL/min as the differential pressure increased from 8 to 30 bar. In addition to the visual observation of water beginning to flow rapidly from the fracture at 30 bar, the flow rate jumped quickly from 8.8 mL/min at 28 bar to 160 mL/min at 30 bar when the apparent refracturing event occurred. Calculation methodologies outlined in eqs 5 and 6 were used to estimate the permeability. Before reaching 30 bar, when fluids were not observed flowing from the fracture, the permeability was calculated using eq 6; at 30 bar with fracture dominated flow, permeability increased and was calculated with eq 5 (Figure 4.5). Since the packer was likely leaking at 30 bar, the pressure was decreased to 8 bar (not beyond packer's pressure limit) to confirm the refracturing permeability of 2,100 md.

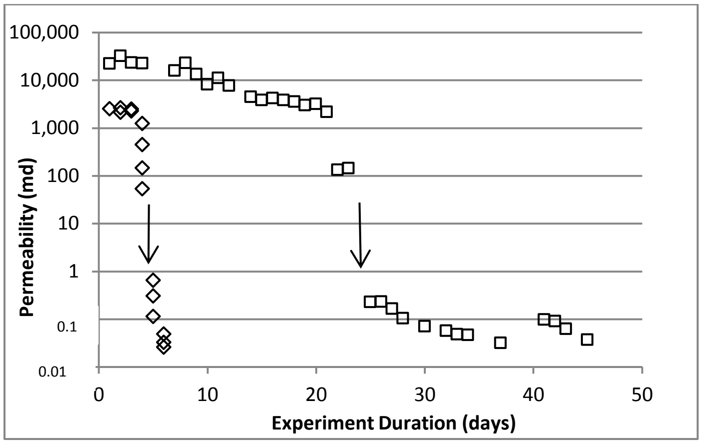

Figure 4.4: Calculated reduction in permeability from fracture sealing experiment #1(□) and #2 (◊). Arrows indicate when radial rather than fracture dominated flow was observed and also where the transition was made to calculate permeability using Equation 6 (full radial flow) as opposed to Equation 5 (fracture dominated flow). At day 23 and day 5 (for sealing experiment #1 and sealing experiment #2, respectively) no fluid flow was observed from the fracture and the injected fluids extended radially from the well. Calculated permeability reduced from approximately 23,000 md to approximately 0.1 md in sealing experiment #1 and from approximately 2,400 md to approximately 0.1 md in experiment #2. Numerical results are reported as averages of several data points near the beginning and end of each experiment.

Black light images (Figure S4.5, Supporting Information) revealed channels where fluorescein-amended fluid flowed after the fracture reopened. The re-fracture flow path showed fewer distinct channels, and the second sealing experiment began with permeability reduced from the original hydraulic fracturing event. Because of these observations, it was hypothesized that some of the original pore channels were not reopened or opened with a reduced aperture during the refracturing event.

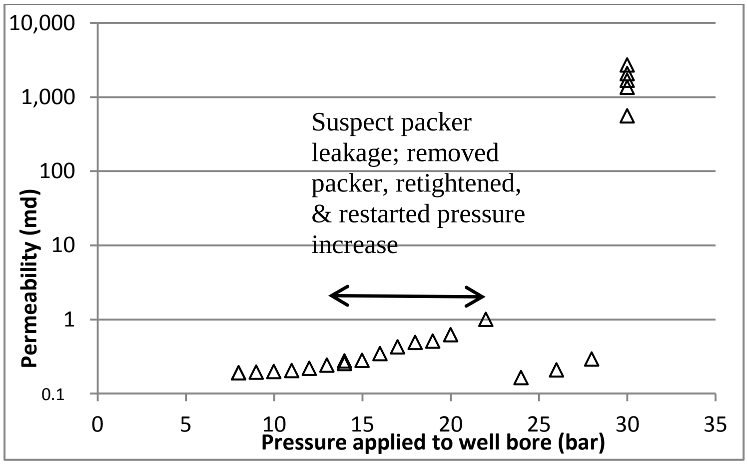

Figure 4.5. Step wise increase of applied well bore pressure acted to re-crack the sealed fracture after sealing experiment #1 (Δ) at 30 bar. The relative permeability increased from approximately 0.2 md to approximately 2,100 md after re-fracture; an increase of two orders of magnitude.

## Discussion

Toward developing field-scale relevant MICP fracture sealing technologies, an injection strategy was developed to homogenously precipitate $CaCO_3$ and minimize near-injection-point plugging, decrease permeability while increasing the treated strength of a hydraulically fractured meso-scale core and more quickly seal a core fracture. Column data (1–4) discussed within this paper have also been used to calibrate a reactive transport pore-scale ureolysis-driven MICP model which can ultimately assist with further improving injection strategies [27]. A combination of modeling and experimentation is necessary to expand these procedures toward field-relevant scale.

Several researchers have reported higher levels of mineral precipitation near the injection points in columns or other reactor studies [2, 7, 13, 30]. Extending mineral precipitation homogenously may be advantageous to sealing multiple fractures while preventing near-injection-point plugging [12, 21]. In these studies the extent of $CaCO_3$ precipitation was controlled to prevent near-injection-point plugging by (1) displacing the available $Ca^{2+}$ in the injection region during active biomineralization periods, and (2) reducing the saturation conditions immediately prior to calcium-growth media injection to prevent instantaneous precipitation.

Other MICP studies have reported changes in properties of porous materials like increased compressive strength and reduced permeability [13, 14, 47, 168]. Sand's compressive strength has been shown to increase to 570 kPa [13] and permeability was reported to decrease 15–99.9% because of $CaCO_3$ precipitation in sand-filled reactors or sandstone cores [2, 13, 19, 89, 168]. In the studies reported here, permeability was decreased up to 99% in columns and 4 orders of magnitude in core fractures. Although column sand compressive strength was not measured here, the MICP treated fracture withstood greater than three times the applied well bore pressure before refracturing.

As other researchers have noted, microbes provide nucleation sites for $CaCO_3$ to precipitate (Supporting Information Figure S4.6), and $CaCO_3$ precipitation may inactivate microorganisms or create nutrient-diffusion limitations, leading to reduced ureolysis and reduced biomineralization [37, 75, 82, 107]. Also, biofilms, particularly the extracellular polymeric substances (EPS), are generally highly hydrated and may create an environment where ions or molecules may accumulate in higher concentrations than the bulk fluid [36]. As such, maintaining the hydration and ureolytic activity of the biofilm needs to be balanced with the goal of precipitating $CaCO_3$ in shortened, field-relevant, time scales. The shortened duration to seal the core fracture in sealing experiment 2 was possibly due to immediately starting overnight resuscitation phases or increasing the daily number of calcium growth pulses. The faster observed sealing may have also been due to additional nucleation sites available from remaining $CaCO_3$ deposited in the first sealing experiment, fewer open pore channels (as observed from fluorescein tracer images), or lower initial fracture permeability, perhaps indicating smaller overall fracture aperture size.

In consideration of field relevance it is important to question the source of ureolytic organisms in the target formation. Ureolytic organisms may either need to be stimulated (biostimulation) or injected (bioaugmentation) [18]. If injected, organisms must penetrate the pore spaces of target formations, and microbial transport can be restricted by permeability, pore throat size, tortuosity of the matrix, and other complex factors such as cell stickiness or electrostatic interactions [18, 94, 95]. Should microbial injection rather than biostimulation be necessary, starved bacteria or spores might penetrate more easily and evenly; soil microbes typically are one to two micrometers in length where starved bacteria are smaller, down to a diameter of 0.3 μm and more spherical [90, 91, 163]. Since microorganisms are small and starved microbes and spores are even smaller, the MICP treatment of small aperture fractures like in the core experiments shown here may be possible with this technology.

In addition, field relevance of MICP fracture sealing also depends on economic feasibility. Assuming the use of similar injection strategies and nutrients presented within this paper but in quantities relevant to large scale fracture sealing or field-deployment, analytical grade urea, carbon, and calcium sources (12%, 18%, and 22% of media costs respectively) represent major economic impact factors. Optimizing $Ca^{2+}$ deposition efficiency and utilizing alternate carbon, urea, and calcium sources such as carbon and calcium-rich industrial waste streams, urea fertilizers, or calcium chloride ice melting products may provide cost savings in large scale ureolysis-driven MICP projects [17, 30, 73].

Several challenges exist when considering the use of this technology in relevant subsurface $CO_2$ storage site conditions including elevated temperatures, pressures, and the presence of supercritical $CO_2$ ($scCO_2$), a known antimicrobial. In the case of bioaugmentation, the use of certain mesophilic microorganisms will likely limit the sites and depth where this technology might be applied because of temperature limitations. That said, previous evidence suggests that ureolytic organisms grow in highly-saline [40, 50, 56] and high pressure environments [5] and that biofilms are resistant to the antimicrobial effects of $scCO_2$ [29]. We present evidence that evolving injection strategies produced homogeneous spatial $CaCO_3$ distribution and minimized injection-point plugging in sand-filled columns and reduced permeability in fractured sandstone. This suggests that the biofilm-induced $CaCO_3$ precipitation technology has the potential to seal fractures and improve long-term storage security of geologically sequestered $CO_2$ in subsurface storage sites like deep saline aquifers. Additional research including meso-scale high pressure experiments and modeling will help develop these techniques and improve cost efficiency toward field-scale implementation.

## Chapter Specific Supporting Information

### Supporting Information: Experimental Methods

Column and core fracture experiment tubing and pumps were disinfected and rinsed with the following successive water-based autoclaved or 0.22 μm-filtered solutions: 1% v/v bleach (Clorox, CA, USA) and 3.5% w/v Tween 80 (Acros, NJ, USA); 10% w/v NaCl (Fisher, Fair Lawn, NJ, USA); 1.26% w/v sodium thiosulfate (Fisher, Fair Lawn, NJ, USA); and 1% w/v ammonium chloride (Fisher, NJ, USA) [169].

Growth medium was prepared with 3 g of Difco Nutrient Broth (BD, Sparks, MD), 20 g of urea (Fisher, Fair Lawn, NJ), 10 g of ammonium chloride (Fisher, Fair Lawn, NJ). Calcium growth medium was prepared as growth medium with the addition of 49 g of calcium chloride dihydrate (Acros, NJ, USA) dissolved in 1 l of nanopure water. As necessary, the pH of the medium was adjusted to between 6.0 and 6.3 before the addition of calcium chloride dihydrate to prevent abiotic precipitation (the final pH of calcium-growth medium after calcium addition was 5.4 to 5.6).

Concentrations of dissolved (0.2 μm-filtered) calcium were measured by a Metrohm 732 IC detector after separation through a Metrohm Metrosep C4 150mm/4.0mm IC column in an Agilent 1100 series HPLC. The sample was pumped through the 25$^{O}$C column at 0.9 ml/min with dipicolinic acid eluent (0.1170 g/l Fluka 2,6-pyridinedicarboxylic acid (Sigma-Aldrich, St. Louis, MO, USA)) and pH adjusted to 2.7 with trace-metal-grade nitric acid (Fisher, Fairlawn, NJ, USA) in nanopure water. Results from samples are calculated by comparing the chromatograms’ peak areas to those derived from injection of multiple concentrations of a mixed cation standard solution (calibration curve).

The double packer system was constructed of two rubber elements which were axially compressed by tightening the nuts, thereby sealing against the well bore and isolating sections of the bore hole. Prior to implementation, the packer assembly was tested for leakage at injection pressures up to 55 bar and was found sufficiently leak tight up to 25 bar.

### Supporting Information: Core Porosity, Permeability, and Pore Structure Characterization

The University of Alabama-Birmingham's Mechanical Engineering Department laboratory determined permeability of Boyles Sandstone sample by steady flow [170] with correction for the Klinkenberg effect [171, 172] and by pressure-pulse decay [173]. The minimum capillary displacement pressure was measured by a method developed by Hildenbrand [174], for quantitative assessment of the potential for seepage of gas through fine-grained rocks.

The University of Alabama-Birmingham's Mechanical Engineering Department reported minimum capillary displacement pressure of 10 psi and permeability of 0.42 md by steady flow and 0.49 md based on pressure pulse decay methodology. Permeability measurements on the entire core before fracture at Montana State University revealed values of 2.2 to 2.5 md. The difference may be due to heterogeneities in the large core materials. University of Alabama-Birmingham samples were only 2.2 cm in diameter and tested in an axial orientation where the Montana State University measurement was performed on a 74.3 cm diameter core under radial flow conditions. Additionally, Leisegang bands may influence permeability in localized regions [175] causing discrepancy between the two measurement methods. Mercury porosimetry measurements performed at the Center for Advanced Mineral Processing (Montana Tech) revealed Boyles sandstone porosity of 11.7% and an average pore diameter of 0.75 μm.

## Supporting Information: Thin Section Analysis

Vertical and horizontal thin sections from samples of Boyles sandstone revealed very fine to coarse heterogeneous quartz sandstone with significant proportions of orange-red detrital clay and pores free of cement. The sample porosity was determined to be dominated by feldspar-moldic porosity and lesser inter-particle porosity. Most pore throats were thin spaces among tightly packed sand particles and where porosity was relatively low, pore throats were long and tortuous; where porosity was higher, pore throats were shorter and straighter. In the most porous areas some pore throats were wide enough to show measurable width under the petrographic microscope (Figure S4.1). Porosity ranged from negligible to about 30% on the scale of a few millimeters and averaged approximately 10%.

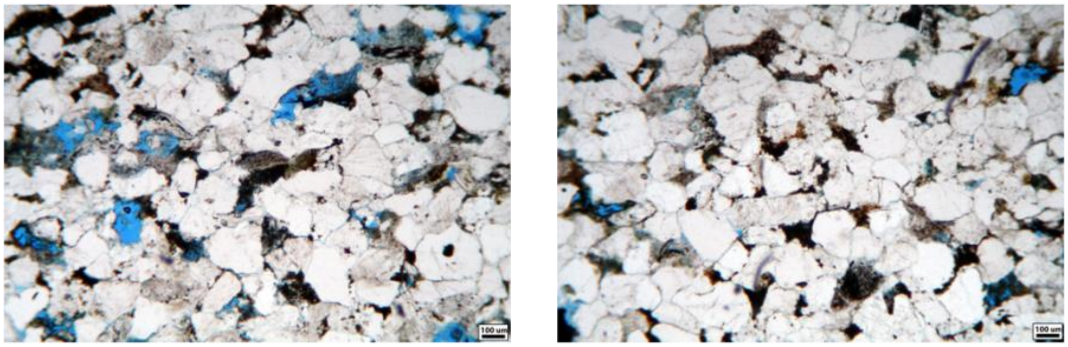

Figure S4.1. Thin section of Boyles sandstone core from petrographic microscope in plane polarized light. Blue epoxy reveals pore spaces. Image (left) depicts a higher porosity sub-sample of the core, where image (right) shows lower porosity. Orange-red detrital clay can be seen in spaces of the sample (right).

## Supporting Information

### XRD Analysis of Minerals

The collected particles were acetone mounted on glass slides prior to analysis with X-Ray Powder Diffraction Spectrometer (XRD) (Scintag X-GEN 4000 XRD) at the Image and Chemical Analysis Laboratory at Montana State University. The particles were scanned from 20.0 to 65.0 degrees at 1 deg/min and DMSNT analysis software (Scintag) was used to characterize the mineralogy of the samples.

XRD spectra from the control, an internal well bore scraping, and a scraping of the fracture on the outside of the core at the termination of the experiment was compared to reference spectra. XRD results of the original Boyles sandstone control revealed only the presence of quartz ($SiO_2$) (Figure S4.2a). Spectra from the internal well bore (data not shown) and the outer circumference fracture region, after biomineralization indicate the presence of quartz and calcite along with either calcium iron hydroxide or vaterite (Figure S4.2b) as indicated by the presence of one single peak at approximately 33 degrees. A strong positive identification could not be determined due to low signal intensity of those minerals in the sample.

(a) Control Spectra:

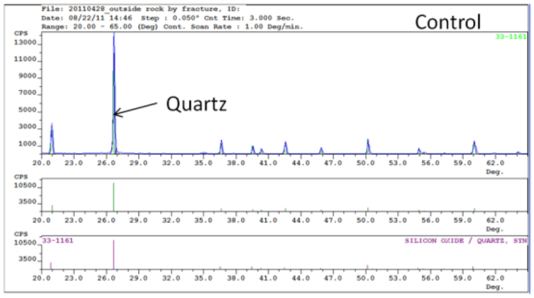

(b) Fracture Sample Spectra:

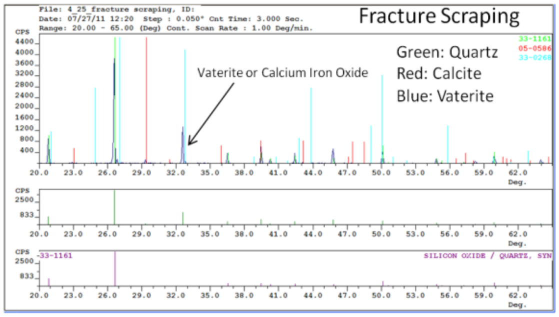

Figure S4.2. Spectra from XRD analysis (a) Control, (b) Fracture region scraped after biomineralization and subsequent re-fracturing.

Supporting Information: Additional
<u>Observations and Results</u>

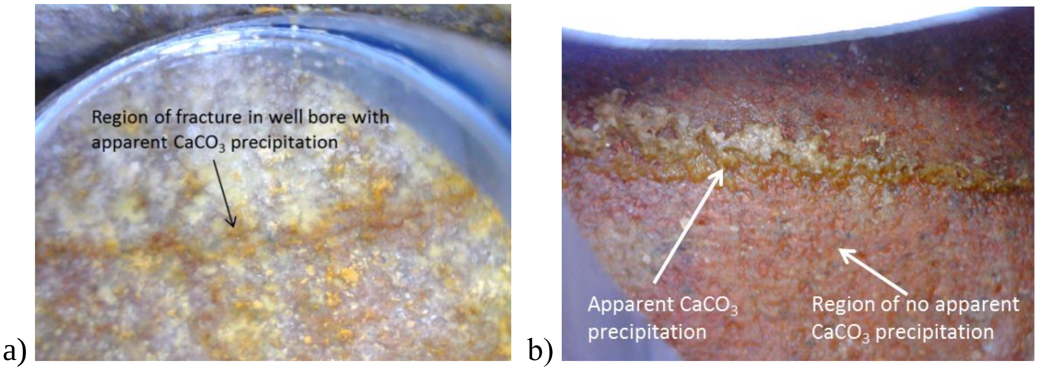

Figure S4.3. Apparent $CaCO_3$ precipitation observed in the well bore via endoscopy. (a) Arrows point to the primary horizontal fracture which was strengthened with biofilm-induced $CaCO_3$ precipitation, (b) arrows show regions of apparent $CaCO_3$ and an area where no apparent $CaCO_3$ is observed.

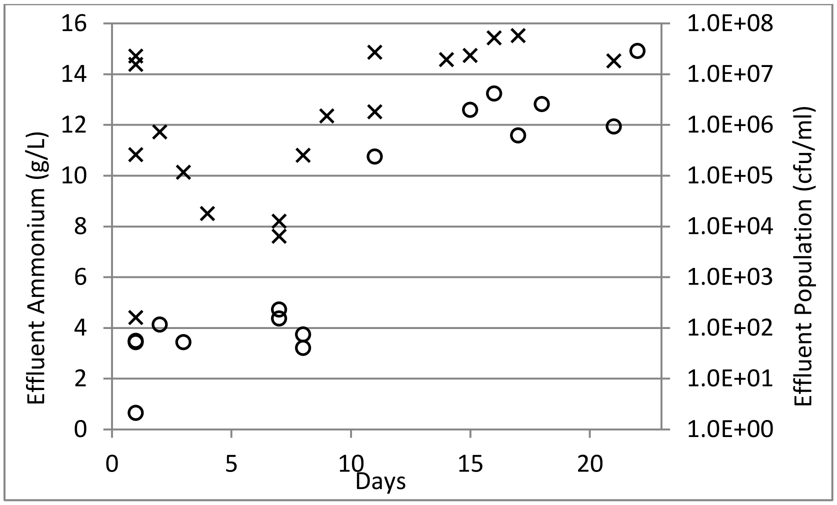

Figure S4.4. Residual effluent concentrations of (o) $NH_4$+ and (x) culturable microorganisms in the collected core fracture sealing experiment #1 effluent sample. Values remain higher after changing the injection strategy to include overnight resuscitation of the biofilm following day 14 in core sealing experiment #1.

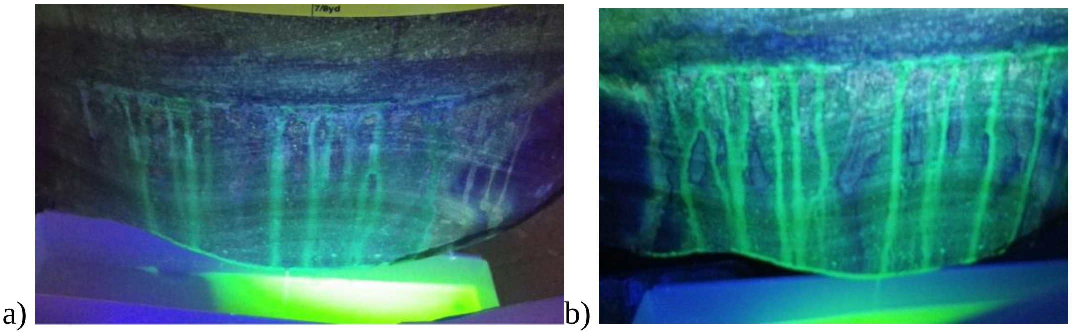

Figure S4.5. Black light images of fluorescein-amended fluids flowing from the fracture (a) Image of fluorescein-amended water exiting fracture during applied pressure of 30 bar after sealing experiment #1 when it re-fractured with fewer flow channels. (b) Image of the first fluorescein-amended calcium medium injection during sealing experiment #1 showing more numerous flow fingering or channels exiting fracture.

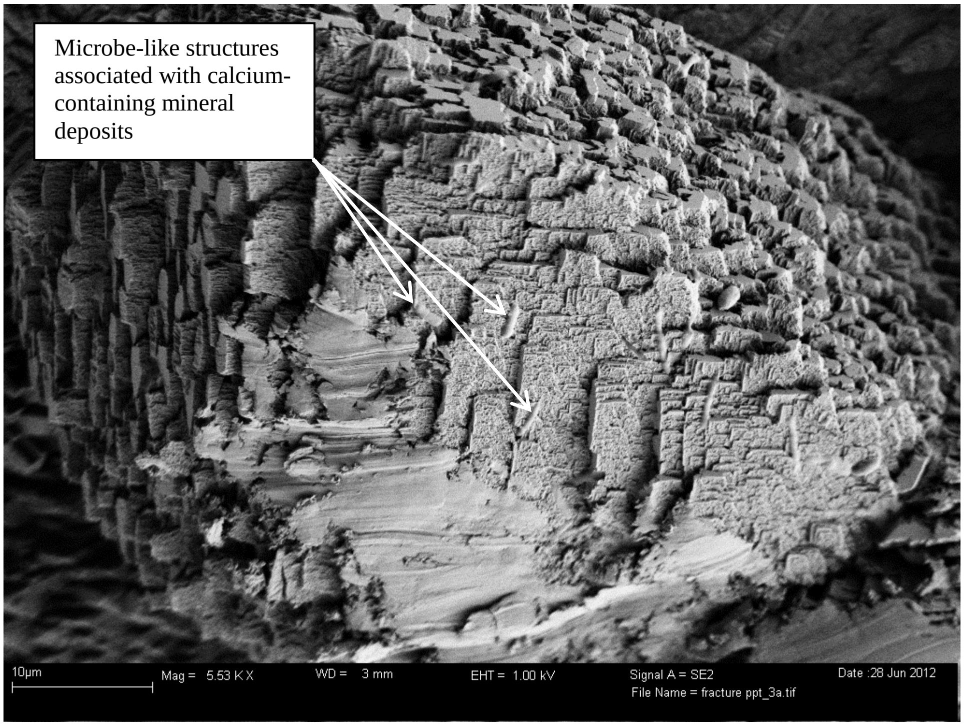

Figure S4.6: Scanning electron micrograph of microbe-like structures associated with calcium-containing mineral deposits (confirmed with EDX but data not shown).

# CHAPTER FIVE

# A MESO-SCALE TEST VESSEL FOR THE EXAMINATION OF HIGH PRESSURE PROCESSES: MICROBIALLY-INDUCED CALCIUM CARBONATE PRECIPITATION (MICP) TREATMENT OF HYDRAULIC FRACTURES

## Contribution of Authors and Co-Authors

Manuscript in Chapter 5

Author: Adrienne J. Phillips

Contributions: Designed and performed experimental work, analyzed data. Wrote and revised manuscript.

Co-Author: Joachim Eldring

Contributions: Contributed to experimental design and writing and revision of the manuscript with comments and feedback.

Co-Author: Randy Hiebert

Contributions: Contributed to the experimental design and contributed to revision of the manuscript with comments and feedback.

Co-Author: Ellen Lauchnor

Contributions: Contributed to experimental design and to the revision of the manuscript with comments and feedback.

Co-Author: Andrew Mitchell

Contributions: Contributed to the revision of the manuscript with comments and feedback.

Co-Author: Alfred Cunningham

Contributions: Contributed to experimental design and to the revision of the manuscript with comments and feedback.

## Contribution of Authors and Co-Authors Continued

Co-Author: Robin Gerlach

Contributions: Contributed to experimental design and to the revision of the manuscript with comments and feedback.

Co-Author: Lee Spangler

Contributions: Contributed to the revision of the manuscript with comments.

# Manuscript Information Page

Phillips, A.J., Eldring, J., Hiebert, R., Lauchnor, E., Mitchell, A.C., Gerlach, R., Cunningham, A., Spangler, L.
Journal of Petroleum Science and Engineering
Status of Manuscript:
__X__ Prepared for submission to a peer-reviewed journal
____ Officially submitted to a peer-review journal
____ Accepted by a peer-reviewed journal
____ Published in a peer-reviewed journal

Elsevier
In preparation.

## Abstract

A meso-scale high-pressure vessel for testing subsurface relevant processes under simulated *in situ* pressures has been designed and constructed. This system is capable of providing pressures up to 96 bar and is capable of housing porous media samples such as rock cores up to 74 cm in diameter and up to 50 cm high. A valved switchboard allows for fluids to be pumped into the vessel under radial flow conditions and fluids being extracted from the vessel to be sampled in a spatially resolved manner. The switchboard assembly also allows for the monitoring of real time pH and conductivity of either the injected or effluent fluids. The vessel has an optional heating jacket to control simulation temperatures. The system can be used to investigate a wide range of subsurface relevant processes, including those related to a variety of oil and gas industry interests such as fracture sealing for improving the security of geologic carbon sequestration.

As an example, this paper describes the use of the vessel to study ureolysis-driven calcium carbonate precipitation to reduce the permeability of a hydraulically fractured core under relevant subsurface pressure conditions (44 bar). The core was inoculated with *Sporosarcina pasteurii* and biofilm growth was promoted in the fracture, followed by injection of calcium and urea containing growth reagents to promote saturation conditions favorable for ureolysis-driven $CaCO_3$ precipitation. The biofilm-induced $CaCO_3$ mineralization treatment reduced the permeability in the mineralized fracture more than two orders of magnitude. This single high pressure experiment suggests MICP can be used to reduce permeability in fractures under relevant subsurface conditions. This study also suggests the high pressure vessel is suitable for testing biogeochemical

processes in meso-scale porous media samples under pressure. The high pressure test system could also be well suited for studying microbially–enhanced methane production from coal, well bore and cement integrity challenges with corrosive fluids, proppant and hydraulic fracturing fluid investigations, bacterial induced corrosion or biofouling among many other industry-related biogeochemical processes.

## Introduction

Laboratory studies of geochemical and biogeochemical processes are often limited to the small core scale and may not incorporate reasonable three dimensional and geologic heterogeneity [176]. Field tests are expensive, laborious and often field opportunities are limited. Therefore, to prepare for field scale experiments or technology deployment it is important to scale up to study more realistic *in situ* processes. Intermediate experiments performed at the meso-scale (defined here as ~1/2 meter to meter scale) can more closely simulate real-world environments by incorporating larger scale phenomena that are not captured with typical lab scale experiments [177] and may lend knowledge valuable in the transition to the field scale [18] .

Aside from commercially available core analysis equipment, such as those available from Core Laboratories (Texas, USA), multiple high pressure vessels have been designed and constructed for the study of methane hydrates [177-179], sampling and analysis of deep sea microbiology [180] and a large-scale high pressure vessel for purposes of petroleum industry-related studies [176]. Studying biogeochemical processes under relevant subsurface conditions is important because (1) microbial activity can be impacted by pressure conditions [181-184], (2) chemical reactions (particularly gaseous reactions) may be enhanced or inhibited by high pressure, and (3) porous media characteristics like porosity and permeability can be altered by pressure [185, 186]. As such, a meso-scale high-pressure vessel (described herein) has been constructed and used to study biogeochemical processes in porous media samples under relevant subsurface pressures.

Microbially-induced calcium carbonate precipitation (MICP), particularly ureolysis-driven MICP, has been studied extensively for a wide range of engineering applications including enhanced oil recovery [19], improving construction materials [9, 10, 187], consolidating porous media [13, 16, 31, 108], remediating environmental contaminants [21, 24, 26, 55, 63, 102] and enhancing the storage security of geologically sequestered $CO_2$ [4-6, 107]. Ureolysis-driven MICP involves microbes, particularly in an attached form, also known as biofilm, to influence the saturation conditions of calcium carbonate to favor precipitation. The microbes produce the enzyme urease which catalyzes the hydrolysis of urea to form carbonate and ammonium. In the presence of calcium, the hydrolysis of urea can create favorable saturation conditions for the precipitation of calcium carbonate [37, 38, 45] (Eq.1-2).

$$CO(NH_2)_2 + 2H_2O \longrightarrow 2NH_4^+ + CO_3^{2-} \qquad (1)$$

$$Ca^{2+} + CO_3^{2-} \longleftrightarrow CaCO_3\,(s) \qquad (2)$$

Ureolysis-driven MICP was chosen for the first study with the high pressure test vessel to make relevant comparisons of permeability reduction via MICP at different confining pressures. It has been shown previously that ureolysis-driven MICP can occur at elevated pressures relevant to those encountered at geologic $CO_2$ sequestration sites [3, 5].

Ureolysis-driven MICP was also used previously to reduce permeability in a hydraulically fractured Boyles Sandstone core at ambient pressure [6]. Also, several MICP field scale experiments have previously been performed [14, 17, 21]. Yet, MICP at both elevated pressures and at meso-scale has not been previously demonstrated. Experiments performed under relevant subsurface conditions and on a near-wellbore scale allow for the testing of injection strategies, monitoring of the population of microbes, and gathering of data to transition from the laboratory scale to the field-scale.

The purpose of this paper is to describe a new high pressure test vessel capable of the examination of meso-scale subsurface relevant processes. To illustrate the vessel capabilities, an experiment was carried out under elevated pressure conditions to study the permeability reduction in a hydraulically fractured sandstone core due to ureolysis-driven calcium carbonate precipitation.

## Materials and Methods

### Vessel Design and Construction

The pressure vessel was designed to inject and extract pressurized aqueous solutions, supercritical carbon-dioxide, or other fluids or gases into meso-scale porous media samples (such as rock cores) of up to 74 cm diameter and 50 cm in height under reservoir relevant pressure and temperature conditions. In order to keep the vessel fabrication cost and weight low the vessel was specified for a maximum allowable working pressure (MAWP) of 96 bar at 43°C. Since the super-critical point for carbon-dioxide resides at 74 bar and 31.5°C, this means a differential injection pressure of up to 22 bar over the $CO_2$ critical pressure can be safely applied. The vessel was designed, fabricated and tested according to ASME standards by Alaskan Copper Works in Seattle, Washington.

The vessel is comprised of a bottom sided blind flange of 132 cm diameter and a flanged shell with an inner diameter of 76 cm and 54 cm height. The bottom blind flange is mounted by means of twenty-eight 2”-8 UN x 14” studs and heavy hex nuts that are tightened to 270 Nm. The flange is sealed against the vessel with a 9.5 mm wide Viton O-ring of Durometer 88 (Shore A).

The vessel cap has a round access port with an inner diameter of 20 cm. The access port is covered by a raised blind flange of 42 cm diameter. This raised top blind flange has 12 ports that allow for fluid delivery, sampling and extraction under pressure, as well as for the installation of necessary safety features. The top blind flange is mounted by means of twelve 1.125” – 8 UN x 5” studs and heavy hex nuts with a Class 600 spiral gasket used to seal the flange to the shell.

The dry weight of the vessel is 2925 kg, not including the supporting frame that is mounted to the bottom blind flange. All wetted parts of the vessel were fabricated from a 304 stainless steel. In order to reduce cost, the bottom flange was made from an SA-105 carbon steel cladded with a 12.4 mm thick 304L stainless steel plate. The mass of the vessel’s flanged top shell is 1350 kg. A gantry-style overhead crane (Contrax Industries, Neenah, WI) specified to 2 tons is used to lift the top shell, and to load or unload heavy samples. An optional heating jacket can be applied to the outside of the vessel should experiments under higher or lower temperature than ambient temperature be desired.

The pressure vessel configuration, with the flat main blind flange located at the bottom, was dictated by height constraints in the laboratory, plus the need for a frame underneath the vessel that assured safe and easy transportation with a pallet jack. As such, a flat versus spherical bottom shell was constructed.

## Fluid Delivery & Sampling System Design

The fluid delivery and extraction system (Figure 5.1) consists of two ISCO D1000 (1000ml) (Teledyne, Nebraska, USA) positive displacement pumps, a packer assembly [6], an optional sampling jacket, an optional heating jacket and custom designed valved switchboard. The fluid delivery into or extraction from the vessel can be flow-rate or pressure controlled.

Figure 5.1. Meso-scale pressure vessel with fluid delivery and extraction system. Shown on the left is the custom designed switchboard for directing injection fluids, fluid sampling and metering. In the center is the custom fabricated pressure vessel. On the right are two positive displacement pumps (Isco) with controller and a laptop computer for data acquisition.

Internal Vessel Sampling Jacket. The system was designed with an optional sampling jacket, although the jacket was not used in the experiment described in this paper. The additional space required for the sampling jacket reduces the maximum allowable porous media sample or core diameter to 71 cm. In the event that a non-homogenous or fractured core specimen is used in the vessel, fluids exiting the sample core at different locations on the circumference may vary in flow velocity or composition. The optional internal fluid sampling jacket was designed to selectively sample fluids from certain regions while under pressure (Figure 5.2).

The sampling jacket was manufactured from a 20 ga. 304 stainless steel sheet metal rolled into a circular sleeve (JE Soares, Belgrade, MT, USA). The sampling jacket diameter is adjustable by an overlapping section that can be tightened against the sample with hose clamps. Flexible tubing can be used to seal between the core and the sleeve to partition the sampling regions. Fluids from six individual sampling regions could be extracted through pipe inserted between the sample and sleeve which are connected to a manifold (Figure 5.3) and routed to the switchboard. The amount of intermixing between fluids that exit the core, and the fluid used to maintain the required confining pressure, could be reduced by filling the space between the sample and the sampling jacket with porous media such as small gravel or polymer balls.

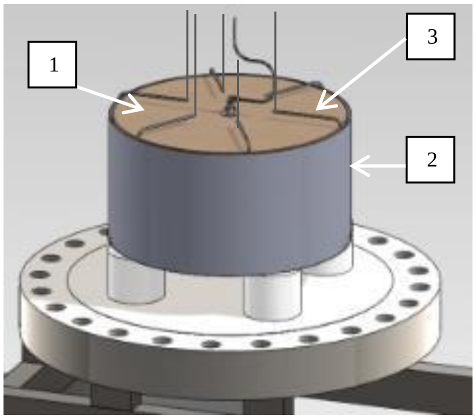

Figure 5.2. Illustration of a sheet-metal sampling jacket mounted around the sample core (1). Compressible tubing inserted in between the stainless steel sleeve (2) and the sample (1) can divide the space into six compartments for spatially selective sampling through pipes (3) inserted into the compartments connected to a manifold and ultimately the valved switchboard.

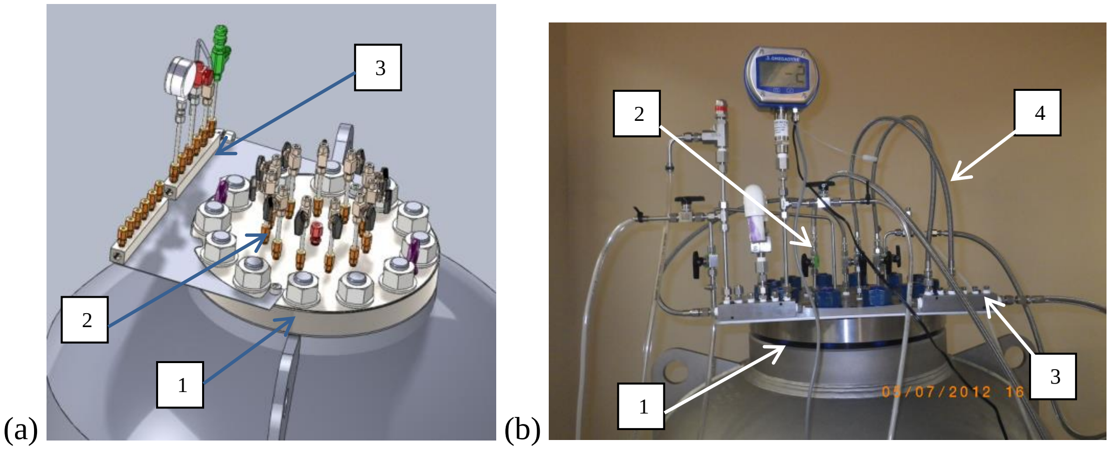

(a) (b)

Figure 5.3. Top flange manifold illustration and image. (a) Illustration of vessel top flange (1), valve-ports (2) and manifold (3) are connected to each other by way of flexible stainless hoses and then can be used for sampling, injection and extraction of fluids and connection of safety components (b) image of the manifold and flexible high pressure hoses (4) connecting the sampling ports from the top flange to the manifold which is then connected to the valved switchboard (Figure 5.4).

<u>Valved Switchboard.</u> A valved switchboard was designed and assembled in order to allow for convenient and safe switching of fluid to different pathways or functions. A multitude of operational steps in connection with the experimental process can be exercised with this switchboard, such as (1) filling and venting the packer or vessel, (2)

injecting a microbial inoculum, (3) cleaning and purging the system between experimental steps, (4) collecting influent and effluent samples and (5) monitoring real time pH and conductivity.

Figure 5.1 presents a side/front view of the switchboard together with the connecting pipes that lead to the vessel's top flange. Figure 5.4 shows the back view of the valve switchboard assembled from stainless steel piping and 210 bar rated 2 & 3-way valves to minimize potential corrosion (Swagelok, Idaho, USA). Figure 5.5 illustrates the system diagram which was used to construct the valved switchboard assembly.

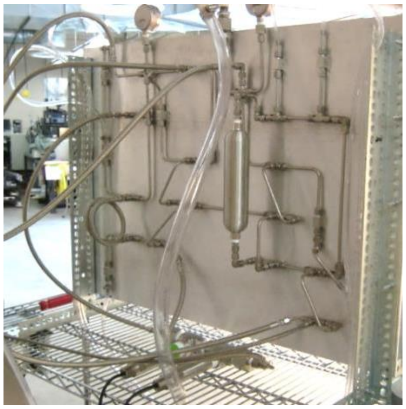

Figure 5.4. Image of the valved switchboard system. The back side of valved switchboard showing the sampling loop (coiled hose to lower left), a pressured reservoir for injection of inoculum (center-right), and the pH- and conductivity sensors (lying on wire frame shelf (Barben Analyzer Technologies, Nevada, USA).

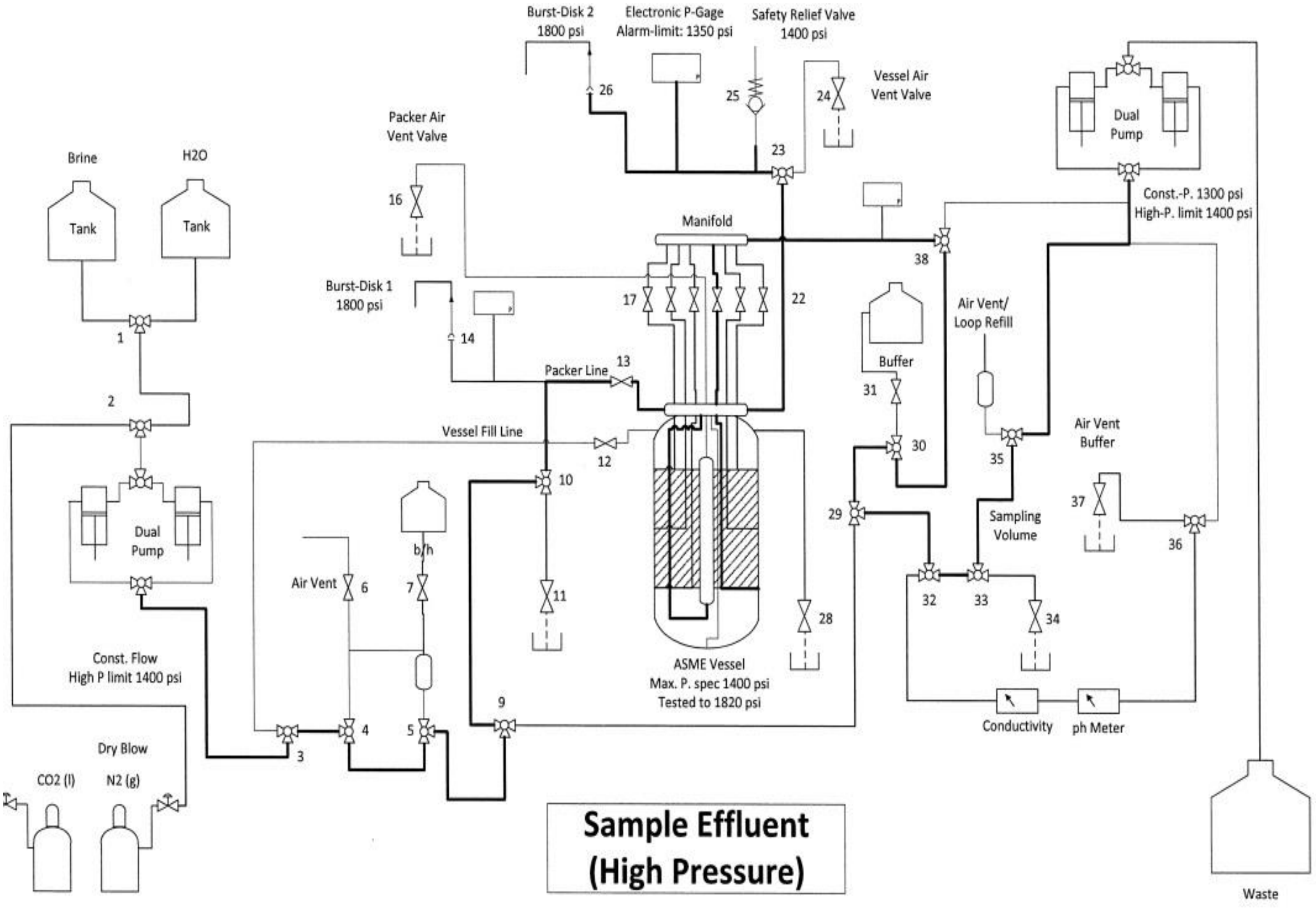

Figure 5.5. Schematic of the valved switchboard system. Schematic of process of sampling the effluent with the switchboard, where fluids enter the vessel from the pumps and lines shown on the left hand side of the vessel and leave the vessel from lines shown on the right hand side. The numbered valves allow for specific valve switching schematics or protocols to be developed for other operations. The bold lines highlight sampling of the effluent from the vessel under high pressure through the sampling loop.

### Safety and Control

Since the vessel can be used to investigate biological or corrosive processes, it is a concern that fouling could impair the function of the safety equipment. To minimize the risk of safety mechanism failure, several redundant safety mechanisms were installed that would be triggered in case of an unacceptable pressure situation including:

a) The ISCO/Teledyne pumps are set to not exceed the MAWP,
b) An independently operated pressure sensor (Omega, Connecticut, USA) mounted to the top of the vessel to shut down pump flow in an under- or over-pressure situation combined with electronic notification (e.g. SMS or email) to research personnel,
c) A burst disk (Zook, Ohio, USA) installed in the packer injection piping system and at the vessel,
d) A pressure relief valve set to open at 1400 psi to maintain vessel pressure below MAWP (Swagelok, Idaho, USA).

## Experimental

### Vessel and Core Preparation

A Boyles Sandstone core was hydraulically fractured as previously described by Phillips et al. (2013) [6]. Immediately after fracturing, the sandstone core was loaded into the high pressure vessel [3]. A sampling pipe was placed directly below the fracture to collect samples of the fluid exiting the fracture (Figure 5.6). The vessel was assembled around the core and filled with a 2 g/L NaCl brine and tap water solution. The core was allowed to saturate over two days and the vessel was topped off with brine prior to sealing. Initial fracture hydraulic conductivity, subsequently converted to permeability was estimated by flowing brine through the packer system, monitoring flow and differential pressure and calculating permeability based on equations for a confined aquifer in radial flow conditions [165].

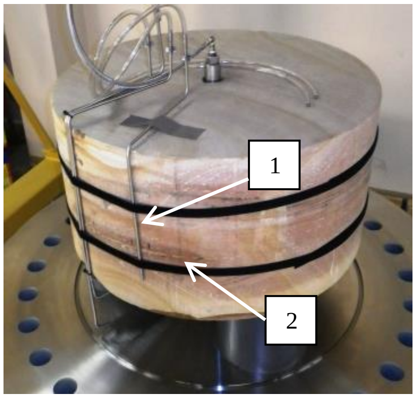

Figure 5.6. Image of core prior to high pressure biomineralization experiment. The core was situated on the base plate of the vessel and a sampling tube (1) was placed directly under the fracture to collect fluids exiting from the fracture region (2).

## Fracture Sealing Experiment

The confining pressure was set to 44 bar by using the Teledyne pump to pressurize the brine in the vessel. This pressure was set to mimic relevant subsurface conditions at ~457 m below ground surface, corresponding to a potential target field deployment site in the Boyles Sandstone layer of the Pottsville Formation in Alabama, USA (Richard Esposito, personal communication). As previously described by Phillips et al. (2013), and Cunningham et al. (2013), growth medium containing 0.33 M urea was injected into the core via the double packer system prior to injecting a culture of *Sporosarcina pasteurii*. Prior to inoculation, the culture was centrifuged at 6000 rpm, re-suspended in fresh growth medium and injected through the double packer into the fracture at 20 ml/min. Following a 4.5 h attachment period of no flow, growth medium was injected for 7 h to promote biofilm formation and then calcium pulses (0.33 M urea and calcium) were initiated. Calcium pulses were performed as previously described to minimize near-injection-point plugging [6, 27]. During the experiment, differential pressure and flow rate were monitored to assess changes in permeability over time. Effluent from the sampling region directly below the fracture was monitored in real time to determine changes in chemistry using high pressure pH and conductivity probes (Barben Analyzer Technology, Nevada, USA). Ureolysis can be monitored by measuring the increase in conductivity over time, as urea is non-ionic but the products of ureolysis are ionic species (Eq. 1) [77]. Additionally, effluent samples were collected during each pulse to determine culturable cell concentrations through drop plate methods [164]. In the beginning of the experiment two colony morphologies were observed on the agar plates. These colonies were used to inoculate filter sterilized growth medium and pH and ammonium production after 24 hours were used to confirm the organisms' potential for ureolysis.

During the first 19 calcium injections, a 24-hour cycle was as follows: (1) injection of calcium with a 4 h stagnation period, (2) second injection of calcium with a second 4 h stagnation period, (3) injection of growth medium injection with a 16 h growth period. However, a consistent permeability reduction had not been achieved by calcium pulses #19, which differed from previous ambient condition experiments where the fracture sealed after 14 and 7 calcium pulses [6]. It was unknown whether the elevated pressure or the presence of confining fluids were impacting the precipitation rates or reducing the efficiency of sealing. Therefore, to compensate for potential negative impacts from pressure or confining fluid conditions, 1) the urea and calcium concentrations of the media were increased to 0.43M to provide more reactants for precipitation and 2) the 24-hour cycle changed to allow more time for biomineralization to occur (1h of growth medium injection, injection of calcium with a 4-6 h no flow period, then a second injection of calcium and no flow period for 18 hours).

The experiment continued until flow rates and differential pressures had reached similar conditions to those observed in previous ambient condition sealing experiments in the same core sample [6]. Then the vessel was depressured, confining fluids were emptied and the vessel was disassembled for cleaning and maintenance. Since the high pressure vessel does not contain view ports to visualize whether the fracture zone was sealed, permeability was an important metric to evaluating success of the treatment.

Samples of precipitates observed on the outside of the fracture and the inside of the well bore were collected for analysis including stereoscopy, X-ray diffraction (XRD) and scanning electron microscopy (SEM). Portions of the precipitate samples were ground fine using an ethanol rinsed mortar and pestle prior to analysis with a X-Ray Powder Diffraction Spectrometer (XRD) (Scintag X-GEN 4000 XRD) at the Image and Chemical Analysis Laboratory (ICAL) at Montana State University. The samples were scanned from 20.0 to 65.0 degrees at 1 deg/min and DMSNT analysis software (Scintag) was used to determine mineralogy from the sample spectra. Other portions of the samples were first imaged via stereomicroscopy (Nikon, New York, USA) in the Center for Biofilm Engineering Microscopy Facility and then mounted and coated with iridium for imaging (1 kV) and elemental analysis (20 kV) with a Zeiss Supra 55 Field Emission

Scanning Electron Microscope coupled with Energy Dispersive Spectroscopy (Zeiss, Germany) also located in the ICAL.

Finally, the strength of the fracture sealing was determined by (1) applying constant well bore pressure of 8 bar for 1.75 hours and (2) step-wise increasing the applied well bore pressure until fluids were observed to be clearly flowing from the fracture.

## Experimental Results and Discussion

### Initial Equivalent Permeability

Prior to starting the fracture sealing experiment the average equivalent permeability [188] of the fracture at a flow rate of brine at 20 ml/min was 26,000 ± 4,100 mD.

### Fracture Sealing and Strength Assessment

Urea hydrolysis was monitored in the effluent from the vessel during the calcium and growth pulses by measuring $NH_4^+$ production and increases in conductivity (Figure 5.7a). Over the course of the experiment, $NH_4^+$ and conductivity on average increased, suggesting active ureolysis was maintained. The initial large jump in conductivity corresponded to an increase in ammonium concentration which immediately followed the biofilm growth stage of the experiment.

During the first three calcium pulses two colony morphologies were observed on plated dilutions of the effluent samples. After isolating the colonies on urea containing agar, only one of those colony morphologies was observed to be ureolytic. The ureolytic colony morphology was light tan and round, which is typical of the colonies observed in a pure culture of *S. pasteurii*. After the third calcium pulse, only the ureolytic *S. pasteurii*-like organisms were culturable from effluent samples to a high concentration of 2.9 x $10^7$ cfu/ml (Figure 5.7b) which is comparable to the maximum population (5.2 x $10^7$ cfu/ml) observed in the effluent of the previously described high pressure experiment [5]. These data suggest that organisms in the non-sterile confining fluids did not out-compete the injected *S. pasteurii* cells. Note: While no other colony morphologies were observed past day three on the aerobic agar plates, anaerobic culturing conditions were not performed and it is possible that anaerobic organisms were present.

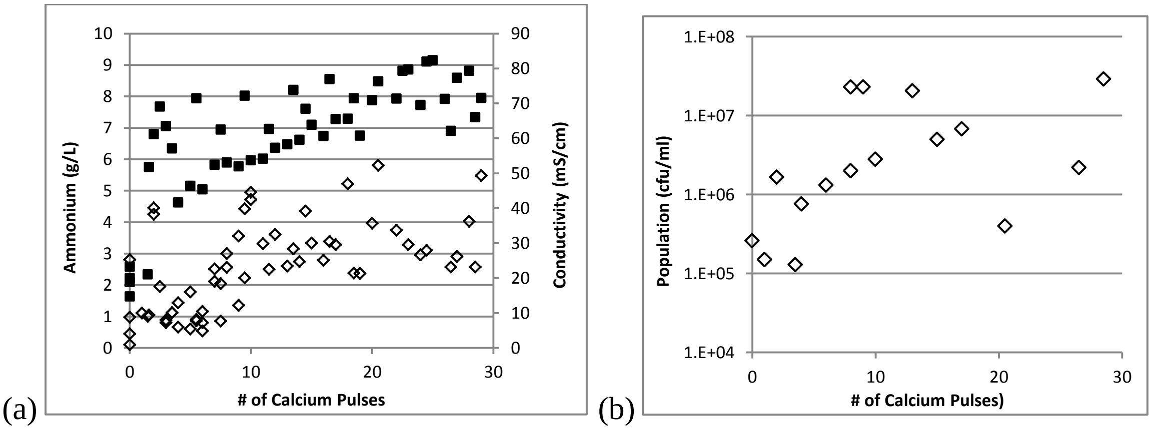

Figure 5.7. Effluent ammonium, conductivity and culturable cell concentrations from vessel effluent samples. (a) Effluent ammonium concentration (◊) and conductivity (■). Ammonium concentration increased from an average of 1.4 g/L in calcium pulses #1-6 to an average of 3.0 g/L for calcium pulses #6-28. Conductivity quickly increased from an average of 19.9 mS/cm to an average of 67.1 mS/cm after the biofilm growth stage. (b) The culturable effluent population averaged 7.8 x$10^6$ cfu/ml.

An initial reduction in equivalent permeability was observed after three calcium pulses, but the reduction was not maintained during an 8 bar, 1.75 hour strength test. After increasing the reagent concentrations and altering the injection strategy to allow for longer biomineralization periods, fracture equivalent permeability was observed to decrease (Figure 5.8). Previous control experiments resulted in no reduction in permeability when column experiments were pulsed with similar media and tested either without organisms or inoculated with non-ureolytic organisms [166]. It should be noted that as compared to previous ambient pressure experiments reported in Phillips et al. (2013), the reduction in equivalent permeability took longer with more calcium pulses in the high pressure system than under ambient conditions (28 calcium pulses instead of 14 and 7 calcium pulses in the two ambient condition experiments) [6]. It is possible that the pressure conditions or the confining fluids themselves impacted ureolysis, precipitation rates or efficiency. After 28 calcium pulses (21 days post inoculation) the experiment was terminated as the flow rate and differential pressure had reached 0.3 ml/min and 3.5 bar, respectively, similar to the metrics reached in the ambient pressure sealing experiments and it was assumed the fracture had been sealed.

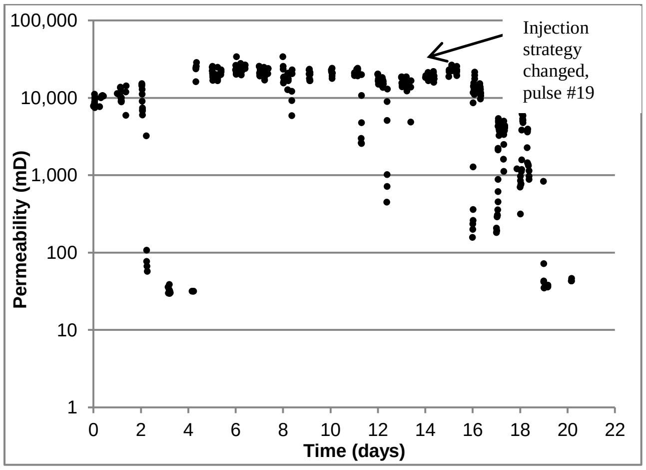

Figure 5.8. Calculated permeability over time (days of experiment). Permeability reduced from approximately 26,000 mD to 40 mD over the course of 21 days and 28 calcium pulses. The injection strategy was altered after 19 calcium pulses (14 days) to increase the concentration of reagents and increase the time allowed for biomineralization [3].

After the vessel was drained and disassembled, precipitates were observed on the circumference of the core in the region of the fracture and in the well bore (Figure 5.9). SEM and stereoscopy showed the presence of calcium-containing minerals associated with cell-like structures (Figure 5.10) and XRD (data not shown) confirmed that the observed minerals were predominantly calcite.

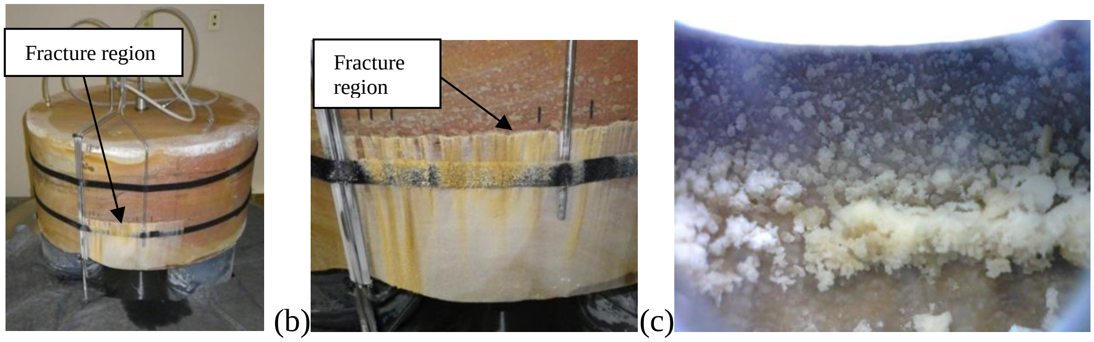

(a) (b) (c)

Figure 5.9. Precipitates were observed after the high pressure experiment in the region of the fracture. (a) and (b) precipitates formed in the region of the fracture, (c) precipitates were observed inside the simulated well bore.

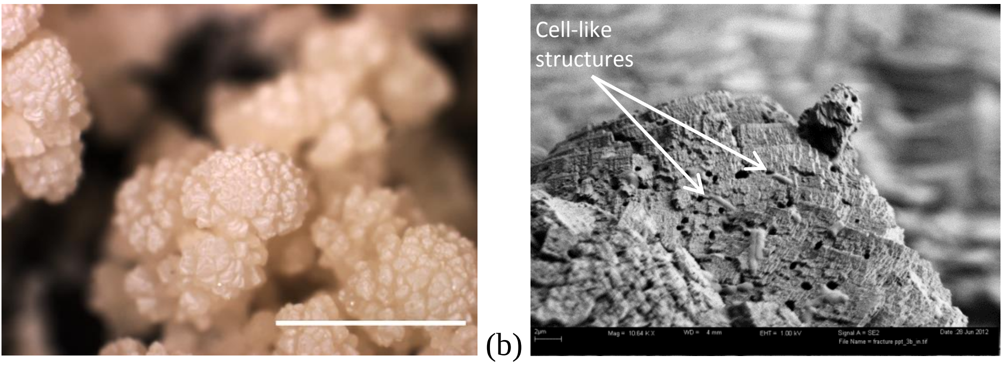

(a) (b)

Figure 5.10. Calcium-containing minerals formed in the fracture region. (a) Stereomicroscope image of minerals formed in the region of the fracture; the scale bar is 1mm. (b.) Scanning electron microscope image of possible cell-like structures associated with calcium-containing minerals obtained from the fracture region.

Following sample collection, the fracture was strength tested without confining pressure. First, 8 bar of well bore pressure was applied for 1.75 hours. During this test, flow was observed from the fracture for the first 20 minutes. After 20 minutes, no flow was observed from the fracture for the remainder of the 8 bar strength test (Figure 5.11). This observation was not clearly understood since before depressurization of the vessel, the fracture was assumed to be sealed due to the reduced equivalent permeability that coincided with the values achieved during the ambient sealing experiment. Two possible explanations are suggested (1) even though the fracture itself may have been filled with mineral, residual saturation in the core matrix above and below the fracture was pushed out toward the circumference of the core due to the pressure field in the well bore or (2) depressurization of the vessel damaged the mineral seal and the brine pumped into the fracture during the 8 bar strength test caused loosely bound mineral precipitates to be re-distributed before re-blocking open flow channels.

After 20 minutes, no flow was observed for the remainder of the 8 bar fracture strength test. Thus after 1.75 hours, well bore pressure was step-wise increased. At a well bore pressure of 26 bar, fluids were observed to be flowing from the fracture (Figure 5.11). During the re-fracturing event, the flow rate increased rapidly from 4 ml/min at 24 bar differential pressure to 108 ml/min at 26 bar differential pressure. This is similar to the well bore pressure necessary to re-open the fracture (30 bar and 32 bar) in the two previously described ambient pressure sealing experiments [6].

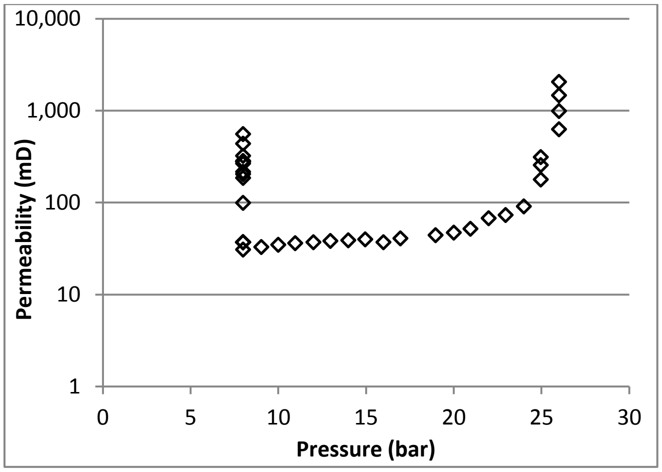

Figure 5.11. Calculated equivalent permeability of the fracture during the strength test. Fracture flow was observed in the first 20 minutes of the 8 bar 1.75 hour test, then no flow was observed until after increasing the applied well bore pressure step wise to 26 bar. At 26 bar of applied well bore pressure the equivalent permeability increased from ~40 mD to 2,500 mD and significant flow was observed from the fracture.

## Summary and Conclusions

Here we describe the design and construction of a high pressure vessel, which is capable of housing samples up to 74 cm in diameter and up to 50 cm in height. The vessel is rated to operate at pressure up to 96 bar. The valved switchboard allows fluids to be pumped into the vessel under pressure and radial flow conditions. Sampling of both influent and effluent fluids can be accomplished both spatially resolved and under pressure. The switchboard is equipped with real-time monitoring equipment for pH and conductivity. The vessel can be temperature controlled and possesses multiple pressure safety mechanisms.

In an initial experiment, ureolysis-driven microbially-induced calcium carbonate precipitation (MICP) was employed to reduce the equivalent permeability of a hydraulic fracture in a sandstone core under high pressure conditions. The equivalent permeability reduction was attributed to precipitation of calcium carbonate inside the fracture. The final strength of the fracture seal in this single replicate experiment was similar to the strength observed under ambient pressure conditions previously described by Phillips et al. (2013) [6]. This initial experiment also demonstrated some of the capabilities of the meso-scale high pressure vessel such as the use of pH and conductivity monitoring and effluent sampling abilities.

During the scale-up of new technologies, such as ureolysis-driven MICP, meso-scale experiments, such as the one described here-in, can provide valuable insight. First, reagent concentrations and biomineralization time periods were increased to overcome possibly reduced reaction rates due to an impact from confining fluid or pressure conditions. Field scale conditions may present inhospitable environments to MICP treatment and researchers may have to be prepared to alter injection strategies to overcome those disadvantages to achieve treatment goals. These meso-scale experimental observations will contribute toward the development of effective injection strategies at the field scale.

This meso-scale high pressure test system can be used to (1) evaluate laboratory-scale developed processes under high pressure and at larger scale, (2) mimic field scale conditions but with ability to monitor more parameters than in field, and (3) study a radial flow configuration which would be similar to a well environment in field. As technologies progress from the lab to the field, meso-scale experiments combined with the use of calibrated models will provide valuable resources for successful field application [27, 112, 113, 143]. Future meso-scale experimental investigations will study the effects of supercritical $CO_2$ on MICP treated fractures and also study these processes under fully radial flow. These experiments will advance the understanding of impacts of pressure and scale on longevity of the permeability reduction created through MICP.

Not only can the vessel be used for MICP related experiments, but the meso-scale high pressure vessel and system components can be adapted to the study of many subsurface processes.  Several possibilities include, but are not limited to; the study of biologically-induced formation of methane from coal; microbial growth or substrate utilization kinetics under high pressure; microbial community or geochemistry response to supercritical $CO_2$ injection in formations;  methane hydrate investigations; geochemical interactions surrounding hydraulic fracturing; integrity of cement and near well bore environments after exposure to corrosive environments; microbially-induced corrosion or biofouling and many other industry-related processes.

# CHAPTER SIX

# MINERAL SEALS PRODUCED BY MICROBIALLY-INDUCED CALCIUM CARBONATE PRECIPITATION AND THEIR RESISTANCE TO SUPERCRITICAL $CO_2$

## Abstract

Promising results where microbially- or biofilm-induced calcium carbonate precipitation (MICP) has been used to seal fractures under ambient and subsurface relevant conditions have been discussed in the previous chapters of this dissertation. This technology has the potential to improve the storage security of either carbon dioxide or other contaminants stored in the subsurface. The first line of defense to prevent migration is an intact cap rock, which should provide a barrier to flow minimizing upward migration of stored fluids to functional aquifers above. An important concept in the integrity of cap rock is the minimum capillary displacement pressure (MCDP) which can be a measure of the potential for leakage from a cap rock [189]. If biomineralization can reduce permeability and porosity, increase the MCDP, and be resistant to supercritical $CO_2$ exposure, storage security of $CO_2$ in the subsurface could be improved through MICP. Berea sandstone cores (2.54 cm diameter, 5 cm long) were treated using MICP under pressures relevant to the subsurface (75.8 bar, 1100 psi). The permeability and porosity reduction in the cores were attributed to MICP. Data also suggest that the MCDP increases after biomineralization. Exposure of biomineralized cores to $scCO_2$ for 24 hours had no clear impact on the permeability reduction or MCDP.

## Introduction

The potential for geologic carbon dioxide sequestration to become a viable strategy for reducing emissions of $CO_2$ to the atmosphere depends on the risk associated with the technology. One such risk is the potential for leakage of $CO_2$ through the reservoir seal or cap rock [104, 162]. A sufficient sealing efficiency of the cap rock is required to maintain the $CO_2$ in the subsurface, protecting public health from leakage and improving public acceptance of the technology [189-192]. Fine grained rocks with low permeability can act as barriers to flow for extended periods of time if they are not compromised [193].

Flow through the cap rock is one pathway for $CO_2$ to escape and according to Wollenweber et al. in (2010) there are three main risks for leakage (1) rapid catastrophic leakage due to mechanical failure of the cap rock or well casing, (2) seepage of $CO_2$ through faults or fractures, and (3) movement of the $CO_2$ though the pore spaces of the cap rock which is controlled by the capillary pressures and permeability [189]. Darcy's law (Eq 6.1) can be used to calculate the absolute permeability of a single phase fluid flow through a porous media sample [174], where Q/A is the Darcy's velocity (or the volume flux), k is the permeability, $\Delta x$ is the distance, $\Delta P$ is the pressure gradient and $\mu$ is the dynamic viscosity:

$$\frac{Q}{A} = \frac{k\,\Delta P}{\Delta x\,\mu} \qquad (6.1)$$

When measuring permeability, the choice of fluid and flux can influence the result [194]. The differences observed between permeability measured with liquid or gas can be described due the Klinkenberg effect [171]. This difference is related to the slippage of gas in pores enhancing the flow rate through a sample when gas does not adhere to pore walls as well as liquid. The Klinkenberg effect is exacerbated in low permeability samples with small pore throat diameters and at low flow rates, where the permeability of a sample measured with a gas will be higher than that measured with liquid [171, 195]. Tanikawa and Shimamoto (2006) concluded for sedimentary rocks (1) gas permeability can exceed water permeability up to one order of magnitude, and (2) gas and water permeability can increase with increasing pore pressure gradients across the samples. The Klinkenberg equation can be used to estimate the gas or liquid permeability from each other (Eq 6.2) where $k_g$ is the permeability measured by gas, $k_l$ is the permeability measured with liquid, b is a constant which depends on the pore size opening, and p is the pore pressure gradient [171, 194],

$$k_g = k_l\left(1 + \frac{b}{p}\right). \tag{6.2}$$

Fluid transport through a porous sample is also controlled by the interfacial tension of the fluids, the wettability of the sample, and the pore structure and pore throat radius [174, 193]. The capillary pressure ($P_c$) is the pressure difference between the nonwetting ($P_2$) and wetting fluids ($P_1$) within a pore. Here, the wetting fluid is described as the fluid that has initially saturated the porous media sample and the nonwetting fluid is the fluid which displaces the wetting fluid. The pore throat radius can be estimated using the Washburn Equation (Eq 6.3), where $P_c$ represents the capillary pressure, $r$ represents the ideal cylindrical radius of the pore throat, $\gamma$ is the interfacial tension and $\theta$ is the wetting angle of the fluid relative to the surface of the sample.

$$P_c = P_2 - P_1 = \frac{-2\gamma\cos\theta}{r} \tag{6.3}$$

The sealing efficiency of a porous medium or a cap rock can be determined experimentally by injecting a nonwetting fluid (i.e. $CO_2$, supercritical $CO_2$, or nitrogen) into a water (or brine) saturated rock core. If a constant pressure is maintained at the core entrance, the pressure at the outlet will equilibrate, resulting in a pressure differential ("delta P") across the core which does not change with time (under this condition there is no flow of the non-wetting fluid through the core). This "delta P" is defined as the Minimum Capillary Displacement Pressure (MCDP) and corresponds to incipient breakthrough of the non-wetting fluid [174]. Any increase in delta P above the MCDP will result in non-wetting fluid beginning to flow through the core. In the context of $CO_2$ leakage potential, the MCDP can be interpreted as the point when $CO_2$ reservoir pressure exceeds the capillary pressure of a water saturated pore network in the cap rock and upward migration of $CO_2$ begins [189].

Biomineralization via the precipitation of calcium carbonate by urea hydrolysis has been suggested and researched as a method to reduce permeability in subsurface fractures and porous materials [2, 4-7, 196]. However several questions about the applicability of the technology in the subsurface remain. Accordingly, the primary goals of the research described in this chapter were to advance understanding of how MICP promoted under high pressure conditions might improve MCDP in sandstone cores, assess which aperture pore throats were most impacted by MICP, and study the impact of $scCO_2$ on the biomineral sealing capability. Toward these goals, we (1) biomineralized cores under subsurface relevant pressures to reduce permeability, (2) subjected biomineralized and non-mineralized samples as "control cores" to mercury intrusion porosimetry (MIP) to determine the aperture of pores throats most impacted by MICP, (3) subjected biomineralized and control cores to $scCO_2$, and (4) assessed the minimum capillary displacement pressure of mineralized and control core samples.

## Materials and Methods

### Biomineralization

High Pressure System. A high pressure testing system was designed and constructed to house 2.5 cm diameter, 2.5-15.2 cm long cylindrical cores (Figure 6.1 and 6.2). The high pressure test system was equipped with a biaxial Hassler type core holder (Temco, TX, USA) with a hydraulic jack pump (Enerpac, WI, USA) used to provide overburden pressure, and a dual set of Teledyne Isco (Teledyne, Lincoln, NE, USA) pumps to deliver fluids to the core holder. In experiment #1 a piston-type accumulator (Parker, IL, USA) was used to control the back pressure. In experiment #2 and #3 one of the Isco pumps was operated in constant pressure mode to provide the desired back pressure. The system was equipped with two pressure relief valves set to 124 bar (Swagelok, ID, USA) and pump pressure cutoff set points were set as redundant safety measures. Overall system pressures and flows were measured with the Teledyne Isco pumps and differential pressure was verified with a pressure transducer (Omega, CT, USA).

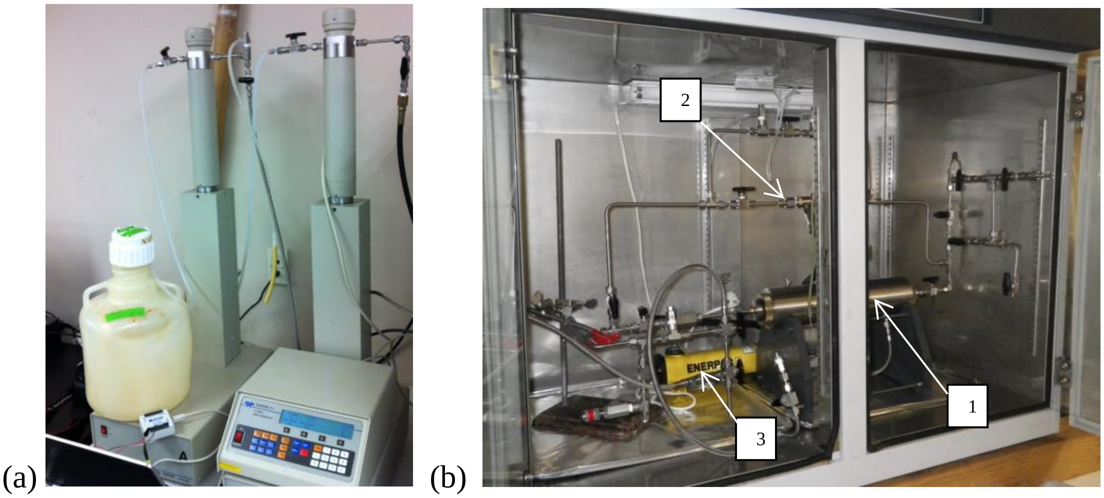

Figure 6.1. High pressure system for testing 2.5 cm diameter cores. (a) Dual Teledyne Isco pumps, generally one pump served as the delivery pump and the other operated as the back pressure regulator. (b) Hassler-type biaxial core holder (1) Omega differential pressure transducer (2) and hydraulic jack pump (3) used to provide overburden pressure. The system was housed in an incubator to allow for temperature control.

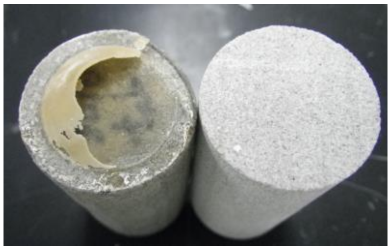

Figure 6.2. Berea sandstone 2.5 cm diameter, 5 cm long cores before (right) and after (left) biomineralization.

All the Berea sandstone cores described in this chapter were drilled from a block of sandstone acquired from Cleveland Quarries (Vermilion, OH, USA). The cores were drilled with water using a diamond drill bit (MK Diamond Products, CA, USA) to 2.54 cm diameter and greater than 5 cm in length. The cores were then cut to 5 cm length using a tile saw (MK Diamond Products, CA, USA). The core samples were loaded into the core holder’s Viton sleeve and the core holder was threaded closed prior to filling the annular space with antifreeze fluid. The use of antifreeze serves to minimize corrosion in the hydraulic jack pump. The overburden fluid was pressurized to above the targeted system delivery and back pressure set points.

Saturation, Bypass and Overburden Pressure Analysis. Before each biomineralization experiment commenced, each sample and the control core were saturated by flowing at least 100 pore volumes of phosphate buffer solution (PBS) or 10 g/L $NH_4Cl$ solution through the core and letting the core condition overnight. Next, the overburden pressure was determined at which fluids would bypass the core or create a back flow condition (flow into annular space between core sleeve and Hassler body) instead of flowing through the core. Additionally, the potential impact of increasing overburden pressure to core permeability was assessed. Using constant flow through the core, and monitoring the differential pressure, the overburden pressure was lowered incrementally from 17.2, to 13.8, 6.9, 3.4, 1.7, 0.7 and finally to 0 bar. The differential pressure was monitored and when an abrupt reduction in differential pressure was noted, it was taken as an indication that bypass or backflow was occurring. Subsequently, the overburden pressure was raised above the bypass or backflow pressure and stepwise increased from 3.4, 6.9, 13.8 and 20.7 bar to determine whether overburden pressure exhibited an influence on the observed permeability.

Biomineralization Procedure. *Disinfection.* Each of the following solutions were run through the pumps and system but not the core, in the following order: (1) a solution of 5mL bleach and 3.5 g Tween 80 dissolved into 500 ml deionized water ($dH_2O$), (2) 500 ml of autoclaved $dH_2O$, (3) an autoclaved solution of 1.26 g sodium thiosulfate dissolved into 500 mL $dH_2O$, (4) a 0.2 μm filter sterilized (Thermo Scientific, NJ, USA) 70% ethanol solution and (5) 500 ml of autoclaved PBS in $dH_2O$ [169].

*Inoculation.* A culture was prepared by inoculating 100 mL of brain heart infusion amended with urea (20 g/L) with 100 μl of a thawed frozen stock culture of *S. pasteurii* (ATCC 11859). The culture was shaken at 30°C at 150 rpm for approximately 16 hours to stationary phase. The culture was centrifuged at a relative centrifugal force (RCF) of 2964 x g for 10 minutes at 4-6° C and the cells were re-suspended in ~50 mL of fresh medium. Triplicate samples of 200 μL of the culture were aliquoted to a 96 well microplate (Corning, NY, USA) and the optical density read at 600 nm ($OD_{600}$) with BioTek Instruments' (Winooski, VT, USA) Synergy HT Multi-Mode Microplate Reader. The observed $OD_{600}$ was 0.4. One ml of the culture was removed to determine the concentration of cells and the rest reserved for inoculating the core. The inoculum was serially diluted in PBS and drop-plated [164] on BHI agar plates containing 20g/L urea. The plate(s) were incubated at 30°C and counted after 24 hours to determine cell concentration in cfu/ml.

To prepare the core for inoculation, one pore volume (~5 ml) of filter sterilized urea growth medium was pumped into the core, then 20 ml of the diluted inoculum were pumped into the core at 5 ml/min. The cells were allowed to attach in the core under no flow conditions for four hours.

*Biofilm Growth.* Following the attachment period, biofilm growth was promoted. In the first experiment, the overall system pressure was increased gradually over the course of the biofilm growth stage (9 hours) to acclimate the biofilm to elevated pressures. In the next two experiments as soon as the attachment period was over the system pressure was increased rapidly (~3 minutes) to the desired pressure (Table 6.1). During the biofilm growth stage the urea growth medium was pumped through the cores at 5 ml/min. The length of time the urea growth medium was injected varied for each experiment as detailed in Table 6.1. Although not measured or confirmed, it was assumed that all of the solutions injected behaved in a plug-flow manner through the system. No effort was made to control temperature of the incubator; all experiments were performed at room temperature (approximately 22°C).

*Calcium and Resuscitation Pulses.* After the biofilm growth stage, calcium pulses were initiated and regular resuscitation events were performed (Table 6.1).

Table 6.1 Experimental parameters of biomineralization.

| Exp # | Downstream pressure (bar) | Calcium injected (g) | Biofilm growth (hr) | Calcium pulses | Max $\Delta p$ (bar) | Experimental goals |
|---|---|---|---|---|---|---|
| 1 | 72.4 | 1.23 | 9 | 20 | 10.3 | Reached 2 order of magnitude reduction in permeability |
| 2 | 75.8 | 1.72 | 6 | 38 | 10.3 | Same permeability as exp. #1 |
| 3 | 75.8 | 0.42 | 16 | 7 | 124 | Reached system pressure limit |
| Control | Ambient | N/A | N/A | N/A | 2.2 | Control core not mineralized |

Calcium pulses were performed as follows:

1. At least two pore volumes of Saturation reducing medium (also known as CMM= (minus minus)) (Table 6.2) were injected,
2. At least two pore volumes of Calcium medium (also known as CMM+) (Table 6.2) were injected,

3. Saturation reducing medium was used to theoretically displace the first 1/5 of the core,
4. Flow was stopped for 4 hours to allow for ureolysis and calcium precipitation to occur.

Resuscitation pulses were performed as follows:

1. At least two pore volumes of Urea growth medium (also known as CMM-) (Table 6.2) were injected,
2. Flow was stopped for 1 hour to allow time for ureolysis to occur.

Table 6.2 Media recipes (in g/L)

| | Saturation Reducing Medium (CMM=) | Calcium Medium (CMM+) | Urea Growth Medium (CMM-) |
|---|---|---|---|
| Urea (Fisher, NJ, USA) | -- | 20 | 20 |
| Nutrient Broth (BD, NJ USA) | 3 | 3 | 3 |
| Calcium chloride dihydrate (Acros, NJ, USA) | -- | 49 | -- |
| Ammonium chloride (Fisher, NJ, USA) | 10 | 10 | 10 |

*Experimental Termination.* Each of the three experiments was terminated by depressurizing the system, removing the core from the Hassler-type core holder and placing the core in a glass beaker to dry. To assess the permeability along the flow path of the core, biomineralized core #1 was cut in half, and either the influent half or effluent half was reloaded into the core holder, re-saturated and the permeability was tested by injecting PBS solution and monitoring the flow rate and differential pressure. This was done to determine whether one half of the core contributed more to the permeability reduction than the other half. These half pieces were removed from the core holder and were further cut into four pieces along the length of the flow path, the influent 0.32 cm, the middle influent half and middle effluent half and then the effluent 0.32 cm (Figure

6.3). The middle influent half or middle effluent half without their first or last 0.32 cm were individually loaded into the core holder and re-saturated. Their permeability was measured to assess the influence of the "skin" of calcium carbonate which had formed on the influent and effluent core and bulk fluid interfaces on the permeability.

A control core was cut in half as well. The control core halves were loaded individually into the core holder to assess whether any artifacts to permeability were introduced by cutting the cores.

Figure 6.3. Mineralized core cut into four pieces (from left to right: inlet "skin"-first 0.32 cm; middle influent, middle effluent, outlet "skin"-last 0.32cm) to assess the impact to permeability reduction by the "skin" formed on the influent and effluent.

Biomineralized cores #2 and #3 remained intact and were shipped (along with unmineralized controls) to Dr. Peter Walsh at the University of Alabama-Birmingham for minimum capillary displacement pressure testing and $scCO_2$ exposure (details below). The cores were tested and shipped back to Montana State University for additional analysis such as cutting into sections to assess permeability along the length and mercury intrusion porosimetry (planned, but not yet conducted).

### Mercury Intrusion Porosimetry (MIP)

Collaborators at the University of Montana, Montana Tech's Center for Advanced Mineral and Metallurgical Processing (Butte, Montana, USA) subjected triplicate samples of biomineralized core #1 and an unmineralized control to mercury intrusion porosimetry (Micromeritics AutoPore IV 9500 Series, GA, USA). Samples were dried until no change in mass was observed from day to day and samples were subjected to mercury intrusion porosimetry (MIP). In MIP, mercury is intruded into the sample by increasing pressure. The Washburn equation (eq. 6.2) describes the pressure required to force a non-wetting liquid (mercury) to enter a capillary of circular cross-section. The pressure is inversely proportional to the radius of the capillary (or pore throat) and directly proportional to the surface tension of the liquid and the angle of contact with the solid surface [197]. Additionally, the volume of mercury intruded into the pores provides a measurement of the porosity of the sample.

### Microscopy

Samples of core #1 were imaged using the Zeiss Supra 55VP scanning electron microscope (SEM) located in the Imaging and Chemical Analysis Laboratory (ICAL) at Montana State University (MSU) and with the Nikon Stereoscope located in the Center for Biofilm Engineering (CBE) Microscopy Center. For SEM, the core samples were air-dried and sputter coated with iridium. High-resolution images were taken at 1.0 kV at a working distance of ~4.0 mm. Elemental analyses with energy-dispersive X-ray spectroscopy (EDS) were performed at 20 kV and a working distance of 15 mm. Portions of each section of core #1 and the control were also sent to collaborator Dr. Bruce Fouke, (University of Illinois Urbana-Champaign) for thin section analysis.

### Permeability, Porosity and Minimum Capillary Displacement Pressure

Collaborator, Dr. Peter Walsh at University of Alabama-Birmingham performed the following steps to determine the permeability, porosity and MCDP of the biomineralized and control cores. First, the cores were weighed as received and dried to constant weight at 50°C. The permeability (adjusted for the Klinkenberg effect) was measured with flowing nitrogen. The cores were saturated with brine to determine porosity from dry and saturated weights. The MCDP was measured and the cores were re-saturated with brine. Next, the cores were challenged with supercritical $CO_2$ (50°C, 82.7 to 89.6 bar) for 24 hours. After $CO_2$ exposure, the cores were re-saturated with brine and their MCDP was re-measured. Finally the cores were dried and the permeability corrected for the Klinkenberg effect was re-measured with nitrogen. Additional details about these steps are provided in the specific sections below.

$N_2$/Brine to Assess Permeability and MCDP. Nitrogen was first used to measure permeability of the cores by flowing $N_2$ constantly through the cores held in a Core Lab/TEMCO triaxial core holder (Figure 6.4) at room temperature (22.0 to 22.5°C) and at pressures of 4.1 to 13.8 bar on the upstream face of the core. The pressure drop was controlled using a metering valve at the outlet from the core holder. The flow rate of gas through the sample was determined by timing the displacement of a soap film in a graduated tube (Teledyne Hastings Mini-Flo Calibrator, Model HBM-1A). Overburden pressure, both axial and radial, was 137.9 bar. The flow and differential pressure were used to calculate the permeability with correction for the Klinkenberg effect [171].

The minimum capillary displacement pressures were determined by saturating the cores with brine (10 g NaCl/L) and using nitrogen at ambient temperature (20.6 to 21.8$^{o}$C) to displace the brine in cores housed in the triaxial core holder with an overburden pressure of 137.9 bar (Figure 6.4). The MCDP was measured by imposing a pressure difference greater than the breakthrough pressure across the brine-saturated sample, then letting the upstream pressure fall and the downstream pressure rise to their asymptotic values [174, 193]. The residual pressure difference between the influent and effluent side of the core at equilibrium was determined as the MCDP.

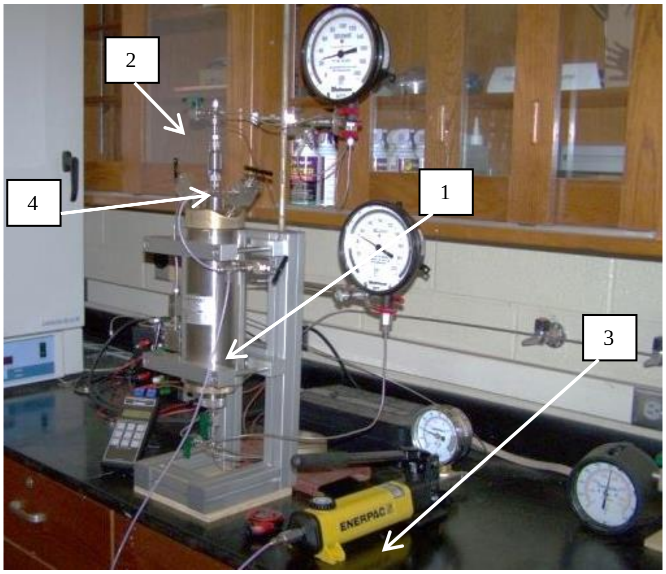

Figure 6.4. Set-up of the triaxial core holder (1) with effluent valve (2), hydraulic jack pump to provide overburden pressure (3), and effluent sample cylinder (4) for measurement of MCDP and subjecting samples to $scCO_2$.

<u>Supercritical Carbon Dioxide ($scCO_2$) Exposure.</u> Following measurement of the MCDP, the core was re-saturated with pressurized (106.2 bar) brine and the excess brine was removed from the sample cylinder (Figure 6.4). Following saturation, the gas lines

and pressure gauges were purged with $CO_2$, the core holder was placed in the oven, and the oven and core holder were heated overnight to 50$^{o}$C.

To challenge the cores with supercritical ($scCO_2$), both the upstream and downstream sides of the core were pressurized to 82 bar, and the influent pressure was raised to a constant pressure of 95.8 bar. When the pressures equilibrated, the system was shut in and the cores were subjected to 24 hours of $scCO_2$ exposure prior to re-drying at 50°C. After drying, the MCDP and permeability with nitrogen were re-measured as described above. Cores were then shipped back to Montana State University where they are currently undergoing additional analysis.

### X-Ray Computerized Tomography (CT)

A SkyScan 1173 Micro-CT scanner was used to scan sandstone cores before and after biomineralization and after exposure to $scCO_2$ (Appendix H).

## Results and Discussion

Note: the results and discussion presented in this section are work in progress.

### Biomineralization

#### Bypass or Backflow Pressure.

To confirm that the injected fluids were pumped through the core and not around it or around the sleeve into the annular space (i.e. bypass), the overburden pressure was decreased in increments and the differential pressure ($\Delta P$) was monitored (Table 6.3). At two different flow rates (1.5 and 5 ml/min) the overburden pressure was decreased step-wise and it was determined that as long as the overburden pressure was at least 1.7 bar greater than the differential pressure bypass or backflow was not occurring. At all times during the further experimentation, the overburden pressure was maintained at pressures greater than 1.7 bar above the applied differential pressure.

Table 6.3. Decreasing overburden pressure (P) to determine bypass or backflow (B) around the core.

| Flow Rate (ml/min) | ΔP (bar) | Permeability (mD) | Overburden P (bar) | Comments |
|---|---|---|---|---|
| 1.5 | 12.7 | 28.6 | 17.2 | |
| 1.5 | 12.9 | 28.1 | 13.8 | |
| 1.5 | 13.1 | 27.7 | 10.3 | |
| 1.5 | 13 | 27.9 | 6.9 | |
| 1.5 | 13.6 | 26.7 | 3.4 | |
| 1.5 | 15.1 | 24.0 | 1.7 | |
| 1.5 | 12.4 | 29.2 | 0.7 | |
| 1.5 | 4.7 | 77.2 | 0 | B |
| 5 | 53 | 22.8 | 6.4 | |
| 5 | 60 | 20.1 | 5.2 | |
| 5 | 59 | 20.5 | 3.4 | |
| 5 | 32 | 37.8 | 1.7 | POSSIBLE B |
| 5 | 8.8 | 137.4 | 0.7 | B |
| 5 | 0.2 | 6045.7 | 0 | B |

Impact on Permeability from Overburden Pressure. The overburden pressure was incrementally increased to assess the impact to the core permeability (Figure 6.5). No statistically significant impact of increasing overburden pressure on the measured permeability was observed.

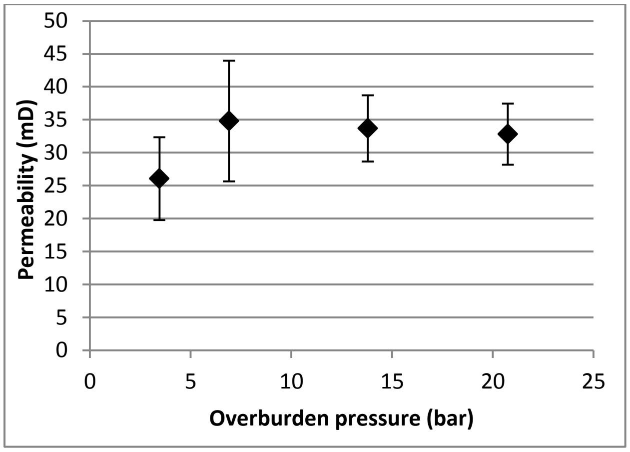

Figure 6.5. Impact of increasing overburden pressure on Berea sandstone core permeability. Overburden pressure in the Hassler-type core holder did not significantly impact the measured permeability through an unmineralized control core. The average measured permeability of the Berea Sandstone was 31 mD ± 5.6 mD.

Permeability Reduction Due to Biofilm Growth. Growth of the biofilm impacted the permeability in each of the Berea sandstone cores (Table 6.4). The length of the biofilm growth stage positively correlated with the permeability reduction. After 6 hours of biofilm growth the permeability was reduced by 49%, after 9 hours of biofilm growth the permeability was reduced 80%, and after 16 hours of biofilm growth the permeability was reduced 95%.

Table 6.4. Permeability of the cores prior to biofilm growth and after.

| Exp. # | Biofilm growth stage (hr) | Initial permeability (mD) | Permeability after biofilm growth (mD) |
|---|---|---|---|
| 1 | 9 | 37 | 7.3 |
| 2 | 6 | 37.6 | 19.1 |
| 3 | 16 | 34 | 1.7 |

Additional Permeability Reduction Due to MICP. After calcium and resuscitation pulses, the overall permeability of the mineralized cores was reduced (Figure 6.6 and Table 6.5). Permeability was reduced to 0.2 mD in core #1, 0.3 mD in core #2, and 0.02

mD in core #3. In experiment #1 and #2, little permeability reduction was achieved after the initial permeability reduction due to biofilm growth until reaching calcium pulses 18 of 21 in experiment #1 and 32 of 35 in experiment #2. These calcium pulse points correspond to permeabilities between 8 and 11 mD. One hypothesis to explain this behavior is there may be a critical permeability ($k_{crit}$) which may be correlated to a critical porosity where MICP treatment can more easily impact the permeability reduction.

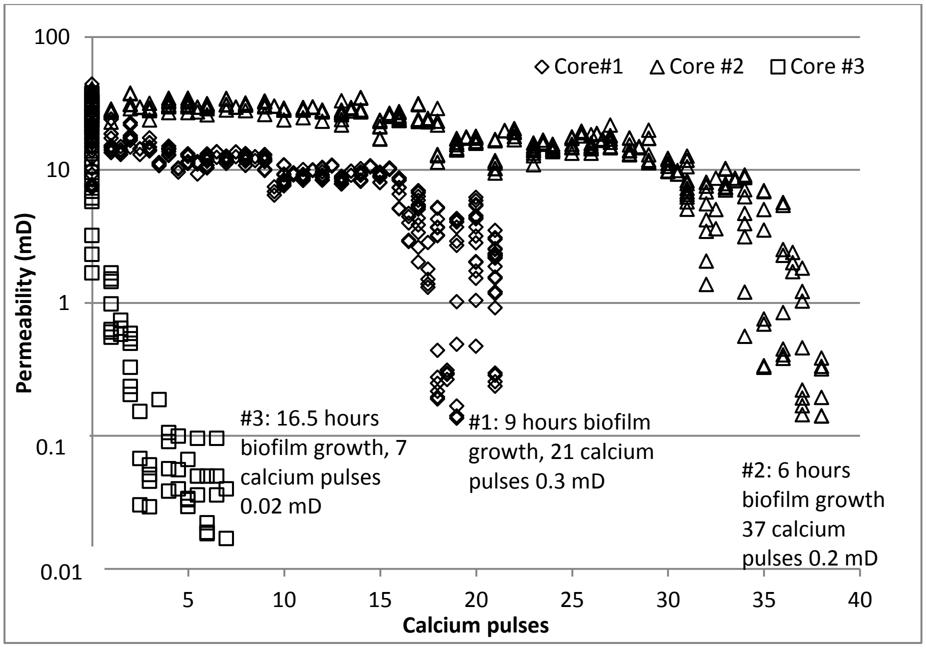

Figure 6.6. Permeability reduction in biomineralized cores. Permeability was significantly reduced both by the biofilm growth stage and the biomineralization treatment in each of the cores subjected to biomineralization treatment. Permeability of Core #1 was reduced to 0.2 mD after 9 hours of biofilm growth and 21 calcium pulses. Permeability in Core #2 was reduced to 0.3 mD after 6 hours of biofilm growth and 37 calcium pulses and the permeability of Core #3 was reduced to 0.02 mD after 16.5 hours of biofilm growth and 7 calcium pulses.

Table 6.5. Summary of permeability, porosity and MCDP of biomineralized cores and an unmineralized control core. NM= not yet measured. N/A= not applicable.

| Exp. # | Initial Perm. (mD) | Perm. before sent to UAB (mD) | Porosity | Perm. with $N_2$ at UAB (mD) | MCDP (bar) | 24 hr $scCO_2$ | Perm. after $scCO_2$ at UAB (mD) | MCDP after $scCO_2$ (bar) |
|---|---|---|---|---|---|---|---|---|
| 1 | 37 | 0.2 | 14.9% | N/A | | | | |
| 2 | 37.6 | 0.2 | NM | 5.7±3.4 | 0.255 | Yes | 4.27±0.1 | NM |
| 3 | 34 | 0.02 | 14.5% | 0.011±0.06 | 0.8± 0.1 | Yes | NM | 0.5 ± 0.2 |
| Controls (2) | 27, 30 | N/A | 18.9% | 71.6±0.8 | 0.007 | No | NM | NM |

Contribution to Permeability by Influent and Effluent "Skin". After the termination of the experiment, particularly for core #1, it was noted that a "skin" of biomineral had formed on the influent and effluent regions of the core (Figure 6.7).

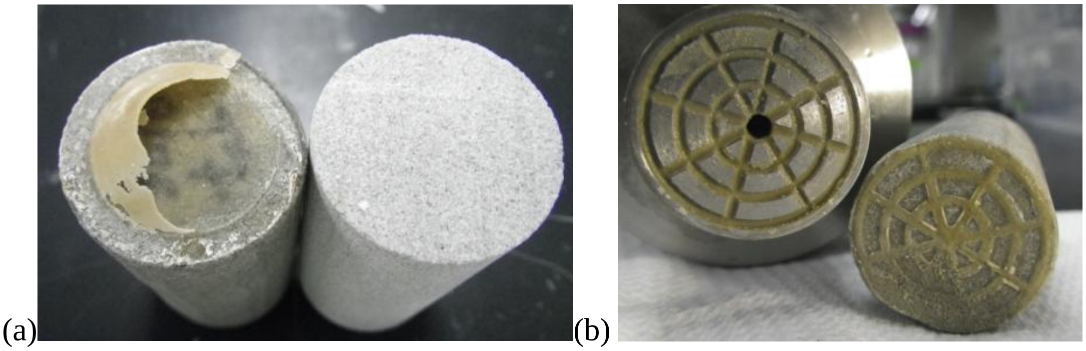

Figure 6.7. Influent and effluent regions of mineralized cores. (a) Mineralized core (left) influent region compared to unmineralized core (right). Note the "skin" of calcium carbonate formed on the influent region of the mineralized core which corresponds to the region of bulk fluid to core interface. (b) Effluent region of a biomineralized core exhibiting a similar pattern of calcium carbonate "skin" in a configuration similar to the core holder's effluent pattern.

First, it was observed that the permeability of core #1 had changed after drying. At the end of the experiment, the permeability had been 0.2 mD, but when it was reassessed it measured 2.4 ± 2.4 mD. This could be due to mineral drying and cracking or some other phenomena associated with the drying of the core. The impact of core drying to permeability has not yet been assessed. The core was cut in half and the permeability of the influent half of the core was determined to be 1.4 ± 1.9 mD and the permeability of the effluent half was 1.9 ± 2.6 mD. Upon removing the "skin" along with 0.3 cm from the influent and effluent portions of the core, the permeability was measured to be 8.1 ± 2.4 mD and 3.6 ± 0.5 mD for the influent and effluent sections, respectively (Table 6.6). The permeability in the influent portion of the core was higher than the effluent portion after the "skin" was removed. The unmineralized control core had a permeability of 30 mD and when it was cut in half the permeability statistically remained the same for influent and effluent portions of the control core.

Table 6.6. Permeability of the mineralized core #1 cut in half with and without the skin portion as compared to an unmineralized core.

| Core | Permeability (mD) | |
|---|---|---|
| Control whole | 30 ± 4.9 | |
| Cut in half | Influent: 29 ± 6.9 | Effluent: 30.4 ± 2.9 |
| Biomineralized whole | 0.2 end of experiment & 2.4 ± 2.4 retesting after drying | |
| Cut in half with skin | Influent: 1.4 ± 1.9 | Effluent: 1.9 ± 2.6 |
| Cut in half without skin | Influent: 8.1 ± 2.4 | Effluent: 3.6 ± 0.5 |

These preliminary results suggest that permeability reduction is being achieved by both the contribution of biofilm growth and MICP treatment. The experiment #3 was limited by a differential pressure of 124 bar due to the system's pressure limits and as such the lowest permeability achieved in these core samples was limited by constraints of the system. The "skin" observed on the influent and effluent regions of core #1 influenced the reduction in permeability, more in the influent region than in the effluent region of the core.

Mercury Intrusion Porosimetry (MIP)

The unmineralized control core, had an average porosity of 18.9% ± 0.5% (n=3). The influent region of biomineralized core #1 had a porosity of 14.9% ± 0.8% and the effluent portion had a porosity of 10.7% ± 0.3% (both n=3). In core #1, a greater reduction in porosity was observed in the effluent portion of the core compared to the influent portion.

It was also determined that the pore size distribution was impacted by biomineralization (Table 6.7). In the control core, over 50% of the pore volume was associated with pores sizes between 6 and 16 µm but after mineralization this number decreased to just over 30%.

Table 6.7. Fraction of pores in the core sample subjected to MIP which fall into each size range before and after mineralization in samples from the influent region and effluent region of the biomineralized core #1.

| Pore diameter | Control average | Biomin Influent Average | Biomin Effluent Average |
|---|---|---|---|
| less than 1 µm | 15% | 22% | 28% |
| 1-10 µm | 33% | 26% | 38% |
| 10-100 µm | 42% | 29% | 22% |
| 100-1000 µm | 10% | 23% | 13% |
| 6-16 µm | 51% | 33% | 31% |

The pore throat size range most impacted by biomineralization in these Berea sandstone cores were those with pore throat diameters ranging from 6-16 µm. Before mineralization 51% of the pores fell in the range of 6-16 µm, but after MICP treatment only 31-33% of the pores had that range of diameters. Also, before mineralization the fraction of pores with pore throat diameters less than 1 µm was 15% but that number increased in the biomineralized core to 22% in the influent portion and 28% in the effluent portion. This suggests a shift in the pore size distribution from the 6-16 μm range pore throat diameter range toward smaller pore throats after mineralization. It should be noted that absolute conclusions about this data cannot be drawn as this analysis has only been performed on one control and one biomineralized core. Additional experimentation and analysis is required.

### Microscopy

Visualization via stereomicroscopy and SEM revealed the presence of a layered mineral formed at the base of the calcite “skin”, here taken to mean the layer of calcium carbonate which formed on the influent region of the MICP treated core #1 (Figure 6.8). Further magnification via scanning electron microscopy reveals the presence of cell-like structures inside layers of minerals. It is possible that these layers are formed due to the injection strategy of pulsed flow alternating calcium and growth medium. It is hypothesized that during the injection of the calcium medium more solid layers of minerals were formed, and then during the injection of the growth medium a layer of biomass could have formed where the cell-like structures are found. As stated previously, additional analysis on several samples would be required to draw more reliable conclusions.

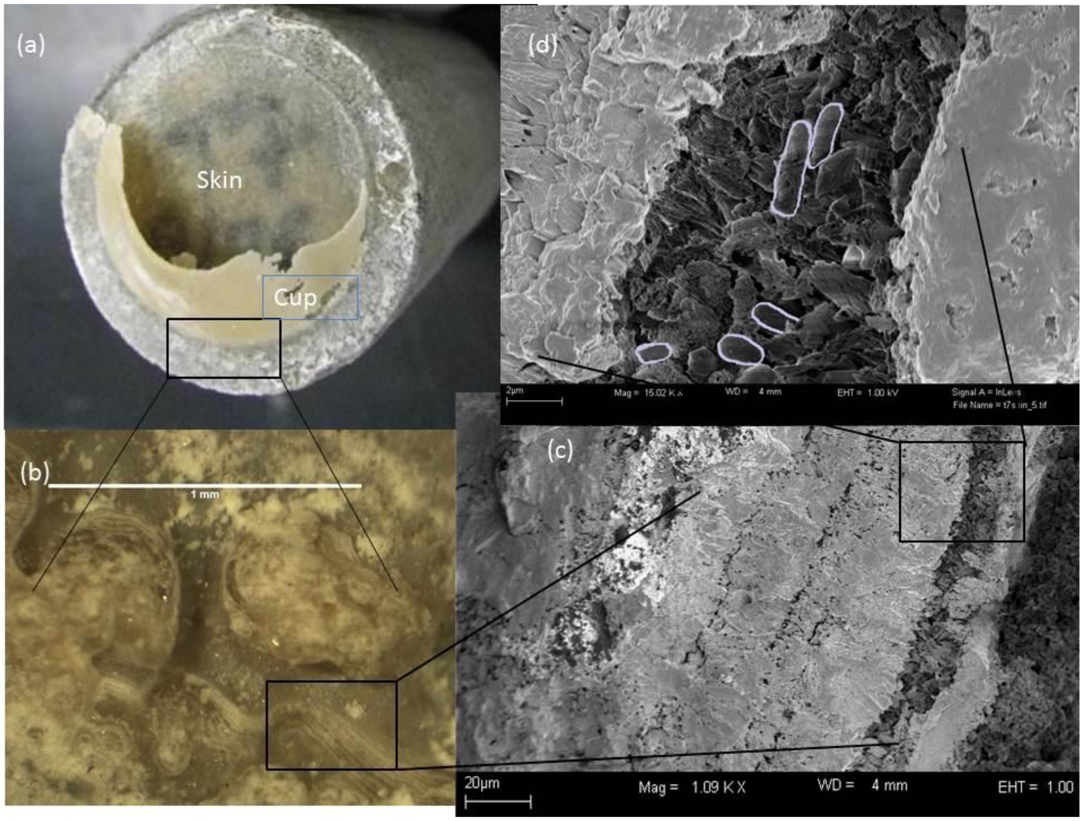

Figure 6.8. Images of the influent side of biomineralized core #1. (a) Photo of the calcium carbonate “skin” and calcite “cup” formed on the influent of the core where the bulk fluid interface exists in the core holder (b) stereoscope image of the layers of mineral observed in the bottom portion of the calcite cup where the skin and cup meet (scale bar 1 mm) (c) further magnification of the layered area with SEM (scale bar 20 μm) and (d) even further magnification (scale bar 2 μm) into one of the layers where cells (falsely colored in purple outline for emphasis) were observed associated with calcium containing minerals.

On-going collaboration with Dr. Bruce Fouke at the University of Illinois Urbana-Champaign is occurring with the intent of deciphering the biogenic role of the microbes on the mineralization patterns through thin-section analysis. One preliminary result of this collaboration is the identification of “fuzzy dumbbells” (Figure 6.9), thought to be the result of mineral encasement of microbes in calcium containing mineral which primarily form in the bulk fluid solid substratum interface (Fouke, Personal Communication, May 2013).

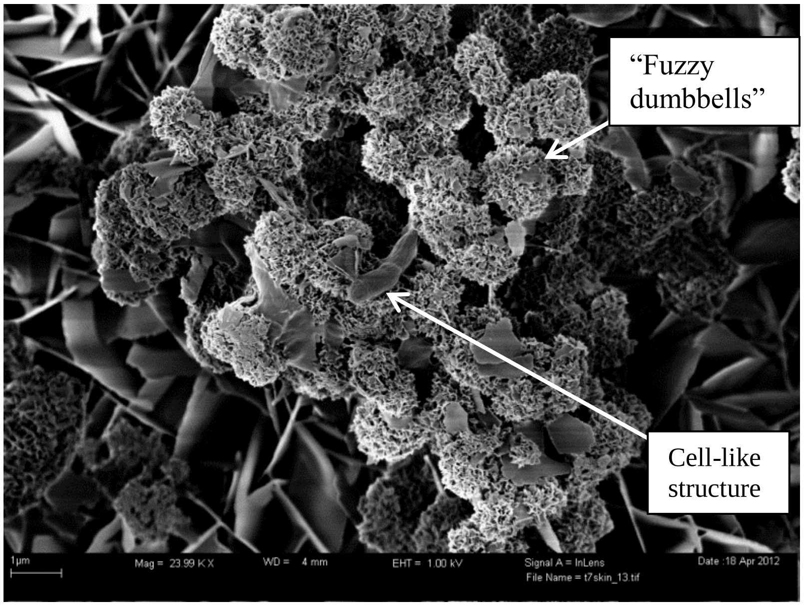

Figure 6.9. Images of cell-shaped "fuzzy dumbbells" thought to be cells encased in the calcium mineral as it nucleates.

## Minimum Capillary Displacement Pressure (MCDP)

### $N_2$-Brine to Determine MCDP.

Three cores thus far have been subjected to brine saturation and $N_2$ displacement to determine the MCDP, biomineralized cores #2 and #3 and one unmineralized control core. In the case of cores #2 and #3 it was observed that biomineralization reduced measured permeability and increased the MCDP compared to the unmineralized control core (Table 6.5).

For the control and core mineralized during experiment #2, the measured permeability using $N_2$ at UAB was 71.6 ± 0.8 mD (unmineralized control core) and 5.7 ± 3.4 mD (mineralized sample), respectively. The permeability measurement of biomineralized core #2 performed at UAB differs from the measurement achieved right at the end of the experiment (0.3 mD) at MSU possibly due to the process of drying and re-saturating the core between measurements. The permeability of the control core was measured to be 30 mD at MSU while UAB measured 71.6 mD. UAB applied the correction for the Klinkenberg effect [171] since their measurements were performed with nitrogen and the measurements at MSU were performed with phosphate buffer or $NH_4Cl$ solutions, however there still exists a difference between the MSU and UAB measurements. These differences are not completely understood, although, differences in saturation might account for the discrepancies. The permeability of core #3 measured 0.02 mD and 0.011 mD at MSU and UAB, respectively, which are more comparable than the permeability measurements of core #2 and the control core.

When subjected to $N_2$/brine MCDP measurements, (Figures 6.10. a, b, and c.) the control core measured 0.007 bar (0.1 psi), the biomineralized core #2 measured 0.255 bar (3.7 psi) and the biomineralized core #3 measured 0.8 bar ± 0.1 bar (11.6 psi ± 1.7 psi, n=3). The uncertainty in the measurements was approximately 0.007 bar (0.1 psi). The MCDP of the control and biomineralized core #2 were measured once, whereas biomineralized core #3 was measured three times. The MCDP of biomineralized core #3 was observed to increase between trials from 0.7 bar (10.1 psi) to 0.8 bar (11.4 psi) and 0.9 bar (13.4 psi). The average MCDP from the three measurements was 0.8 bar ± 0.1 bar (11.6 ± 1.7 psi).

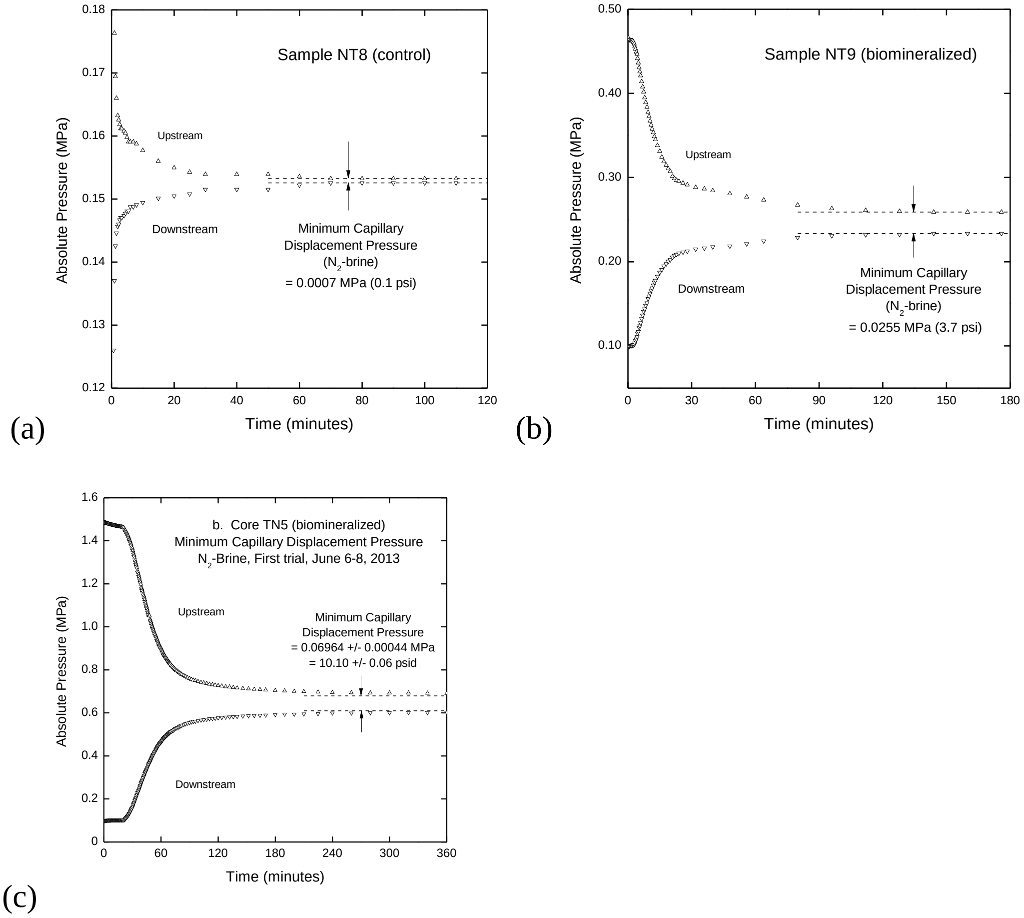

Figure 6.10. Upstream and downstream pressures versus time to determine MCDP for the (a) unmineralized control core, (b) biomineralized core #2, and (c) the first of three trials of biomineralized core #3. The measured MCDPs for the control core were 0.007 bar (0.1 psi), biomineralized core # 2 was 0.225 bar (3.7 psi), and biomineralized core #3 was 0.8 bar (11.6 psi, n=3).

Porosity was observed to decrease slightly in the biomineralized cores compared to the unmineralized control core (14.9, and 14.7% compared to 18.9%). For core #3, the absolute permeability was determined to be 0.01 mD and its porosity 14.5% (Table 6.5). Compared to the control, the MCDP increased as the permeability decreased in both the experimental cores (Figure 6.11).

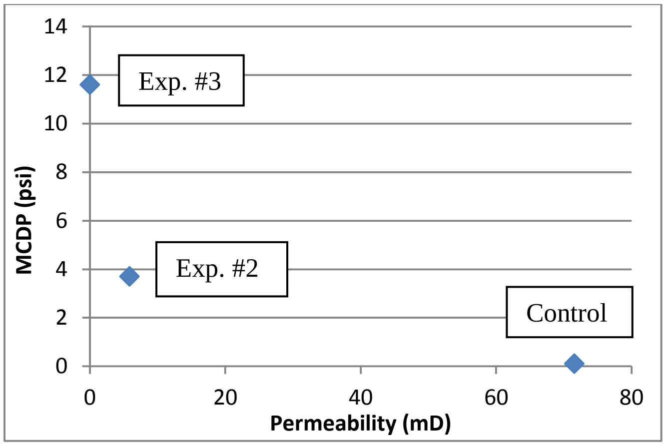

Figure 6.11. Minimum capillary displacement pressure compared to permeability in mineralized cores #2 and #3 and an unmineralized control core. MCDP was observed to increase with decreasing permeability.

$\underline{\text{scCO}_2\text{ Exposure.}}$ The exposure of the core #2 to $scCO_2$ revealed no statistically significant influence on the permeability (Table 6.5). The control core has not yet been subjected to supercritical $CO_2$ exposure. The mineralized core #3 was also exposed to $scCO_2$ for 24 hours. The permeability of core #3 has not yet been determined after exposure to $CO_2$. The MCDP after $scCO_2$ exposure in core #3 was measured four times and statistically did not change (0.5 ± 0.2 bar) after exposure compared to (0.8 ± 0.1 bar) before exposure. The first trial out of the four in core #3 revealed an unusually low MCDP value (0.2 bar) and was not included in the average after exposure MCPD calculation as it was attributed to incomplete saturation of the core prior to MCDP measurement. Additional measurements are being performed to determine the impact of exposure to $scCO_2$.

## Conclusions and Future Work

Biofilm growth and MICP treatment promoted in 2.5 cm diameter, 5 cm long Berea sandstone cores influenced a decrease in permeability. The maximum reduction in permeability due to biomineralization was limited by the system's differential pressure limits of 124 bar. MICP treatment of core #3 resulted in a three order of magnitude reduction in permeability. Two orders of magnitude reduction in permeability were achieved in cores #2 and #3. The minimum capillary displacement pressures of mineralized cores were 36 and more than 100 times higher (0.25 bar and 0.8 bar) for cores #2 and #3, compared to the unmineralized control core (0.007 bar). This suggests that the permeability reduction influenced by biomineralization also increases the MCDP significantly compared to controls. It was observed that 24 hours of $scCO_2$ exposure did not significantly impact the permeability or MCDP. Reducing permeability, increasing MCDP and maintaining the reduced MCDP after $scCO_2$ exposure all suggest promise toward using MICP under high pressure conditions to improve the security of geologically stored $scCO_2$.

As this technology transitions from the laboratory to the field, it may be important to understand in more detail the impact of biofilm growth to the success of the treatment. For example, it would be advantageous to understand how the biofilm forms a template for the mineral to initiate and precipitate and whether that leads to more porous or less dense mineral. Also, understanding how the length of the biofilm growth stage influences the number of calcium injections necessary to reduce permeability could help improve field injection strategies to promote shorter field application times. Preliminary data suggests that the pore sizes most influenced by biomineralization are those in the size range of 6-16 μm. Since microbes such as *S. pasteurii* are typically 1-3 μm in length, the size of pore spaces most influenced by biomineralization might be strongly correlated to the ability of the cell to be transported into those pore spaces.

To complete this body of work, additional cores, both biomineralized and control cores should be exposed to $scCO_2$. This work is being performed in an ongoing collaboration with the University of Alabama, Birmingham. Also, collaboration with the University of Illinois, Urbana-Champaign will be required to better understand the biogenic impact or role of microbes in the nucleation and maturation of mineral formed during biomineralization through microscopic thin section analysis and SEM observations. Additional mercury intrusion porosimetry work with the collaboration of the Center for Advanced Mineral and Metallurgical Processing at Montana Tech will help improve the conclusions made about the pore sizes most impacted by biomineralization.

# CHAPTER SEVEN: CONCLUSIONS AND OUTLOOK

## Conclusions

Ureolysis-driven MICP has been suggested for a wide variety of engineered treatments including modification of construction materials, cementing porous media, hydraulic control and remediating environmental contaminants [8]. In the subsurface, MICP has been suggested to reduce permeability or seal fractures to improve the security of geologically stored $CO_2$ or for permanent well closure after hydraulic fracturing for fossil fuel extraction [4-6].

In this dissertation, MICP has been explored for subsurface application by (1) promoting and controlling precipitation with developed injection strategies and developing a model to predict the outcome of MICP treatments [27], (2) designing and constructing a large high pressure vessel to study the reduction of permeability due to MICP in a hydraulically fractured sandstone core under both low [6] and high pressure conditions and (3) reducing permeability and increasing minimum capillary displacement pressure (MCDP) in MICP treated Berea sandstone cores.

Injection strategies were developed to spatially and temporally control precipitation of $CaCO_3$. Precipitation is controlled by promoting ureolytic activity and manipulating the reaction and transport regimes to ultimately alter the saturation conditions to achieve the desired timing and location of $CaCO_3$ precipitation. Organisms or enzymes provide the catalyst for ureolysis and cells may act as nucleation sites for precipitation to occur. Also, the reaction rates and the transport rates of reactants can be manipulated by changing flow rates to influence transport rates or altering factors that influence the kinetics of ureolysis and precipitation reactions like fluid salinity and temperature. Whether and where $CaCO_3$ will precipitate is governed by the saturation state or saturation index which is determined by the activity of $Ca^{2+}$ and $CO_3^{2-}$.

The injection strategies employed in the sand-filled column experiments manipulate the saturation conditions to serve three goals (1) promote homogeneous distribution of calcium carbonate along the flow path, (2) prevent near injection point plugging, and (3) revive ureolytic activity after mineralization to promote further precipitation. To achieve these goals the columns were inoculated with *S. pasteurii*, biofilm growth was promoted and then different fluids were injected in a five step cycle over the course of several weeks (Figure 7.1). Note that in step 3 the ratio of reaction rate to transport rate i.e. the Damköhler number (*Da*), was designed to be less than one in an effort to homogeneously distribute the urea and calcium to promote uniform distribution of substrates available for reaction (and precipitation). Step 5 was discovered to be important as the microbes can become entombed in mineral leading to diffusion limitation of substrates or inhibition of cellular activity. These processes can lead to reduced ureolytic activity and thus decreasing $CaCO_3$ precipitation rates over time. Balancing promotion of ureolytic activity and biofilm growth with high calcium precipitation rates is an important consideration in the transition from the laboratory to the field. Efficient calcium precipitation can be promoted by reviving the ureolytic activity; however growth or revival stages might consume time. Therefore, a balance between cost and time required to achieve the treatment goal (for example reducing permeability or plugging) might have to be struck in planned and prospective field applications.

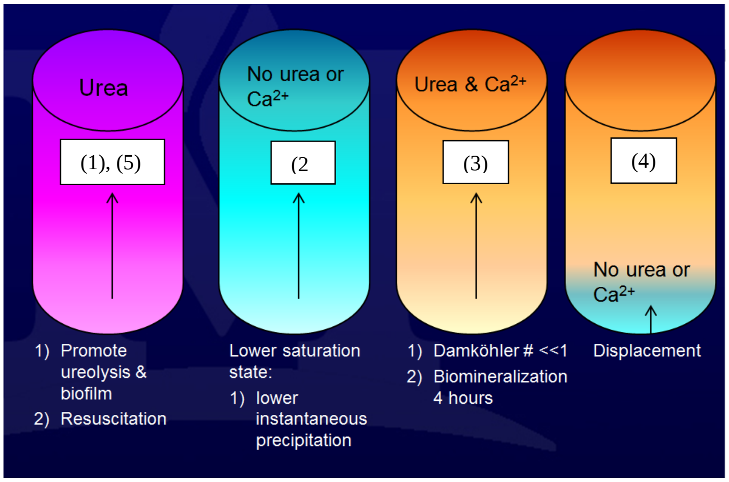

Figure 7.1 Schematic of injection strategies developed in sand-filled column studies. After inoculation, fluids were injected in the following manner: (1) Urea growth medium to promote *S. pasteurii* biofilm formation and ureolysis, (2) Saturation reducing medium (no urea, no calcium) to minimize instantaneous precipitation when calcium is introduced, (3) fast injection of Calcium medium with urea to promote ureolysis and precipitation in a batch biomineralization period, (4) Saturation reducing medium in the near injection point displaces the Calcium medium to minimize precipitation close to the injection point, and (5) Urea growth medium without calcium after the biomineralization period to resuscitate and revive the biofilm's ureolytic activity.

A Darcy-scale MICP model which was developed together with collaborators at the University of Stuttgart was calibrated using two column experiments and then used to predict calcium distribution in subsequent experiments. The model predicts the calcium distribution in experiments reasonably well. During a sensitivity analysis, it was observed that the model is most sensitive to fitted parameters associated with the urease and ureolytic activities of the biofilm [27]. Improving the understanding of these urease/biofilm relationships experimentally is currently being pursued and will strengthen the model's predictive capabilities. Also, the model simulations suggest that injection of pure, dense-phase $CO_2$ leads to limited calcite dissolution because the dissolution of

$CaCO_3$ buffers the pH of the medium, minimizing further dissolution. However, simulated injection of both $CO_2$ and water led to dissolution which was attributed to the injected water flushing out resident water reducing the buffering capacity of the calcite. Since $CO_2$ injections into Berea sandstone cores (Chapter 6) have recently been performed, additional model calibration may soon be possible.

The next efforts described in this dissertation highlight the use of the injection strategies developed in the sand-filled column studies to reduce permeability in meso-scale (approximately 1/2 meter) fractured sandstone cores. These experiments promoted MICP in relevant subsurface samples on both meso-scale and under pressure. Collaborators from Southern Company drilled a 74 cm diameter Boyles sandstone core from an outcrop of the Pottsville formation in Alabama. The core was hydraulically fractured and then twice sealed with MICP under ambient pressure conditions where the MICP treatment was observed to improve the strength of the fracture apparently three fold compared to the strength observed prior to treatment. Next a high pressure vessel was developed to study MICP treatment at elevated pressures relevant to subsurface conditions. During an experiment with confining pressure of 44 bar, MICP was demonstrated to reduce the fracture permeability by two orders of magnitude. However, more calcium pulses were required to reduce the fracture permeability as compared to MICP treatment under low pressure conditions (28 calcium pulses at high pressure versus 7 and 14 under low pressure). Observing differences between low and high pressure experiments (additional experimental details can be found in Appendix F and G) could be important when considering field deployment, where additional calcium or resuscitation events or even higher concentrations of reagents might be required to overcome non-ideal MICP promoting subsurface conditions.  Additional experiments on fractured or porous media samples, such as the recently developed sand pack system (Figure 7.2) under high pressure will help gain understanding of injection strategies to transition toward deep subsurface field deployment.

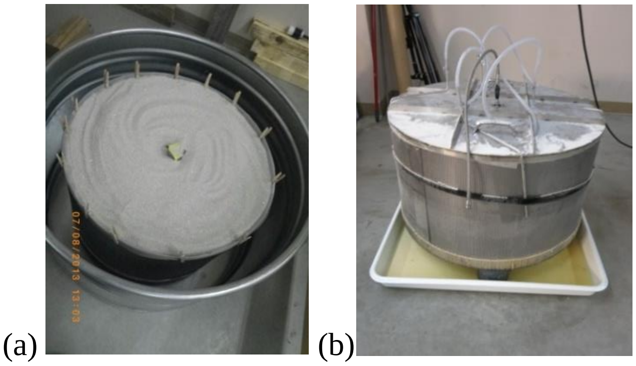

Figure 7.2. Sand pack sample for studying MICP in porous media under radial flow conditions and under pressure in the high pressure vessel. (a) Sand being filled into the sample's slotted screen with the center injection pipe covered to prevent sand intrusion into the simulated well, (b) slotted screen makes up the outside of the sand pack to hold the sand in but allow for fluids to flow out the circumference of the sand pack.

Finally, in 2.5 cm diameter Berea sandstone cores, permeability was reduced and minimum capillary displacement pressure (MCDP) was increased through MICP treatment.  The contribution of biofilm growth was observed to influence the permeability reduction and the number of calcium pulses necessary to reduce the overall permeability.  It was hypothesized that the biofilm may form a template for mineral formation, yet further thin-section analysis is required.  The porosity of the biomineralized cores was slightly reduced compared to an unmineralized control core, according to mercury intrusion porosimetry (MIP) results.  The MIP results also suggest that pores with the throat diameter between 6 and 16 μm were the most impacted by treatment with MICP.

MICP treated cores were subjected to $scCO_2$ for 24 hours and no significant impact was observed on permeability or MCDP. No differences in pore structure were observed between a pre-biomineralized, biomineralized and $scCO_2$ exposed core when examined with X-Ray CT (Appendix H). Replicate samples and those exposed to longer periods of $scCO_2$ need to be analyzed with MIP and for MCDP before and after $scCO_2$ exposure to assess the statistical significance of these observations. Overall, increasing the MCDP with MICP treatment and maintaining an increased MCDP after $scCO_2$ exposure is a promising step toward using MICP to alter cap rock permeability. Improving flow resistance through cap rock could make it less likely for $CO_2$ to escape from geologic storage reservoirs.

## Outlook

While the results presented show potential for deep subsurface field application of MICP, more research has to be performed to improve the understanding of how pressure, confining fluids, and scale-up impact MICP. Pressure and scale factors may influence the strength and/or integrity of the mineralization treatment. Studies in simulated fracture or delaminated composite cores (well cement, steel casing, formation material) will provide information about MICP in the near well bore interfaces, another important location of potential leakage pathways in addition to the cap rock. Supercritical $CO_2$ exposure should also be evaluated over longer time periods (beyond 24 hours) to determine if dissolution occurs and the length of time a mineral barrier can continue to reduce permeability. Calibrating models with the results of these experiments will help reduce laboratory efforts and allow for multiple scenarios to be examined under shorter than geologic times scales.

The Montana State University MICP research team is currently planning a field experiment to reduce permeability in a hydraulically fractured well at the Gorgas Power Station near Parrish, Alabama. In an effort to prepare for field deployment, several research questions have to be explored. First the experiment must promote MICP in the deployment time line (limited time will be allowed on-site). Second, the field experiment is limited by budget and resources. To continue to advance the control of MICP and meet the constraints of field deployment, several research questions are being explored (1) the dimensionless Damköhler number (*Da*), which is the ratio of reaction rate to transport rate, is being explored as a tool in MICP design for controlling ureolysis and precipitation, (2) the best substrate balance and sources of substrates (e.g. urea and calcium) are being researched to determine optimal $CaCO_3$ precipitation efficiency, to improve economic feasibility and to reduce unwanted byproduct production, and (3) nano- to micro-scale mineral nucleation processes are being examined to determine impacts to mineral growth, morphology and stability at larger scales.

Since controlling temporal and spatial saturation conditions and precipitation is a multi-factored reactive transport challenge, efforts to improve models will help improve the application of MICP technologies. Models can help predict treatment efficacy while decreasing the need for labor-intensive laboratory experiments [27, 62, 111-113]. Models are continually being improved by focusing on the fundamental processes at the micro-scale (e.g. ureolysis and growth kinetics, precipitation kinetics, crystal growth and microbe-mineral interactions) to integrate these process descriptions into Darcy-scale models for large-scale application design.  Modeling will continue to aid in the effort of transitioning ureolysis-driven MICP technologies from laboratory to field deployment.

# REFERENCES CITED

1. Cunningham, A. B.; Gerlach, R.; Spangler, L.; Mitchell, A. C., Microbially enhanced geologic containment of sequestered supercritical $CO_2$. *Energy Procedia* **2009,** *1*, (1), 3245-3252.

2. Cunningham, A. B.; Gerlach, R.; Spangler, L.; Mitchell, A. C.; Parks, S.; Phillips, A., Reducing the risk of well bore leakage of $CO_2$ using engineered biomineralization barriers. *Energy Procedia* **2011,** *4*, 5178-5185.

3. Cunningham, A.; Lauchnor, E.; Eldring, J.; Esposito, R.; Gerlach, R.; Phillips, A.; Ebigbo, A.; Spangler, L., Abandoned well $CO_2$ leakage mitigation using biologically induced mineralization: current progress and future directions. *Greenhouse Gases Science and Technology* **2013,** *2*, 1-10.

4. Mitchell, A.; Dideriksen, K.; Spangler, L.; Cunningham, A.; Gerlach, R., Microbially enhanced carbon capture and storage by mineral-trapping and solubility-trapping. *Environmental Science & Technology* **2010**, 5270-5276.

5. Mitchell, A. C.; Phillips, A. J.; Schultz, L.; Parks, S.; Spangler, L.; Cunningham, A.; Gerlach, R., Microbial $CaCO_3$ mineral formation and stability in an experimentally simulated high pressure saline aquifer with supercritical $CO_2$. *International Journal of Greenhouse Gas Control* **2013,** *15*, 86-96.

6. Phillips, A. J.; Lauchnor, E.; Eldring, J.; Esposito, R.; Mitchell, A. C.; Gerlach, R.; Cunningham, A. B.; Spangler, L. H., Potential $CO_2$ leakage reduction through biofilm-induced calcium carbonate precipitation. *Environmental Science & Technology* **2013,** *47*, (1), 142-149.

7. Schultz, L.; Pitts, B.; Mitchell, A. C.; Cunningham, A.; Gerlach, R., Imaging biologically induced mineralization in fully hydrated flow systems. *Microscopy Today* **2011,** *19*, (5), 12-15.

8. Phillips, A. J.; Gerlach, R.; Lauchnor, E.; Mitchell, A. C.; Cunningham, A. B.; Spangler, L., Engineered applications of ureolytic biomineralization: a review. *Biofouling* **2013,** *29*, (6), 715-733.

9. De Muynck, W.; De Belie, N.; Verstraete, W., Microbial carbonate precipitation in construction materials: A review. *Ecological Engineering* **2010,** *36*, (2), 118-136.

10. Achal, V.; Mukherjee, A.; Reddy, M. S., Microbial concrete: way to enhance the durability of building structures. *Journal of Materials in Civil Engineering* **2011,** *23*, (6), 730-734.

11. Siddique, R.; Chahal, N. K., Effect of ureolytic bacteria on concrete properties. *Construction and Building Materials* **2011,** *25*, (10), 3791-3801.

12. Harkes, M. P.; van Paassen, L. A.; Booster, J. L.; Whiffin, V. S.; van Loosdrecht, M. C. M., Fixation and distribution of bacterial activity in sand to induce carbonate precipitation for ground reinforcement. *Ecological Engineering* **2010,** *36*, (2), 112-117.

13. Whiffin, V.; van Paassen, L.; Harkes, M., Microbial carbonate precipitation as a soil improvement technique. *Geomicrobiology Journal* **2007,** *24*, 417-423.

14. van Paassen, L.; Ghose, R.; van der Linden, T.; van der Star, W.; van Loosdrecht, M., Quantifying biomediated ground improvement by ureolysis: large-scale biogrout experiment. *Journal of Geotechnical and Geoenvironmental Engineering* **2010,** *136*, (12), 1721-1728.

15. Ivanov, V.; Chu, J., Applications of microorganisms to geotechnical engineering for bioclogging and biocementation of soil in situ. *Reviews in Environmental Science and Biotechnology* **2008,** *7*, (2), 139-153.

16. Stabnikov, V.; Naeimi, M.; Ivanov, V.; Chu, J., Formation of water-impermeable crust on sand surface using biocement. *Cement and Concrete Research* **2011,** *41*, (11), 1143.

17. Burbank, M. B.; Weaver, T. J.; Green, T. L.; Williams, B. C.; Crawford, R. L., Precipitation of calcite by indigenous microorganisms to strengthen liquefiable soils. *Geomicrobiology Journal* **2011,** *28*, (4), 301-312.

18. DeJong, J. T.; Mortensen, B. M.; Martinez, B. C.; Nelson, D. C., Bio-mediated soil improvement. *Ecological Engineering* **2010,** *36*, (2), 197-210.

19. Ferris, F.; Stehmeier, L.; Kantzas, A.; Mourits, F., Bacteriogenic mineral plugging. *Journal of Canadian Petroleum Technology* **1996,** *35*, 56-61.

20. Fujita, Y.; Redden, G. D.; Ingram, J. C.; Cortez, M. M.; Ferris, F. G.; Smith, R. W., Strontium incorporation into calcite generated by bacterial ureolysis. *Geochimica et Cosmochimica Acta* **2004,** *68*, (15), 3261.

21. Fujita, Y.; Taylor, J.; Gresham, T.; Delwiche, M.; Colwell, F.; McLing, T.; Petzke, L.; Smith, R., Stimulation of microbial urea hydrolysis in groundwater to enhance calcite precipitation. *Environmental Science & Technology* **2008,** *42*, 3025-3032.

22. Fujita, Y.; Taylor, J.; Wendt, L.; Reed, D.; Smith, R., Evaluating the potential of native ueolytic microbes to remediate a (90)Sr contaminated environment. *Environmental Science & Technology* **2010,** *44*, (19), 7652-7658.

23. Achal, V.; Pan, X.; Zhang, D., Remediation of copper-contaminated soil by *Kocuria flava* CR1, based on microbially induced calcite precipitation. *Ecological Engineering* **2011,** *37*, (10), 1601-1605.

24. Achal, V.; Pan, X.; Fu, Q.; Zhang, D., Biomineralization based remediation of As(III) contaminated soil by *Sporosarcina ginsengisoli*. *Journal of Hazardous Materials* **2012,** *201–202*, (0), 178-184.

25. Achal, V.; Pan, X.; Zhang, D., Bioremediation of strontium (Sr) contaminated aquifer quartz sand based on carbonate precipitation induced by Sr resistant Halomonas sp. *Chemosphere* **2012,** *89*, (6), 764-768.

26. Lauchnor, E. G.; Schultz, L. N.; Bugni, S.; Mitchell, A. C.; Cunningham, A. B.; Gerlach, R., Bacterially induced calcium carbonate precipitation and strontium coprecipitation in a porous media flow system. *Environmental Science & Technology* **2013,** *47*, (3), 1557-1564.

27. Ebigbo, A.; Phillips, A.; Gerlach, R.; Helmig, R.; Cunningham, A. B.; Class, H.; Spangler, L. H., Darcy-scale modeling of microbially induced carbonate mineral precipitation in sand columns. *Water Resources Research* **2012,** *48*, (7), W07519.

28. Mitchell, A.; Phillips, A.; Hiebert, R.; Gerlach, R.; Spangler, L.; Cunningham, A., Biofilm enhanced geologic sequestration of supercritical $CO_2$. *International Journal of Greenhouse Gas Control* **2009**, 90-99.

29. Mitchell, A. C.; Phillips, A. J.; Hamilton, M. A.; Gerlach, R.; Hollis, W. K.; Kaszuba, J. P.; Cunningham, A. B., Resilience of planktonic and biofilm cultures to supercritical $CO_2$. *The Journal of Supercritical Fluids* **2008,** *47*, (2), 318-325.

30. Achal, V.; Mukherjee, A.; Basu, P.; Reddy, M., Lactose mother liquor as an alternative nutrient source for microbial concrete production by *Sporosarcina pasteurii*. *Journal of Industrial Microbiology & Biotechnology* **2009,** *36*, 433-438.

31. DeJong, J. T.; Soga, K.; Banwart, S. A.; Whalley, W. R.; Ginn, T. R.; Nelson, D. C.; Mortensen, B. M.; Martinez, B. C.; Barkouki, T., Soil engineering in vivo: harnessing natural biogeochemical systems for sustainable, multi-functional engineering solutions. *Journal of The Royal Society Interface* **2011,** *8*, (54), 1-15.

32. Al-Thawadi, S. M., Ureolytic bacteria and calcium carbonate formation as a mechanism of strength enhancement of sand. *Journal of Advanced Science and Engineering Research* **2011,** *1*, 98-114.

33. Fouke, B. W., Hot-spring systems geobiology: abiotic and biotic influences on travertine formation at Mammoth Hot Springs, Yellowstone National Park, USA. *Sedimentology* **2011,** *58*, (1), 170-219.

34. Northup, D. E.; Lavoie, K. H., Geomicrobiology of caves: A review. *Geomicrobiology Journal* **2001,** *18*, (3), 199-222.

35. Benzerara, K.; Miot, J.; Morin, G.; Ona-Nguema, G.; Skouri-Panet, F.; Férard, C., Significance, mechanisms and environmental implications of microbial biomineralization. *Comptes Rendus Geoscience* **2011,** *343*, (2-3), 160-167.

36. Decho, A. W., Overview of biopolymer-induced mineralization: What goes on in biofilms? *Ecological Engineering* **2010,** *36*, (2), 137-144.

37. Stocks-Fischer, S.; Galinat, J.; Bang, S., Microbiological precipitation of $CaCO_3$. *Soil Biology & Biochemistry* **1999,** *31*, (11), 1563-1571.

38. Hammes, F.; Verstraete, W., Key roles of pH and calcium metabolism in microbial carbonate precipitation. *Reviews in Environmental Science and Biotechnology* **2002,** *1*, 3-7.

39. Cuthbert, M. O.; Riley, M. S.; Handley-Sidhu, S.; Renshaw, J. C.; Tobler, D. J.; Phoenix, V. R.; Mackay, R., Controls on the rate of ureolysis and the morphology of carbonate precipitated by *S. pasteurii* biofilms and limits due to bacterial encapsulation. *Ecological Engineering* **2012,** *41*, 32-40.

40. Mortensen, B.; Haber, M.; DeJong, J.; Caslake, L.; Nelson, D., Effects of environmental factors on microbial induced calcium carbonate precipitation. *Journal of Applied Microbiology* **2011,** *111*, (2), 338-349.

41. Okwadha, G.; Li, J., Optimum conditions for microbial carbonate precipitation. *Chemosphere* **2010,** *81*, (9), 1143-1148.

42. Hammes, F.; Boon, N.; de Villiers, J.; Verstraete, W.; Siciliano, S., Strain-specific ureolytic microbial calcium carbonate precipitation. *Applied and Environmental Microbiology* **2003,** *69*, (8), 4901-4909.

43. Mobley, H. L. T.; Hausinger, R. P., Microbial ureases: significance, regulation, and molecular Characterization. *Microbiological Reviews* **1989,** *53*, (1), 85-108.

44. Burbank, M. B.; Weaver, T. J.; Williams, B. C.; Crawford, R. L., Urease activity of ureolytic bacteria isolated from six soils in which calcite was precipitated by indigenous bacteria. *Geomicrobiology Journal* **2012,** *29*, (4), 389-395.

45. Ferris, F.; Phoenix, V.; Fujita, Y.; Smith, R., Kinetics of calcite precipitation induced by ureolytic bacteria at 10 to 20 degrees C in artificial groundwater. *Geochimica Et Cosmochimica Acta* **2003,** *67*, (8), 1701-1710.

46. Yoon, J. H.; Lee, K. C.; Weiss, N.; Kho, Y. H.; Kang, K. H.; Park, Y. H., *Sporosarcina aquimarina* sp. nov., a bacterium isolated from seawater in Korea, and transfer of *Bacillus globisporus* (Larkin and Stokes 1967), *Bacillus psychrophilus* (Nakamura 1984) and *Bacillus pasteurii* (Chester 1898) to the genus *Sporosarcina* as *Sporosarcina globispora* comb. nov., *Sporosarcina psychrophila* comb. nov. and *Sporosarcina pasteurii* comb. nov., and emended description of the genus *Sporosarcina*. *International Journal of Systematic and Evolutionary Microbiology* **2001,** *51*, (3), 1079-1086.

47. DeJong, J. T., Microbially induced cementation to control sand response to undrained shear. *Journal of Geotechnical and Geoenvironmental Engineering* **2006,** *132*, (11), 1381.

48. van Veen, J. A., Fate and activity of microorganisms introduced into soil. *Microbiology and Molecular Biology Reviews* **1997,** *61*, (2), 121.

49. van Elsas, J.; Hill, P.; Chronakova, A.; Grekova, M.; Topalova, Y.; Elhottova, D.; Kristufek, V., Survival of genetically marked *Escherichia coli O157:H7* in soil as affected by soil microbial community shifts. *ISME Journal* **2007,** *1*, (3), 204-214.

50. Tobler, D. J.; Cuthbert, M. O.; Greswell, R. B.; Riley, M. S.; Renshaw, J. C.; Handley-Sidhu, S.; Phoenix, V. R., Comparison of rates of ureolysis between *Sporosarcina pasteurii* and an indigenous groundwater community under conditions required to precipitate large volumes of calcite. *Geochimica et Cosmochimica Acta* **2011,** *75*, (11), 3290-3301.

51. Martin, D.; Dodds, K.; Ngwenya, B.; Butler, I.; Elphick, S., Inhibition of *Sporosarcina pasteurii* under anoxic conditions: implications for subsurface carbonate precipitation and rmediation via ureolysis. *Environmental Science & Technology* **2012,** *46*, (15), 8351-8355.

52. Parks, S. L. Kinetics of calcite precipitation by ureolytic bacteria under aerobic and anaerobic conditions. Montana State University, Masters Thesis, 2009.

53. Zamarreño, D. V.; Inkpen, R.; May, E., Carbonate crystals precipitated by freshwater bacteria and their use as a limestone consolidant. *Applied and Environmental Microbiology* **2009,** *75*, (18), 5981-5990.

54. Dick, J.; De Windt, W.; De Graef, B.; Saveyn, H.; Van der Meeren, P.; De Belie, N.; Verstraete, W., Bio-deposition of a calcium carbonate layer on degraded limestone by *Bacillus* species. *Biodegradation* **2006,** *17*, (4), 357-367.

55. Mitchell, A.; Ferris, F., The coprecipitation of Sr into calcite precipitates induced by bacterial ureolysis in artificial groundwater: Temperature and kinetic dependence. *Geochimica et Cosmochimica Acta* **2005**, 4199-4210.

56. Dupraz, S.; Parmentier, M.; Menez, B.; Guyot, F., Experimental and numerical modeling of bacterially induced pH increase and calcite precipitation in saline aquifers. *Chemical Geology* **2009,** *265*, 44-53.

57. Fidaleo, M.; Lavecchia, R., Kinetic study of enzymatic urea hydrolysis in the pH range 4-9. *Chemical and Biochemical Engineering Quarterly* **2003,** *17*, (4), 311-318.

58. Domenico, P. A.; Schwartz, F. W., *Physical and Chemical Hydrogeology (2nd Edition)*. John Wiley & Sons: New York, 1998.

59. Dijk, P.; Berkowitz, B., Precipitation and dissolution of reactive solutes in fractures. *Water Resources Research* **1998,** *34*, (3), 457-470.

60. Berkowitz, B.; Zhou, J., Reactive solute transport in a single fracture. *Water Resources Research* **1996,** *32*, (4), 901-913.

61. Stumm, W.; Morgan, J. J., *Aquatic Chemistry: Chemical Equilibria and Rates in Natural Waters*. 3rd ed.; Wiley: New York, 1996; 1022 p.

62. Zhang, C.; Dehoff, K.; Hess, N.; Oostrom, M.; Wietsma, T. W.; Valocchi, A. J.; Fouke, B. W.; Werth, C. J., Pore-scale study of transverse mixing induced $CaCO_3$ precipitation and permeability reduction in a model subsurface sedimentary system. *Environmental Science & Technology* **2010,** *44*, (20), 7833-7838.

63. Mitchell, A.; Ferris, F., Effect of strontium contaminants upon the size and solubility of calcite crystals precipitated by the bacterial hydrolysis of urea. *Environmental Science & Technology* **2006**, 1008-1014.

64. Hammes, F., Ureolytic microbial calcium carbonate precipitation. In Ph.D. Thesis, Ghent University, 2002; p 161.

65. Douglas, S.; Beveridge, T., Mineral formation by bacteria in natural microbial communities. *FEMS Microbiology Ecology*, **1998**; Vol. 26, pp 79-88.

66. Mitchell, A.; Ferris, F., The Influence of *Bacillus pasteurii* on the nucleation and growth of calcium carbonate. *Geomicrobiology Journal* **2006**, 213-226.

67. De Muynck, W.; Debrouwer, D.; De Belie, N.; Verstraete, W., Bacterial carbonate precipitation improves the durability of cementitious materials. *Cement and Concrete Research* **2008,** *38*, (7), 1005-1014.

68. Braissant, O.; Cailleau, G.; Dupraz, C.; Verrecchia, A., Bacterially induced mineralization of calcium carbonate in terrestrial environments: The role of exopolysaccharides and amino acids. *Journal of Sedimentary Research* **2003**, 485-490.

69. Rodriguez-Navarro, C.; Jimenez-Lopez, C.; Rodriguez-Navarro, A.; Gonzalez-Muñoz, M. T.; Rodriguez-Gallego, M., Bacterially mediated mineralization of vaterite. *Geochimica et Cosmochimica Acta* **2007,** *71*, (5), 1197-1213.

70. Tourney, J.; Ngwenya, B. T., Bacterial extracellular polymeric substances (EPS) mediate $CaCO_3$ morphology and polymorphism. *Chemical Geology* **2009,** *262*, (3-4), 138-146.

71. Morse, J. W.; Casey, W. H., Ostwald processes and mineral paragenesis in sediments. *American Journal of Science* **1988,** *288*, (6), 537-560.

72. Jiménez-López, C.; Caballero, E.; Huertas, F. J.; Romanek, C. S., Chemical, mineralogical and isotope behavior, and phase transformation during the precipitation of calcium carbonate minerals from intermediate ionic solution at 25 C. *Geochimica et Cosmochimica Acta* **2001,** *65*, (19), 3219-3231.

73. Achal, V.; Mukherjee, A.; Reddy, M., Effect of calcifying bacteria on permeation properties of concrete structures. *Journal of Industrial Microbiology & Biotechnology* **2011,** *38*, (9), 1229.

74. De Muynck, W., Influence of pore structure on the effectiveness of a biogenic carbonate surface treatment for limestone conservation. *Applied and Environmental Microbiology* **2011,** *77*, (19), 6808-6820.

75. De Muynck, W.; Verbeken, K.; De Belie, N.; Verstraete, W., Influence of urea and calcium dosage on the effectiveness of bacterially induced carbonate precipitation on limestone. *Ecological Engineering* **2010,** *36*, (2), 99-111.

76. Chunxiang, Q.; Jianyun, W.; Ruixing, W.; Liang, C., Corrosion protection of cement-based building materials by surface deposition of $CaCO_3$ by *Bacillus pasteurii*. *Materials Science and Engineering: C* **2009,** *29*, (4), 1273-1280.

77. Whiffin, V. S., Microbial $CaCO_3$ precipitation for the production of biocement. In Ph.D. Thesis, Murdoch University, Australia, 2004; p 154.

78. Bang, S. S., Microbial calcite, a bio-based smart nanomaterial in concrete remediation. *International Journal of Smart & Nano Materials* **2010,** *1*, (1), 28-39.

79. Jonkers, H. M.; Thijssen, A.; Muyzer, G.; Copuroglu, O.; Schlangen, E., Application of bacteria as self-healing agent for the development of sustainable concrete. *Ecological Engineering* **2010,** *36*, (2), 230-235.

80. Wiktor, V.; Jonkers, H., Quantification of crack-healing in novel bacteria-based self-healing concrete. *Cement & Concrete Composites* **2011,** *33*, (7), 763-770.

81. Bang, S.; Galinat, J.; Ramakrishnan, V., Calcite precipitation induced by polyurethane-immobilized *Bacillus pasteurii*. *Enzyme and Microbial Technology* **2001,** *28*, (4-5), 404-409.

82. Bachmeier, K. L.; Williams, A. E.; Warmington, J. R.; Bang, S. S., Urease activity in microbiologically-induced calcite precipitation. *Journal of Biotechnology* **2002,** *93*, (2), 171-181.

83. Van Tittelboom, K.; De Belie, N.; De Muynck, W.; Verstraete, W., Use of bacteria to repair cracks in concrete. *Cement and Concrete Research* **2010,** *40*, (1), 157-166.

84. Wang, J.; Van Tittelboom, K.; De Belie, N.; Verstraete, W., Use of silica gel or polyurethane immobilized bacteria for self-healing concrete. *Construction and Building Materials* **2012,** *26*, (1), 532-540.

85. Ramachandran, S.; Ramakrishnan, V.; Bang, S., Remediation of concrete using micro-organisms. *Aci Materials Journal* **2001,** *98*, (1), 3-9.

86. Achal, V.; Pan, X.; Ozyurt, N., Improved strength and durability of fly ash-amended concrete by microbial calcite precipitation. *Ecological Engineering* **2011,** *37*, (4), 554-559.

87. Chahal, N.; Siddique, R.; Rajor, A., Influence of bacteria on the compressive strength, water absorption and rapid chloride permeability of fly ash concrete. *Construction and Building Materials* **2012,** *28*, 351-356.

88. Bang, S.; Min, S.-H.; Bang, S. S., Application of microbially induced soil stabilization technique for dust suppression. *International Journal of Geo-Engineering,* **2011**; Vol. 3, pp 27-37.

89. Gollapudi, U. K.; Knutson, C. L.; Bang, S. S.; Islam, M. R., A new method for controlling leaching through permeable channels. *Chemosphere* **1995,** *30*, (4), 695-705.

90. Cunningham, A. B.; Sharp, R. R.; Caccavo Jr, F.; Gerlach, R., Effects of starvation on bacterial transport through porous media. *Advances in Water Resources* **2007,** *30,* (6–7), 1583-1592.

91. Gerlach, R.; Cunningham, A. B., Influence of biofilms on porous media. In *Porous Media: Applications in Biological Systems and Biotechnology*, Vafai, K., Ed. Taylor and Francis: 2011; pp 173-230.

92. Foppen, J. W. A.; Schijven, J. F., Evaluation of data from the literature on the transport and survival of *Escherichia coli* and thermotolerant coliforms in aquifers under saturated conditions. *Water Research* **2006,** *40,* (3), 401-426.

93. Scholl, M. A.; Mills, A. L.; Herman, J. S.; Hornberger, G. M., The influence of mineralogy and solution chemistry on the attachment of bacteria to representative aquifer materials. *Journal of Contaminant Hydrology* **1990,** *6,* (4), 321-336.

94. Jenneman, G.; McInerney, M.; Knapp, R., Microbial penetration through nutrient-saturated berea sandstone. *Applied and Environmental Microbiology* **1985,** *50,* (2), 383-391.

95. Bouwer, E.; Rijnaarts, H.; Cunningham, A.; Gerlach, R., Biofilms in porous media. In *Biofilms II: Process Analysis and Applications*, Bryers, J., Ed. Wiley-Liss, Inc.: 2000; pp 123-158.

96. Mitchell, J. K.; Santamarina, J. C., Biological considerations in geotechnical engineering. *Journal of Geotechnical & Geoenvironmental Engineering* **2005,** *131,* (10), 1222-1233.

97. Rusu, C.; Cheng, X.; Li, M., Biological clogging in Tangshan sand columns under salt water intrusion by *Sporosarcina pasteurii*. *Advanced Materials Research,* **2011**; Vol. 250-253, pp 2040-2046.

98. Wu, Y.; J., A.-F.; Spycher, N.; Hubbard, S.; Zhang, G.; Williams, K.; Taylor, J.; Fujita, Y.; Smith, R., Geophysical monitoring and reactive transport modeling of ureolytically-driven calcium carbonate precipitation. *Geochemical Transactions* **2011,** *12*.

99. Warren, L. A.; Maurice, P. A.; Parmar, N.; Ferris, F. G., Microbially mediated calcium carbonate precipitation: implications for interpreting calcite precipitation and for solid-phase capture of inorganic contaminants. *Geomicrobiology Journal* **2001,** *18,* (1), 93-115.

100. Hua, B.; Deng, B.; Thornton, E.; Yang, J.; Amonette, J., Incorporation of chromate into calcium carbonate structure during coprecipitation. *Water Air and Soil Pollution* **2007,** *179*, (1-4), 381-390.

101. Kurmaç, Y., The impact of toxicity of metals on the activity of ureolytic mixed culture during the precipitation of calcium. *Journal of Hazardous Materials* **2009,** *163*, (2-3), 1063.

102. Okwadha, G. D. O.; Li, J., Biocontainment of polychlorinated biphenyls (PCBs) on flat concrete surfaces by microbial carbonate precipitation. *Journal of Environmental Management* **2011,** *92*, (10), 2860-2864.

103. Carey, W. J.; Svec, R.; Grigg, R.; Zhang, J.; Crow, W., Experimental investigation of wellbore integrity and $CO_2$–brine flow along the casing–cement microannulus. *International Journal of Greenhouse Gas Control* **2010,** *4*, (2), 272-282.

104. Wigand, M.; Kaszuba, J. P.; Carey, J. W.; Hollis, W. K., Geochemical effects of $CO_2$ sequestration on fractured wellbore cement at the cement/caprock interface. *Chemical Geology* **2009,** *265*, (1-2), 122-133.

105. Huerta, N. J.; Bryant, S. L.; Conrad, L., Cement core experiments with a conductive leakage pathway, under confining stress and alteration of cement's mechanical properties via a reactive fluid, as an analog for $CO_2$ leakage scenario. In *SPE/DOE Symposium on Improved Oil Recovery*, Society of Petroleum Engineers: Tulsa, OK., 2008; Vol. SPE 113375-MS.

106. Barlet-Gouédard, V.; Rimmelé, G.; Porcherie, O.; Quisel, N.; Desroches, J., A solution against well cement degradation under $CO_2$ geological storage environment. *International Journal of Greenhouse Gas Control* **2009,** *3*, (2), 206-216.

107. Dupraz, S.; Menez, B.; Gouze, P.; Leprovost, R.; Benezeth, P.; Pokrovsky, O.; Guyot, F., Experimental approach of $CO_2$ biomineralization in deep saline aquifers. *Chemical Geology* **2009,** *265*, 54-62.

108. Tobler, D.; Maclachlan, E.; Phoenix, V., Microbially mediated plugging of porous media and the impact of differing injection strategies. *Ecological Engineering* **2012,** *42*, 270-278.

109. Al Qabany, A.; Soga, K.; Santamarina, C., Factors affecting efficiency of microbially induced calcite precipitation. *Journal of Geotechnical and Geoenvironmental Engineering* **2012,** *138*, (8), 992-1001.

110. Achal, V.; Mukherjee, A.; Basu, P. C.; Reddy, M. S., Strain improvement of Sporosarcina pasteurii for enhanced urease and calcite production. *Journal of Industrial Microbiology & Biotechnology* **2009,** *36*, (7), 981-988.

111. Ebigbo, A.; Helmig, R.; Cunningham, A. B.; Class, H.; Gerlach, R., Modelling biofilm growth in the presence of carbon dioxide and water flow in the subsurface. *Advances in Water Resources* **2010,** *33*, (7), 762-781.

112. Barkouki, T.; Martinez, B.; Mortensen, B.; Weathers, T.; De Jong, J.; Ginn, T.; Spycher, N.; Smith, R.; Fujita, Y., Forward and inverse bio-geochemical modeling of microbially induced calcite precipitation in half-meter column experiments. *Transport in Porous Media* **2011,** *90*, (1), 23-39.

113. Fauriel, S.; Laloui, L., A bio-hydro-mechanical model for propagation of biogrout in soils. In *Geo-Frontiers 2011 Conference*, ASCE: Dallas, Texas, USA, 2011; pp 4041-4048.

114. Hammes, F., A novel approach to calcium removal from calcium-rich industrial wastewater. *Water Research (Oxford)* **2003,** *37*, (3), 699.

115. Wijngaarden, W.; Vermolen, F.; Meurs, G.; Vuik, C., Modelling biogrout: A new ground improvement method based on microbial-induced carbonate precipitation. *Transport in Porous Media* **2011,** *87*, (2), 397-420.

116. Bear, J., *Dynamincs of Fluids in Porous Media*. American Elsevier Co., Inc.: New York, NY, 1972; p 764.

117. van Noorden, T. L., Crystal precipitation and dissolution in a porous medium: effective equations and numerical experiments. *Multiscale Modeling & Simulation* **2009,** *7*, (3), 1220-1236.

118. van Noorden, T. L., Crystal precipitation and dissolution in a thin strip. *European Journal of Applied Mathematics* **2009,** *20*, (01), 69-91.

119. van Noorden, T. L.; Pop, I. S.; Ebigbo, A.; Helmig, R., An upscaled model for biofilm growth in a thin strip. *Water Resources Research* **2010,** *46*, (6).

120. Duijn, C. J. v.; Pop, I. S., Crystal dissolution and precipitation in porous media: pore scale analysis. *Journal für die Reine und Angewandte Mathematik (Crelles Journal)* **2004,** *2004*, (577), 171-211.

121. Golfier, F.; Wood, B. D.; Orgogozo, L.; Quintard, M.; Buès, M., Biofilms in porous media: development of macroscopic transport equations via volume averaging with

closure for local mass equilibrium conditions. *Advances in Water Resources* **2009,** *32*, (3), 463-485.

122. Class, H.; Helmig, R.; Bastian, P., Numerical simulation of non-isothermal multiphase multicomponent processes in porous media.: 1. An efficient solution technique. *Advances in Water Resources* **2002,** *25*, (5), 533-550.

123. Michaelides, E. E., Thermodynamic properties of geothermal fluids. *Trans.-Geothermal Resources Council;(United States)* **1981,** *5*, (CONF-811015-).

124. Chou, L. E. I.; Garrels, R. M.; Wollast, R., Comparative study of the kinetics and mechanisms of dissolution of carbonate minerals. *Chemical Geology* **1989,** *78*, (3), 269-282.

125. Flukiger, F.; Bernard, D., A new numerical model for pore scale dissolution of calcite due to $CO_2$ saturated water flow in 3D realistic geometry: Principles and first results. *Chemical Geology* **2009,** *265*, (1), 171-180.

126. Ciurli, S.; Marzadori, C.; Benini, S.; Deiana, S.; Gessa, C., Urease from the soil bacterium *Bacillus pasteurii*: Immobilization on Ca-polygalacturonate. *Soil Biology and Biochemistry* **1996,** *28*, (6), 811-817.

127. Klose, S.; Tabatabai, M. A., Urease activity of microbial biomass in soils. *Soil Biology and Biochemistry* **1999,** *31*, (2), 205-211.

128. Lloyd, A. B.; Sheaffe, M. J., Urease activity in soils. *Plant and Soil* **1973,** *39*, (1), 71-80.

129. Brotherton, J. E.; Emery, A.; Rodwell, V. W., Characterization of sand as a support for immobilized enzymes. *Biotechnology and Bioengineering* **1976,** *18*, (4), 527-543.

130. Li, Y. H.; Chen, Y. Y. M.; Burne, R. A., Regulation of urease gene expression by *Streptococcus salivarius* growing in biofilms. *Environmental Microbiology* **2000,** *2*, (2), 169-177.

131. Resch, A.; Rosenstein, R.; Nerz, C.; Götz, F., Differential gene expression profiling of *Staphylococcus aureus* cultivated under biofilm and planktonic conditions. *Applied and Environmental Microbiology* **2005,** *71*, (5), 2663-2676.

132. Wolf, M.; Breitkopf, O.; Puk, R., Solubility of calcite in different electrolytes at temperatures between 10° and 60° C and at $CO_2$ partial pressures of about 1 kPa. *Chemical Geology* **1989,** *76*, (3), 291-301.

133. Millero, F. J.; Milne, P. J.; Thurmond, V. L., The solubility of calcite, strontianite and witherite in NaCl solutions at 25 C. *Geochimica et Cosmochimica Acta* **1984,** *48,* (5), 1141-1143.

134. Clegg, S. L.; Whitfield, M., A chemical model of seawater including dissolved ammonia and the stoichiometric dissociation constant of ammonia in estuarine water and seawater from −2 to 40°C. *Geochimica et Cosmochimica Acta* **1995,** *59,* (12), 2403-2421.

135. Zhong, S.; Mucci, A., Calcite and aragonite precipitation from seawater solutions of various salinities: Precipitation rates and overgrowth compositions. *Chemical Geology* **1989,** *78,* (3), 283-299.

136. Compton, R. G.; Pritchard, K. L.; Unwin, P. R., The dissolution of calcite in acid waters: mass transport versus surface control. *Freshwater Biology* **1989,** *22,* (2), 285-288.

137. Millero, F.; Huang, F.; Graham, T.; Pierrot, D., The dissociation of carbonic acid in NaCl solutions as a function of concentration and temperature. *Geochimica et Cosmochimica Acta* **2007,** *71,* (1), 46-55.

138. Bell, T. G.; Johnson, M. T.; Jickells, T. D.; Liss, P. S., Ammonia/ammonium dissociation coefficient in seawater: A significant numerical correction. *Environmental Chemistry* **2008,** *5,* (3), 258.

139. Ji, J. Fundamental aspects of nickel electrowinning from chloride electrolytes. In Ph.D. Thesis, University of British Columbia, Canada, 1994.

140. Taylor, S. W.; Jaffé, P. R., Substrate and biomass transport in a porous medium. *Water Resources Research* **1990,** *26,* (9), 2181-2194.

141. Rockhold, M. L.; Yarwood, R. R.; Selker, J. S., Coupled microbial and transport processes in soils. *Vadose Zone Journal* **2004,** *3,* (2), 368-383.

142. Kim, D. S., Biomass evolution in porous media and its effects on permeability under starvation conditions. *Biotechnology and Bioengineering* **2000**, 69, (1), 47-56.

143. Zhang, T.; Klapper, I., Mathematical model of biofilm induced calcite precipitation. *Water Science Technology* **2010,** *61,* (11), 2957-64.

144. Rittman, B. E., The effect of shear stress on biofilm loss rate. *Biotechnology and Bioengineering* **1982,** *24,* (2), 501-506.

145. Speitel Jr, G. E.; DiGiano, F. A., Biofilm shearing under dynamic conditions. *Journal of Environmental Engineering* **1987,** *113,* (3), 464-475.

146. Murphy, E. M.; Ginn, T. R., Modeling microbial processes in porous media. *Hydrogeology Journal* **2000,** *8*, (1), 142-158.

147. Assteerawatt, A.; P. Bastian; A. Bielinski; T. Breiting; H. Class; A. Ebigbo; H. Eichel; S. Freiboth; R. Helmig; A. Kopp; J. Niessner; S. Ochs; A. Papafotiou; M. Paul; H. Sheta; D. Werner; Ölmann, U., MUFTE-UG: Structure, applications, and numerical methods. *Newsletter, International Groundwater Modeling Centre, Colorado School of Mines* **2005,** *23*, (2), 10.

148. Helmig, R.; Class, H.; Huber, R.; Sheta, H.; Ewing, R.; Hinkelmanm, R.; Jakobs, H.; Bastian, P., Architecture of the modular program system MUFTE-UG for simulating multiphase flow and transport processes in heterogeneous porous media. *Mathmatical Geology* **1998,** *2*, 123-131.

149. Norland, S.; Heldal, M.; Tumyr, O., On the relation between dry matter and volume of bacteria. *Microbial Ecology* **1987,** *13*, (2), 95-101.

150. Frippiat, C. C.; Pérez, P. C.; Holeyman, A. E., Estimation of laboratory-scale dispersivities using an annulus-and-core device. *Journal of Hydrology* **2008,** *362*, (1), 57-68.

151. Hao, O. J.; Richard, M. G.; Jenkins, D.; Blanch, H. W., The half-saturation coefficient for dissolved oxygen: A dynamic method for its determination and its effect on dual species competition. *Biotechnology and Bioengineering* **1983,** *25*, (2), 403-416.

152. Seto, M.; Alexander, M., Effect of bacterial density and substrate concentration on yield coefficients. *Applied and Environmental Microbiology* **1985,** *50*, (5), 1132-1136.

153. Mateles, R. I., Calculation of the oxygen required for cell production. *Biotechnology and Bioengineering* **1971,** *13*, (4), 581-582.

154. Kim, D.-S.; Thomas, S.; Fogler, H. S., Effects of pH and trace minerals on long-term starvation of *Leuconostoc mesenteroides*. *Applied and Environmental Microbiology* **2000,** *66*, (3), 976-981.

155. Krajewska, B., Ureases I. Functional, catalytic and kinetic properties: A review. *Journal of Molecular Catalysis B: Enzymatic* **2009,** *59*, (1), 9-21.

156. Melo, L. F., Biofilm physical structure, internal diffusivity and tortuosity. *Water Science and Technology* **2005**, 77-84.

157. Zhang, T. C.; Bishop, P. L., Density, porosity, and pore structure of biofilms. *Water Research* **1994,** *28*, (11), 2267-2277.

158. Tanyolaç, A.; Beyenal, H., Prediction of average biofilm density and performance of a spherical bioparticle under substrate inhibition. *Biotechnology and Bioengineering* **1997,** *56*, (3), 319-329.

159. Sausse, J.; Jacquot, E.; Fritz, B.; Leroy, J.; Lespinasse, M., Evolution of crack permeability during fluid-rock interaction. Example of the Brézouard granite (Vosges, France). *Tectonophysics* **2001,** *336*, (1-4), 199-214.

160. Zhang, X.; Jeffrey, R. G.; Bunger, A. P.; Thiercelin, M., Initiation and growth of a hydraulic fracture from a circular wellbore. *International Journal of Rock Mechanics and Mining Sciences* **2011,** *48*, (6), 984-995.

161. Esposito, A.; Benson, S. M., Remediation of possible leakage from geologic $CO_2$ storage reservoirs into groundwater aquifers. *Energy Procedia* **2011,** *4*, 3216-3223.

162. Carroll, S.; McNab, W.; Torres, S.; Singleton, M.; Zhao, P., Wellbore integrity in carbon sequestration environments: 1. Experimental study of Cement-Sandstone/Shale-Brine-$CO_2$. *Energy Procedia* **2011,** *4*, 5186-5194.

163. MacLeod, F. A.; Lappin-Scott, H. M.; Costerton, J. W., Plugging of a model rock system using starved bacteria. *Applied and Environmental Microbiology* **1988,** *54*, (6), 1365-1372.

164. Herigstad, B.; Hamilton, M.; Heersink, J., How to optimize the drop plate method for enumerating bacteria. *Journal of Microbiological Methods* **2001,** *44*, (2), 121-129.

165. Todd, D.; Mays, L., *Groundwater Hydrology*. 3rd edition ed.; John Wiley and Sons, Inc.: 2005.

166. Wheeler, L. A. Establishment of ureolytic biofilms and their influence on the permeability of pulse-flow porous media column systems. Masters Thesis, Montana State University, Bozeman, MT, 2009.

167. Gangi, A. F., Variation of whole and fractured porous rock permeability with confining pressure. *International Journal of Rock Mechanics and Mining Sciences & Geomechanics Abstracts* **1978,** *15*, (5), 249-257.

168. Nemati, M.; Voordouw, G., Modification of porous media permeabilty, using calcium carbonate produced enzymatically in situ. *Enzyme and Microbial Technology* **2003,** *33*, 635-642.

169. Barkley, W.; Richardson, J., Laboratory Safety. In *Manual of Methods for General Microbiology*, Gerhardt, P.; Murray, R.; Wood, E.; Willis, A.; Kreig, N., Eds. American Society of Microbiology: Washington, DC,, 1994; pp 715-734.

170. ASTM, Standard test method for permeability of rocks by flowing air, D4525-08. American Society for Testing and Materials International: West Conshohocken, PA, 2008.

171. Klinkenberg, L. J., The permeability of porous media to liquids and gases. In *Drilling and Production Practice*, American Petroleum Institute: 1941; pp 200-213.

172. Collins, R. E., *Flow of Fluids Through Porous Materials*. Pennwell Publishing Co.: Tulsa, OK, 1961; p 50-51.

173. Dicker, A. I.; Smits, R. M. In *A practical approach for determining permeability from laboratory pressure-pulse decay measurements*, SPE Iinternational Meeting on Petroleum Engineering, 1988; Society of Petroleum Engineers, Tianjin China, 1988.

174. Hildenbrand, A.; Schlömer, S.; Krooss, B. M., Gas breakthrough experiments on fine-grained sedimentary rocks. *Geofluids* **2002,** *2*, (1), 3-23.

175. Fu, L.; Milliken, K. L.; Sharp Jr, J. M., Porosity and permeability variations in fractured and liesegang-banded Breathitt sandstones (Middle Pennsylvanian), eastern Kentucky: diagenetic controls and implications for modeling dual-porosity systems. *Journal of Hydrology* **1994,** *154*, (1-4), 351-381.

176. Yale, D. P.; Meier, S. W.; Leonardi, S. A.; Joyce, G. M.; Kushnick, A. P.; Wang, J. In *Large-scale laboratory testing of petroleum reservoir processes*, SPE Annual Technical Conference and Exhibition, 2010; Society of Petroleum Engineers: Florence, Italy, 2010.

177. McCallum, S. D.; Riestenberg, D. E.; Zatsepina, O. Y.; Phelps, T. J., Effect of pressure vessel size on the formation of gas hydrates. *Journal of Petroleum Science and Engineering* **2007,** *56*, (1–3), 54-64.

178. Fitzgerald, G. C.; Castaldi, M. J.; Zhou, Y., Large scale reactor details and results for the formation and decomposition of methane hydrates via thermal stimulation dissociation. *Journal of Petroleum Science and Engineering* **2012,** *94–95*, (0), 19-27.

179. Eaton, M.; Mahajan, D.; Flood, R., A novel high-pressure apparatus to study hydrate–sediment interactions. *Journal of Petroleum Science and Engineering* **2007,** *56*, (1–3), 101-107.

180. Bianchi, A.; Garcin, J.; Tholosan, O., A high-pressure serial sampler to measure microbial activity in the deep sea. *Deep Sea Research Part I: Oceanographic Research Papers* **1999,** *46*, (12), 2129-2142.

181. Spilimbergo, S.; Elvassore, N.; Bertucco, A., Microbial inactivation by high-pressure. *The Journal of Supercritical Fluids* **2002,** *22*, (1), 55-63.

182. Bartlett, D. H., Pressure effects on in vivo microbial processes. *Biochimica et Biophysica Acta (BBA) - Protein Structure and Molecular Enzymology* **2002,** *1595,* (1–2), 367-381.

183. Abe, F.; Kato, C.; Horikoshi, K., Pressure-regulated metabolism in microorganisms. *Trends in Microbiology* **1999,** *7*, (11), 447-453.

184. Martin, D.; Dodds, K.; Butler, I. B.; Ngwenya, B. T., Carbonate precipitation under pressure for bioengineering in the anaerobic subsurface via denitrification. *Environmental Science & Technology* **2013**, 47, (15), 8692-8699.

185. Ali, H. S.; Al-Marhoun, M. A.; Abu-Khamsin, S. A.; Celik, M. S. In *The effect of overburden pressure on relative permeability*, Fifth Middle East Oil Show, Manama, Bahrain, 1987; Society of Petroleum Engineers: Manama, Bahrain, 1987; pp 335-341.

186. Fatt, I., The effect of overburden pressure on relative permeability. *Journal of Petroleum Technology* **1953,** *5*, (10), 15-16.

187. Dhami, N. K.; Reddy, M. S.; Mukherjee, A., Improvement in strength properties of ash bricks by bacterial calcite. *Ecological Engineering* **2012,** *39*, (0), 31-35.

188. Sagar, B.; Runchal, A., Permeability of fractured rock: Effect of fracture size and data uncertainties. *Water Resources Research* **1982,** *18*, (2), 266-274.

189. Wollenweber, J.; Alles, S.; Busch, A.; Krooss, B. M.; Stanjek, H.; Littke, R., Experimental investigation of the $CO_2$ sealing efficiency of caprocks. *International Journal of Greenhouse Gas Control* **2010,** *4*, (2), 231-241.

190. Bachu, S., Sequestration of $CO_2$ in geological media: criteria and approach for site selection in response to climate change. *Energy Conversion and Management* **2000,** *41*, (9), 953-970.

191. Bachu, S., Legal and regulatory challenges in the implementation of $CO_2$ geological storage: An Alberta and Canadian perspective. *International Journal of Greenhouse Gas Control* **2008,** *2*, (2), 259-273.

192. Bachu, S.; Bennion, D. B., Experimental assessment of brine and/or $CO_2$ leakage through well cements at reservoir conditions. *International Journal of Greenhouse Gas Control* **2009,** *3*, (4), 494-501.

193. Hildenbrand, A.; Schlömer, S.; Krooss, B. M.; Littke, R., Gas breakthrough experiments on pelitic rocks: comparative study with $N_2$, $CO_2$ and $CH_4$. *Geofluids* **2004,** *4*, (1), 61-80.

194. Tanikawa, W.; Shimamoto, T., Klinkenberg effect for gas permeability and its comparison to water permeability for porous sedimentary rocks. *Hydrology and Earth System Sciences Discussions* **2006,** *3*, (4), 1315-1338.

195. Wu, Y.-S.; Pruess, K.; Persoff, p., Gas Flow in Porous Media With Klinkenberg Effects. *Transport in Porous Media* **1998,** *32*, (1), 117-137.

196. Mitchell, A. C.; Phillips, A. J.; Kaszuba, J. P.; Hollis, W. K.; Cunningham, A. L. B.; Gerlach, R., Microbially enhanced carbonate mineralization and the geologic containment of $CO_2$. *Geochimica et Cosmochimica Acta* **2008,** *72*, (12), A636-A636.

197. Webb, P. *An introduction to the physical characterization of materials by mercury intrusion porosimetry with emphasis on reduction and presentation of experimental data*; Micromeritics Instrument Corp.: 2001.

198. Gasda, S. E.; Bachu, S.; Celia, M. A., Spatial characterization of the location of potentially leaky wells penetrating a deep saline aquifer in a mature sedimentary basin. *Environmental Geology* **2004,** *46*, (6/7), 707-720.

199. Jung, D.; Biggs, H.; Erikson, J.; Ledyard, P., New colorimetric reaction for end-point, continuous-flow, and kinetic measurement of urea. *Clinical Chemistry* **1975,** *21*, (8), 1136-1140.

200. Kalia, N.; Balakotaiah, V., Modeling and analysis of wormhole formation in reactive dissolution of carbonate rocks. *Chemical Engineering Science* **2007,** *62*, (4), 919-928.

# APPENDICES

# APPENDIX A

## ADDITIONAL RESEARCH: BIOFILM ENHANCED GEOLOGIC SEQUESTRATION OF SUPERCRITICAL $CO_2$

## Abstract

In order to develop subsurface $CO_2$ storage as a viable engineered mechanism to reduce the emission of $CO_2$ into the atmosphere, any potential leakage of injected supercritical $CO_2$ (SC-$CO_2$) from the deep subsurface to the atmosphere must be reduced. Here, we investigate the utility of biofilms, which are microorganism assemblages firmly attached to a surface, as a means of reducing the permeability of deep subsurface porous geological matrices under high pressure and in the presence of SC-$CO_2$, using a unique high pressure (8.9 MPa), moderate temperature (32°C) flow reactor containing 40 millidarcy Berea sandstone cores. The flow reactor containing the sandstone core was inoculated with the biofilm forming organism *Shewanella fridgidimarina*. Electron microscopy of the rock core revealed substantial biofilm growth and accumulation under high-pressure conditions in the rock pore space which caused >95% reduction in core permeability. Permeability increased only slightly in response to SC-$CO_2$ challenges of up to 71 h and starvation for up to 363 h in length. Viable population assays of microorganisms in the effluent indicated survival of the cells following SC-$CO_2$ challenges and starvation, although *S. fridgidimarina* was succeeded by *Bacillus mojavensis* and *Citrobacter sp*. which were native in the core. These observations suggest that engineered biofilm barriers may be used to enhance the geologic sequestration of atmospheric $CO_2$.

## Citation

Mitchell, A.; Phillips, A.J; Hiebert, R.; Gerlach, R.; Spangler, L.; Cunningham, A., Biofilm enhanced geologic sequestration of supercritical $CO_2$. *International Journal of Greenhouse Gas Control*. 2009, 90-99.

# APPENDIX B

# ADDITIONAL RESEARCH: RESILIENCE OF PLANKTONIC AND BIOFILM CULTURES TO SUPERCRITICAL $CO_2$

## Abstract

Supercritical $CO_2$ has been shown to act as a disinfectant against microorganisms. These organisms have most often been tested in vegetative or spore form. Since biofilm organisms are typically more resilient to physical, chemical, and biological stresses than the same organisms in planktonic form, they are often considered more difficult to eradicate. It is therefore hypothesized that supercritical $CO_2$ (SC–$CO_2$) induced inactivation of biofilm organisms would be less effective than against planktonic (suspended) growth cultures of the same organism. Six-day old biofilm cultures as well as suspended planktonic cultures of *Bacillus mojavensis* were exposed to flowing SC–$CO_2$ at 136 atm and 35◦C for 19 min and slowly depressurized after treatment. After SC–$CO_2$ exposure, *B. mojavensis* samples were analyzed for total and viable cells. Suspended cultures revealed a 3 $\log_{10}$ reduction while biofilm cultures showed a 1 $\log_{10}$ reduction in viable cell numbers. These data demonstrate that biofilm cultures of *B. mojavensis* are more resilient to SC–$CO_2$ than suspended planktonic communities. It is hypothesized that the small reduction in the viability of biofilm microorganisms reflects the protective effects of extracellular polymeric substances (EPS) which make up the biofilm matrix, which offer mass transport resistance, a large surface area, and a number of functional groups for interaction with and immobilization of $CO_2$. The resistance of biofilm suggests that higher pressures, longer durations of SC–$CO_2$ exposure, and a quicker depressurization rate may be required to eradicate biofilms during the sterilization of heat-sensitive materials in medical and industrial applications. However, the observed resilience of biofilms to SC–$CO_2$ is particularly promising for the prospective application of subsurface biofilms in the subsurface geologic sequestration of $CO_2$.

## Citation

Mitchell, A. C.; Phillips, A. J.; Hamilton, M. A.; Gerlach, R.; Hollis, W. K.; Kaszuba, J. P.; Cunningham, A. B., Resilience of planktonic and biofilm cultures to supercritical $CO_2$. *The Journal of Supercritical Fluids*. 2008, 47, (2), 318-325.

# APPENDIX C

## ADDITIONAL RESEARCH: REDUCING THE RISK OF WELL BORE LEAKAGE OF $CO_2$ USING ENGINEERED BIOMINERALIZATION BARRIERS

## Abstract

If $CO_2$ is injected in deep geological formations it is important that the receiving formation has sufficient porosity and permeability for storage and transmission and be overlain by a suitable low permeability cap rock formation. When the resulting $CO_2$ plume encounters a well bore, leakage may occur through various pathways in the "disturbed zone" surrounding the well casing. Gasda et al.[198] propose a method for determining effective well bore permeability from a field pressure test. If permeability results from such tests prove unacceptably large, strategies for *in situ* mitigation of potential leakage pathways become important. To be effective, leakage mitigation methods must block leakage pathways on timescales longer than the plume will be mobile, be able to be delivered without causing well screen plugging, and be resistant to supercritical $CO_2$ ($ScCO_2$) challenges.

Traditional mitigation uses cement, a viscous fluid that requires a large enough aperture for delivery and that also must bond to the surrounding surfaces in order to be effective. Technologies that can be delivered via low viscosity fluids and that can effectively plug small aperture pathways, or even the porous rock surrounding the well could have significant advantages for some leakage scenarios. We propose a microbially mediated method for plugging preferential leakage pathways and/or porous media, thereby lowering the risk of unwanted upward migration of $CO_2$, similar to that discussed by Mitchell et al [4]. We examine the concept of using engineered microbial biofilms which are capable of precipitating crystalline calcium carbonate using the process of ureolysis. The resulting combination of biofilm plus mineral deposits, if targeted near points of $CO_2$ injection, may result in the long-term sealing of preferential leakage pathways. Successful development of these biologically-based concepts could result in a $CO_2$ leakage mitigation technology which can be applied either before $CO_2$ injection or as a remedial measure. Results from laboratory column studies are presented which illustrate how biomineralization deposits can be developed along packed sand columns at length scales of 2.54 cm and 61 cm. Strategies for controlling mineral deposition of uniform thickness along the axis of flow are also discussed.

## Citation

Cunningham, A. B.; Gerlach, R.; Spangler, L.; Mitchell, A. C.; Parks, S.; Phillips, A., Reducing the risk of well bore leakage of $CO_2$ using engineered biomineralization barriers. *Energy Procedia* 2011, 4, 5178-5185.

# APPENDIX D

# ADDITIONAL RESEARCH: ABANDONED WELL $CO_2$ LEAKAGE MITIGATION USING BIOLOGICALLY INDUCED MINERALIZATION: CURRENT PROGRESS AND FUTURE DIRECTIONS

## Abstract

Methods of mitigating leakage or re-plugging abandoned wells before exposure to $CO_2$ are of high potential interest to prevent leakage of $CO_2$ injected for geologic carbon sequestration in depleted oil and gas reservoirs where large numbers of abandoned wells are often present. While $CO_2$ resistant cements and ultrafine cements are being developed, technologies that can be delivered via low viscosity fluids could have significant advantages including the ability to plug small aperture leaks such as fractures or delamination interfaces. Additionally there is the potential to plug rock formation pore space around the wellbore in particularly problematic situations. We are carrying out research on the use of microbial biofilms capable of inducing the precipitation of crystalline calcium carbonate using the process of ureolysis. This method has the potential to reduce well bore permeability, coat cement to reduce $CO_2$–related corrosion, and lower the risk of unwanted upward $CO_2$ migration. In this spotlight, we highlight research currently underway at the Center for Biofilm Engineering (CBE) at Montana State University (MSU) in the area of ureolytic biomineralization sealing for reducing $CO_2$ leakage risk. This research program combines two novel core testing systems and a 3-dimensional simulation model to investigate biomineralization under both radial and axial flow conditions and at temperatures and pressures which permit $CO_2$ to exist in the supercritical state. This combination of modeling and experimentation is ultimately aimed at developing and verifying biomineralization sealing technologies and strategies which can successfully be applied at the field scale for carbon capture and geological storage (CCGS) projects.

## Citation

Cunningham, A.; Lauchnor, E.; Eldring, J.; Esposito, R.; Gerlach, R.; Phillips, A.; Ebigbo, A.; Spangler, L., Abandoned well $CO_2$ leakage mitigation using biologically induced mineralization: current progress and future directions. *Greenhouse Gases Science and Technology* 2013, 2, 1-10.

# APPENDIX E

# ADDITIONAL RESEARCH: MICROBIAL $CaCO_3$ MINERAL FORMATION AND STABILITY IN AN EXPERIMENTALLY SIMULATED HIGH PRESSURE SALINE AQUIFER WITH SUPERCRITICAL $CO_2$.

## Abstract

The use of microbiologically induced mineralization to plug pore spaces is a novel biotechnology to mitigate the potential leakage of geologically sequestered carbon dioxide from preferential leakage pathways. The bacterial hydrolysis of urea (ureolysis) which can induce calcium carbonate precipitation, via a pH increase and the production of carbonate ions, was investigated under conditions that approximate sub-surface storage environments, using a unique high pressure (~7.5 MPa) moderate temperature (32°C) flow reactor housing a synthetic porous media core. The synthetic core was inoculated with the ureolytic organism *Sporosarcina pasteurii* and pulse-flow of a urea inclusive saline growth medium was established through the core. The system was gradually pressurized to 7.5 MPa over the first 29 days. Concentrations of $NH_4^+$, a by-product of urea hydrolysis, increased in the flow reactor effluent over the first 20 days, and then stabilized at a maximum concentration consistent with the hydrolysis of all the available urea. pH increased over the first 6 days from 7 to 9.1, consistent with buffering by $NH_4^+ \Leftrightarrow NH_3 + H^+$. Ureolytic colony forming units were consistently detected in the reactor effluent, indicating a biofilm developed in the high pressure system and maintained viability at pressures up to 7.5 MPa. All available calcium was precipitated as calcite. Calcite precipitates were exposed to dry supercritical $CO_2$ ($scCO_2$), water-saturated $scCO_2$, $scCO_2$-saturated brine, and atmospheric pressure brine. Calcite precipitates were resilient to dry $scCO_2$, but suffered some mass loss in water-saturated $scCO_2$ (mass loss 17 ± 3.6% after 48 h, 36 ± 7.5% after 2 h). Observations in the presence of $scCO_2$ saturated brine were ambiguous due to an artifact associated with the depressurization of the $scCO_2$ saturated brine before sampling. The degassing of pressurized brine resulted in significant abrasion of calcite crystals and resulted in a mass loss of approximately 92 ± 50% after 48 h. However dissolution of calcite crystals in brine at atmospheric pressure, but at the pH of the $scCO_2$ saturated brine, accounted for only approximately 7.8 ± 2.2% of the mass loss over the 48 h period. These data suggest that microbially induced mineralization, with the purpose of reducing the permeability of preferential leakage pathways during the operation of GCS, can occur under high pressure $scCO_2$ injection conditions.

## Citation

Mitchell, A. C.; Phillips, A. J.; Schultz, L.; Parks, S.; Spangler, L.; Cunningham, A.; Gerlach, R., Microbial $CaCO_3$ mineral formation and stability in an experimentally simulated high pressure saline aquifer with supercritical $CO_2$. *International Journal of Greenhouse Gas Control*. 15 (2013) 86–96

# APPENDIX F

# KINETICS OF UREOLYSIS UNDER LOW AND HIGH PRESSURE CONDITIONS

## Description of Experimental Conditions

Collaborators at the University of Stuttgart require data to calibrate their Darcy-scale model which was described in this dissertation in Chapter 3. In particular, the question of whether differences to kinetics of ureolysis or precipitation existed between high and low pressure conditions was of interest. To begin to answer the question, a study was undertaken to assess high and low pressure urea hydrolysis reaction kinetics. To study these kinetic relationships the high pressure pH and conductivity probe bank normally associated with the high pressure vessel described in Chapter 5 were used as a small (~60 ml) batch reactor. Two pressures were studied, ambient (atmospheric) and 96.5 bar.

Kinetics of ureolysis (urea is non-ionic) can be monitored by surrogate of the ionic $NH_4^+$ production which can be measured as an increase in conductivity (Eq. 1) [77]. In this experiment, the high pressure pH and conductivity probe bank (Barben Analyzer Technologies) was removed from the high pressure fluid delivery system and placed on a shaker and attached to one of the high pressure Isco pumps via flexible stainless steel tubing (Swagelok, ID, USA). The probe bank was disinfected by pumping a Bleach/Tween solution followed by distilled water, then a sodium thiosulfate solution followed by 70% ethanol [27]. The probes were then rinsed and stored in sterile buffer. Immediately prior to inoculation the probe bank was drained and filled with 60 ml of fresh sterile growth medium. The entire probe bank was shaken at 100 rpm as the medium equilibrated for approximately 10 min, then conductivity and pH were recorded prior to inoculation.

A culture of *S. pasteurii* was grown overnight by starting a culture from frozen stock, with 100 µl inoculated into 100 ml of 37 g/L and 20 g/L urea medium and shaken at 150 rpm on an incubated (30°C) shaker. After 24 hours, the culture was transferred to fresh BHI+Urea medium then grown to stationary phase prior to centrifugation three times at 6000 rpm for 10 min and re-suspension in 40 ml growth medium. After the final resuspension the optical density was measured by aliquoting in triplicate 200 µl of the culture to a 96 well plate and measuring optical density at 600 nm ($OD_{600}$) with a Biotek Synergy HT (Biotek) plate reader. The final $OD_{600}$ was 1.4.

Low and high pressure experiments were run in triplicate and each began by inoculating 40 ml of the 1.4 $OD_{600}$ culture into the probe bank. Immediately, a 0.5 ml time zero sample was taken and 0.1 ml of the sample was used to assess culturable population via the drop plate method [164] and 0.4 ml filtered with a 0.2 µm syringe filter for urea analysis. Urea was assessed by colorimetric assay modeled after the Jung assay[199]. The modified Jung assay is a colorimetric 96 well plate method where:

1. 125 µL of Reagent 2 were added into each well (samples and standards were run in triplicate)
2. 10 µL of each sample and standard were added to the wells

  - Standards were 2.5, 2.0, 1.5, 1.0, 0.5 and 0.25 g/L of urea with DI water as a blank sample
  - Samples were diluted appropriately (1:10 for high urea samples, undiluted for low urea samples)
3. 125 µL of Reagent 3 was added into each well
4. The wells were mixed by pulling the solution into a multi-channel pipette and injecting it back into the plate. (Tips were changed between wells)
5. The plate was incubated for 30 minutes at 37° C
6. Absorbance was read at 505 nm

Reagents:

Reagent 1 – 33% Brij Solution:
1. 1 mL of Brij-L23 into 29ml of water

Reagent 2 – o-Phthalaldehyde
1. 800ml of distilled $H_2O$ was added to a 1L volumetric flask.
2. 74ml of concentrated $H_2SO_4$ was added to the flask
3. The solution was allowed to cool, then 200mg of o-phthalaldehyde and 1ml of reagent 1 were added to the flask
4. Water was added to a final volume of 1L

Reagent 3 – NED reagent
1. 600mL of distilled water was added to a 1L volumetric flask
2. 5.0 g of Boric acid was added and allowed to dissolve
3. 222mL of concentrated $H_2SO_4$ was then added to the flask
4. The solution was allowed to cool to room temperature then 600mg of N-1-napthylethylenediamine dihydrochloride (NED) and 1mL of reagent 1 were added
5. Water was added to a final volume of 1L

In each high and low pressure experiments; pH & conductivity were monitored over time. In the low pressure experiments samples were collected every 7.5 minutes for the first hour and every 15 minutes thereafter and filtered for urea analysis. In the high pressure experiment, pressure was increased by using a Teledyne Isco pump in constant pressure mode to increase the probe bank pressure from ambient conditions to 96.5 bar over approximately 2 minutes before isolating the probe bank. In the high pressure experiment since pressure would reduce if sampling occurred; only time zero and endpoint samples were collected. Experiments were conducted for two hours.

Conductivity was correlated to the results of the low pressure experiment urea assay using linear regression analysis. Then that correlation was used to calculate the urea concentration in the high pressure experiments based on the conductivity readings. Following, three kinetic models (Zero order, first order and Michaelis-Menten type) were examined by minimizing the sum of squared error between the data and the model to determine whether there was a significant difference to the ureolysis kinetics under these conditions where [U] is the concentration of urea, $r_{urea}$ is the rate of ureolysis, $v_{max}$ is the maximum rate of ureolysis and $K_m$ is the half saturation coefficient:

Zero order: $r_{urea} = \frac{du}{dt} = -k$  First order: $r_{urea} = \frac{du}{dt} = -k[U]$

Michaelis-Menten: $r_{urea} = \frac{du}{dt} = \frac{v_{max}[U]}{K_m + [U]}$

## Results: Ureolysis kinetics

Urea concentration was correlated to conductivity through linear regression (Figure Appendix F.1).

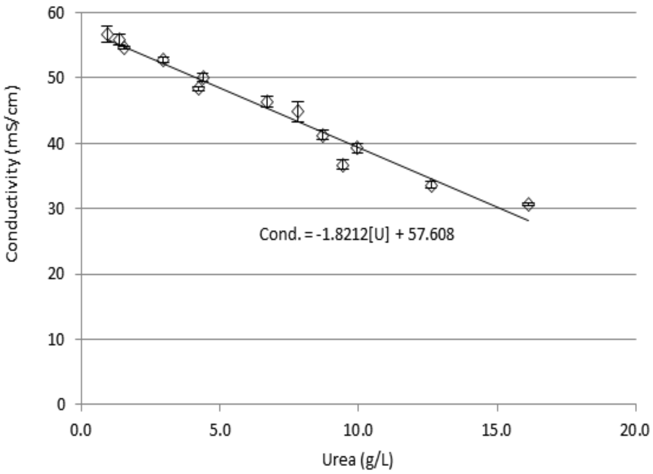

Figure Appendix F.1. Correlation of urea concentration to conductivity (◊). Linear regression fit the data with a line with an $R^2$ of 0.97.

The slope and intercept of the line were used to convert high pressure data to urea concentration and the high and low pressure urea data was compared between three kinetic models (Table Appendix F.1). The zero order model fit the first hour of the data (Figure Appendix F.2), whereas first order fit better to the two hour data (Figure Appendix F.3).

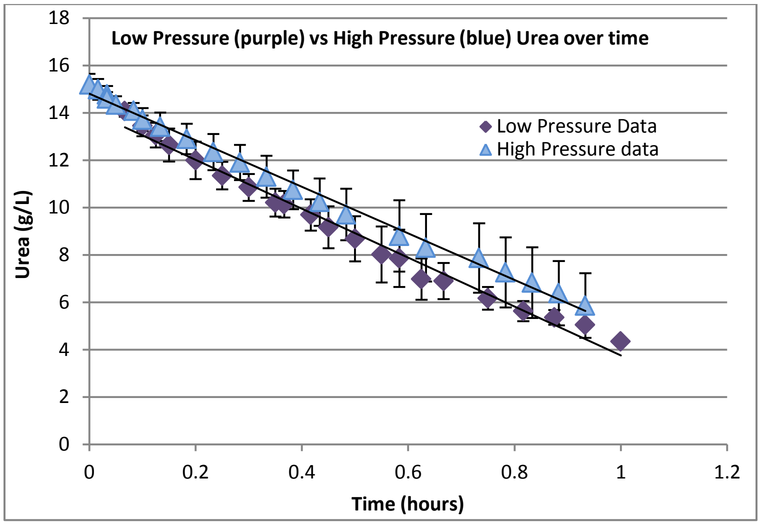

Figure Appendix F.2. Zero order model comparison of urea degradation under high and low pressure conditions. The zero order model fit best to the first hour of the data .

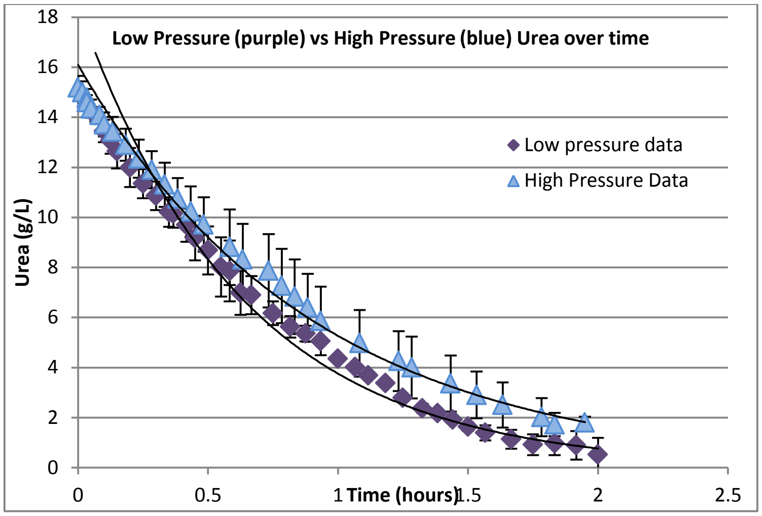

Figure Appendix F.3. First order model comparison of urea degradation under high and low pressure conditions. The first order model fit best to the first two hours of the data.

Michaelis-Menten (MM) kinetic model did not fit well to this data as evidenced by the high standard deviation surrounding the fitted parameters of $k_m$ and $v_{max}$ (Table Appendix F.1). The MM model might not fit these data well because at these urea concentrations the maximum rate of urea hydrolysis may not yet be observed. All of the models suggest that kinetic parameters are within the standard deviation of each other between low and high pressure suggesting no difference between the rates of ureolysis under these conditions.

Table Appendix F.1. Kinetic parameters derived from least sum of squares error method.

| | | |
|---|---|---|
| High Pressure | Zero | $r_{urea}$= 9.46 g/L/hr ± 1.22 |
| | First | k= 1.00 ± 0.23 ($hr^{-1}$) |
| | MM | $k_m$ =14.5 g/L ± 6.6 |
| | | $v_{max}$ =27.7 g/L/hr ± 12.8 |
| Low Pressure | Zero | $r_{urea}$ = 10.48 g/L/hr ± 0.64 |
| | First | k=1.19 ±0.05 ($hr^{-1}$) |
| | MM | $k_m$ =17.2 g/L ± 12 |
| | | $v_{max}$ =29.4g/L/hr ± 15.1 |

In conclusion, the study reveals that under the conditions tested, there was no statistically significant difference to ureolysis kinetics between low (ambient pressure) and high pressure (96.5 bar).

# APPENDIX G

# COMPARISON OF UREOLYSIS AND $CaCO_3$ PRECIPITATION RATES IN BEREA SANDSTONE CORES UNDER LOW AND HIGH PRESSURE CONDITIONS

## Goal and Experimental Conditions

To continue the efforts to answer the question of whether differences exist between high and low pressure conditions for collaborators at the University of Stuttgart to better calibrate their Darcy-scale model, two additional experiments were performed. These were performed in 2.5 cm diameter Berea sandstone cores drilled from the same block of sandstone described in this dissertation in Chapter 6. To begin, cores were loaded into the Hassler-type core holder and permeability was characterized with $NH_4Cl$ 10 g/L solution. In the low pressure experiment the overburden pressure was held at 300 psi and at high pressure at 1400 psi; each well above the pressure observed where bypass or backflow of the fluid around the core might be observed (Chapter 6). The cores were conditioned with urea growth medium and the cores were inoculated with *S. pasteurii*, nine hours of biofilm growth was promoted and then 6 hours of calcium urea medium was injected under semi-constant flow conditions (1 ml/min during flowing periods and batch periods of no-flow overnight). One core was treated with the effluent side of the core holder open to atmospheric conditions; the other core was subjected to the same flow conditions but with 75.8 bar (1100 psi) of back pressure controlled by a Teledyne Isco pump operated in constant pressure mode on the effluent side. Differential pressure and flow rate were monitored to assess changes in permeability. Effluent samples were collected and analyzed with the modified Jung assay for urea and IC for calcium [27]. At the termination of each experiment, the cores were cut into four equally spaced sections along the flow path and portions of the cut cores were ground and digested with 10% trace metal grade $HNO_3$ which was diluted to 5% and appropriately for analysis with ICP-MS to determine calcium concentration.

## Results

### Permeability

Permeability was observed to decrease in both low and high pressure experiment cores (Figure Appendix G.1). The core mineralized under high pressure was reduced from ~60 md to 5 md and the low pressure experiment core from ~60 to 0.8 md. To determine the difference between high and low pressure and the pressures impact on mineralization, comparing the permeability may not be the best metric as the core mineralized in the high pressure experiment did not reach as low of permeability (5 vs. 0.8 md) as the low pressure experiment. This was perhaps due to an artifact in the sampling where during sampling under high pressure large differential pressures can be initiated due to filling the sampling loop. This could contribute to possible breakage of newly formed mineral, although this speculation cannot be confirmed.

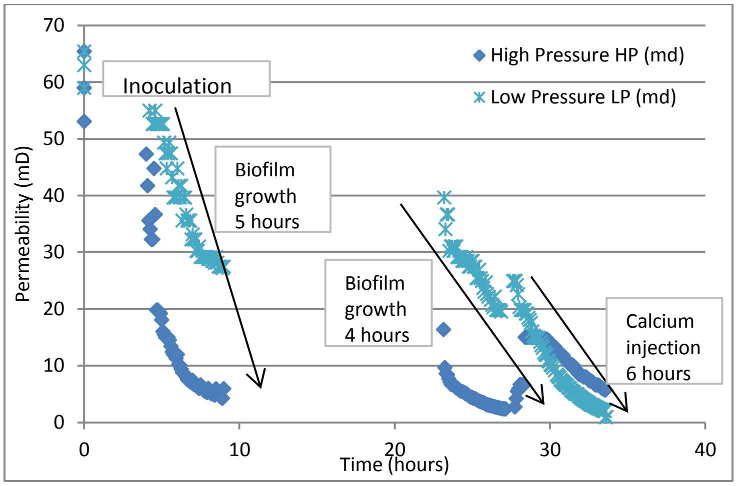

Figure Appendix G.1. Permeability over time of the constant flow biomineralization experiment performed under low(*) and high (♦) pressure.

Residual Effluent Analysis: Urea and Calcium

Not all of the urea was hydrolyzed during the biofilm growth stage (Figure Appendix G.2). Based on the difference between the known influent urea concentration and the measured effluent urea concentration it was determined that the overall urea hydrolyzed in the low pressure experiment was 8.2% (1.48 g hydrolyzed out of the 18 total grams injected) and under high pressure was 9.3% (1.67 g hydrolyzed out of the 18 total grams injected).

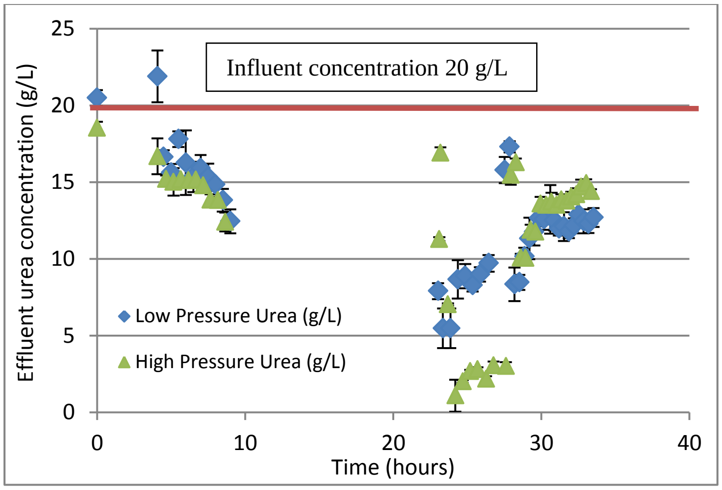

Figure Appendix G.2. Urea concentration in the residual effluent from both low (♦) and high pressure (▲) experiments.

Then to determine the urea hydrolysis rates during the first five hours of biofilm growth, the difference between the influent and the measured effluent concentration of urea was divided by the residence time in the core to achieve a rate in (mol/L/min). The ureolysis rates ranged from 7.3 x $10^{-3}$ to 2.5 x $10^{-2}$ mol/L/min for the low pressure experiment and from 1.1 x 10-2 to 2.9 x 10-2 mol/L/min for the high pressure experiment

(Figure Appendix G.3). Since only one high pressure and one low pressure experiment were performed, no statistically significant conclusion can be drawn from these data, although the trends of the ureolysis rates for both low and high pressure experiments are not drastically different from each other and both are increasing. This suggests ureolysis rates are increasing over time which is hypothesized due to biofilm growth and increasing cell concentrations.

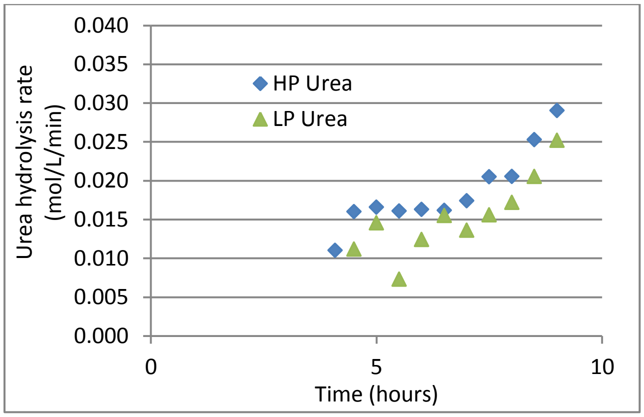

Figure Appendix G.3. Urea hydrolysis rates over time in both low (LP) and high pressure (HP) experiments. Since only one high pressure and one low pressure experiment were performed, no statistically significant conclusion can be drawn from these data, although high pressure ureolysis rates are observed to be greater than the low pressure rates. The trends of the ureolysis rates for both low and high pressure experiments are not drastically different from each other and both are increasing. This suggests ureolysis rates are increasing over time which is hypothesized due to biofilm growth and increasing cell concentrations.

During the 6 hour calcium injection, rates of ureolysis and calcium precipitation were calculated by the difference between the sampled influent and effluent concentration of urea or calcium, divided by the residence time in the core to obtain a rate in mol/L/min (Figure Appendix G.4). It was assumed that the difference between the influent and effluent concentrations of calcium was due to precipitation.

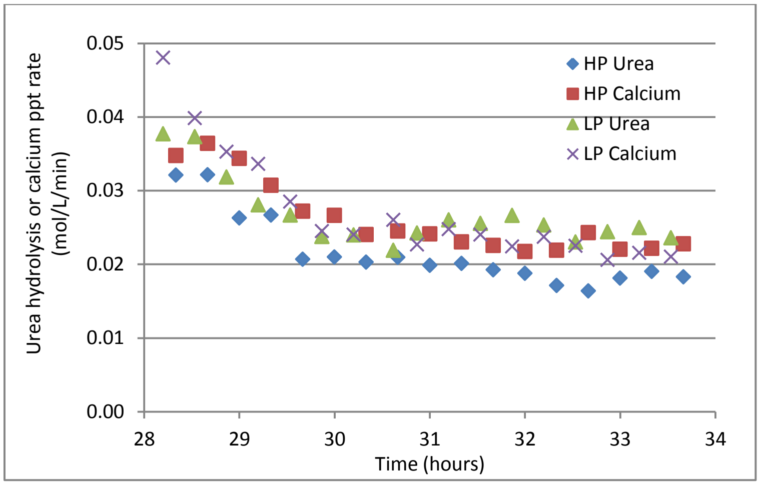

Figure Appendix G.4. Ureolysis and calcium precipitation rates over time during calcium urea medium injection. Slight differences were observed between the urea rates observed under low (LP) and high pressure (HP) conditions with the high pressure urea rates reduced to those observed under low pressure conditions. This was opposite the trend observed during the biofilm growth stage where high pressure ureolysis rates were greater than low pressure ureolysis rates. Calcium precipitation rates are observed to have no difference between the low and high pressure conditions. Ureolysis rates and calcium precipitation rates decreased during the calcium injection stage which was hypothesized to be due to entombment of microbes during calcium precipitation leading to reduced ureolysis rates due to diffusion limitations of urea and urease or inactivation of microorganisms.

## Calcium Distribution

Noticeable precipitate was observed on the influent but not the effluent side of the core (Figure Appendix G.5). This precipitate was not well cemented onto the core face so care was taken to include it in the analysis for calcium; however several flakes of mineral were observed in the beaker storing the high pressure experiment core.

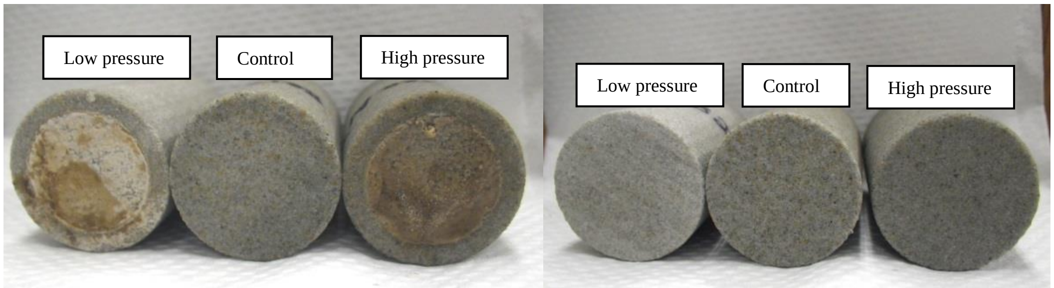

Figure Appendix G.5. Image of the influent and effluent side of the cores biomineralized under low and high pressure. (a) influent side, (b) effluent side.

The concentration of calcite per gram of sand in the four sections along the flow path of each high, low and control (not mineralized) cores was measured by ICP-MS

(Figure Appendix G.6). It was assumed that any measured calcium was in the polymorph of calcite. The calcite concentrations of the high pressure core were significantly lower than those measured in the low pressure core although both are significantly higher than the control core.

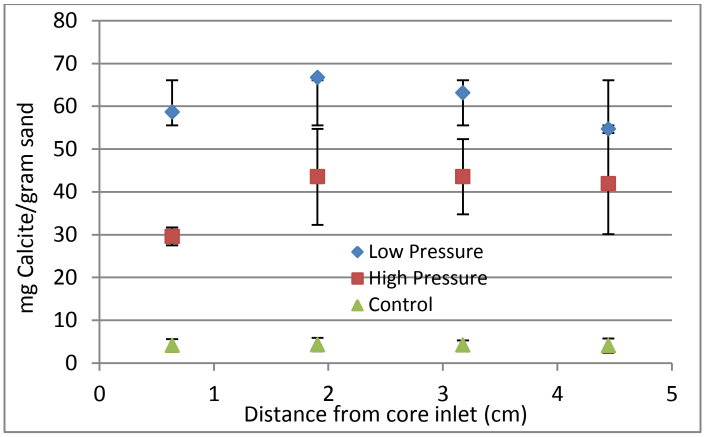

Figure Appendix G.6. Concentration of calcite achieved along the flow path in the biomineralized cores under low and high pressure compared to an unmineralized control.

Some of the difference in the near influent section could be attributed to the loss of mineral off the face of the core in the beaker holding the high pressure core. Also, large differential pressures introduced by sampling under high pressure could cause lightly cemented minerals to be loosened and not retained in the core compared to the low pressure core. Or, there may be a pressure-induced explanation for less mineral precipitated in the high pressure core, although the rates of calcium precipitation based on the effluent analysis were nearly identical for high and low pressure calcium precipitation rates. Additional experimentation including replicates could strengthen the conclusions made about the differences of the MICP processes under low and high pressure conditions.

# APPENDIX H

## X-RAY COMPUTED TOMOGRAPHY: POROSITY IN BEREA SANDSTONE CORES

## Experimental Conditions

The Sky Scan 1173 Micro-Computed Tomography (CT) scanner at the MSU Subzero Science and Engineering Research facility (Sky Scan, Kontich, Belgium) was used to scan Core #2 (Chapter 6) before and after MICP treatment and after exposure to $scCO_2$. CT works by sending X-rays through a sample to a detector to create a series of 2D images with resolution on the order of 10 µm. The sample's material density will control the X-rays penetration through the sample, resulting in an image where the sample densities are represented with different intensities of white to grey to black. Images were reconstructed into a 3D computed representation or viewed as cross-sections of the sample. The reconstructed images generated from the micro-CT were used to visualize pores by first down sampling the original images by half (from 2240 x2240 pixels to 1120x1120), setting a region of interest and binarizing the resulting images to separate pore space (air) from solid phase (sand/rock plus $CaCO_3$). These images were analyzed with the image analysis software CTAn (SkyScan, Kontich, Belgium) to calculate porosity in the samples before and after biomineralization and after exposure to $scCO_2$. Extensive down-sampling was required (1120x1120 pixels to 293x293) to speed image processing times, recreate 3D reconstructions and accommodate the computer's graphics capability.

## Results: X-Ray CT

Porosity was determined from binary images with the 2D analysis function in the CTAn Software (Sky Scan, Kontich, Belgium) for the core biomineralized in Experiment #2. The core was scanned and porosity assessed before biomineralization treatment, after biomineralization treatment and after exposure to $scCO_2$ (Table H.1).

Table Appendix H.1. Porosity determined from CT image analysis before and after biomineralization and after $scCO_2$ exposure.

| Core #2 | Porosity |
|---|---|
| Prebiomin | 6.1% |
| Post biomin | 10.2% |
| Post $scCO_2$ | 9.5% |

The results suggest that porosity increased after biomineralization which was not expected as biomineralization was shown to decrease the porosity of the sandstone core in Experiment #1 using mercury intrusion porosimetry (MIP) discussed in Chapter 6. The results also suggest that there was no observable increase in porosity after exposure to $scCO_2$ and in fact there was a decrease after exposure. The raw images from the CT scans at a point approximately 1/3 into the core from the influent side show no obvious differences to the core before or after mineralization or after $scCO_2$ exposure (Figure H.1). Finally, reconstructed 3D images (CTvol Software, Kontich, Belgium) of the core show no obvious differences such as wormhole development due to carbonate dissolution [200] to the core after $scCO_2$ treatment (Figure H.2).

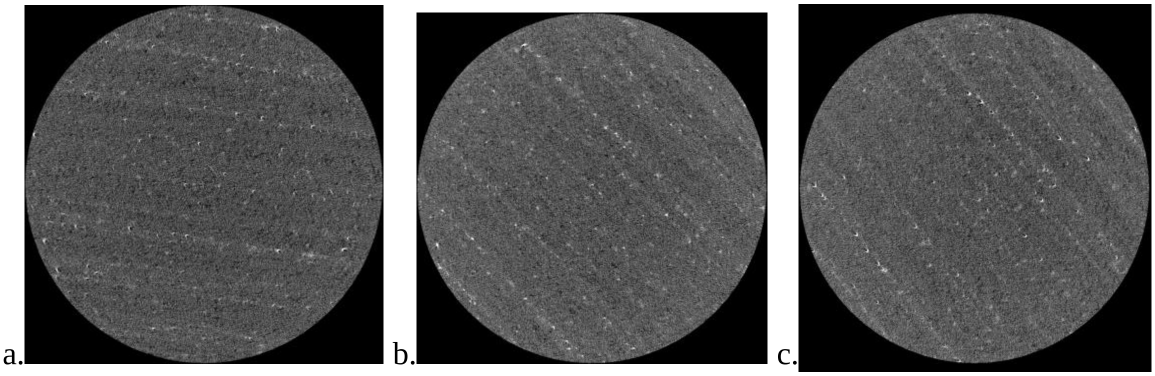

Figure H.1: Images of the CT scanned core from experiment #2 (a) before biomineralization (b) after biomineralization (c) after exposure to $scCO_2$.

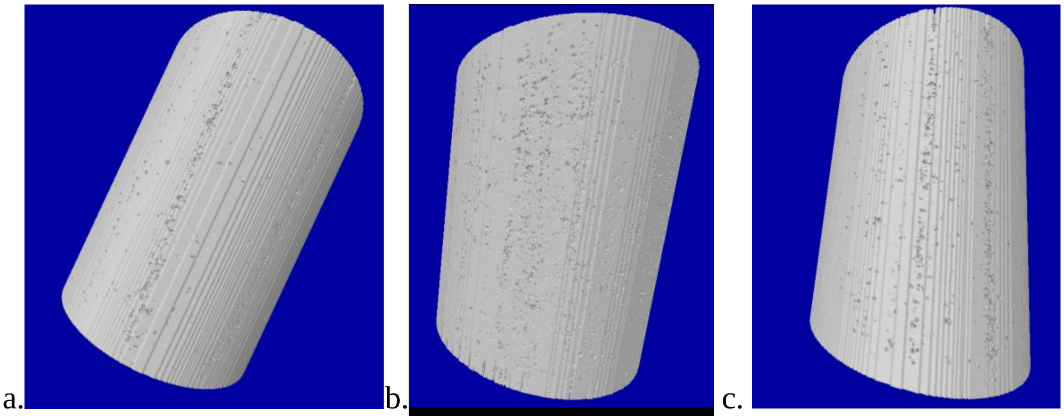

Figure H.2 Images of the 3D reconstructions of the CT scanned core from experiment #2 (a) before biomineralization (b) after biomineralization (c) after exposure to $scCO_2$.

While the results suggest there are no differences in the core before or after biomineralization or after exposures to $scCO_2$, the technique (X-Ray CT) may not be the most appropriate for assessing the porosity changes in the sandstone cores. A majority (50%) of the pore sizes in the core are in the 6-16 μm range as determined by MIP, yet the scans performed here have a resolution of 13.8 μm per pixel. Also, in order to accommodate the computer processing limitations the stack of images was down resolved by half to 27 μm per pixel. Underestimation of the porosity may occur because smaller pores cannot be resolved on these images resulting in underrepresentation of the pore space. Porosity in the control core was estimated to be 18.9% using MIP and only 6.1% with CT. Most likely the scan settings were not sensitive enough to detect the fine pore structure of the Berea sandstone. Since a majority of the pores are below the scan resolution, the CT scans might not be the most appropriate method for determining changes in porosity, especially in the fine pore structures.